A STUDY ON THE APPLICATIONS OF QUANTUM OPTICAL COHERENCE TO NANO-OPTICS

A Dissertation

by

JABIR WALI HAKAMI

Submitted to the Office of Graduate and Professional Studies of
Texas A&M University
in partial fulfillment of the requirements for the degree of

DOCTOR OF PHILOSOPHY

Chair of Committee,	M. Suhail Zubairy
Committee Members,	Marlan O. Scully
	Alexei Sokolov
	Goong Chen
Head of Department,	Peter McIntyre

May 2017

Major Subject: Physics

ABSTRACT

Optically controlled dipole-dipole interaction at submicrometers and subwavelength scales leads to many interesting phenomenon and remarkable potential applications in quantum optics, condensed matter physics, and today's micro-devices. In this dissertation, we study the applications of quantum optical coherence to nano-optics in the following systems and aspects. On the one hand, chiral metamaterials has been previously reported as excellent candidates to realize both attractive and repulsive Casimir forces, where the existence of a repulsive Casimir force depends upon the strength of the chirality. On the other hand, nanoscale integration of metal nanoparticles and semiconductors is particulary interesting because the strengths of both materials are combined in such a hybrid system. In the first part of this work, we proposed a technical scheme to coherently control of the Casimir interaction energy with two identical chirality mediums. We took explicit caution regarding the requirements of passivity and causal response of the materials, since these requirements are essential for the application of the Lifshitz formula. The rare-earth metals' atomic species, for instance, dysprosium, is proposed as an applicable medium for the forthcoming studies of possible experimental implementation of our technique. Secondly, we fully investigated the coherent control of the quantum optical properties of spontaneous emission spectra of a semiconductor quantum dot coupled to a metallic nanoparticle. The properties of the spontaneous emission spectra of such a system are studied in detail with and without involving the coherent field. The Rabi splitting effect in the spectrum emitted by the quantum dot under particular conditions is predicted for different sizes of the metal nanoparticles. We show that the spontaneous emission spectra of the transition coupled to surface plasmons may

be further modified by adjusting the external coherent control on the adjacent transitions. In the third part, we propose a robust protocol to study the entanglement generation in a hybrid structure consisting of two quantum dots in the proximity of a metallic nanoshell. The entanglement arises impulsively due to common coupling to the plasmonic nanostructure, without demanding postselective measurement or mediating the dissipative environment. The long-lived entangled states can be created deterministically by optimizing the shell thickness as well as the ratio of the distances between the quantum dots and the surface of the shell. The loss of the system is greatly reduced even when the quantum dots are ultraclose to the shell, which signifies a slow decay rate of the coherence information and longtime entanglement preservation.

To my parents ... ...

ACKNOWLEDGEMENTS

Primary acknowledgments are due to my advisor, Prof. M. Suhail Zubairy. Over my courses and research, he has always been approachable and very helpful, and I am very grateful for the invaluable advices that kept me on the right track, tolerance, and encouragement he gave me over the past years or so. His caring, patience, excellent guidance, physics intuition, and insight insured my research and constantly helped me from going in wrong directions to pursuit for answers. Beyond academic guidance, the more valuable things I learned from him are his proficient manner and enthusiastic attitude.

Next, I'd like to convey my thanks to Prof. Ali Kamli for encouraging and inspiring through my graduate studies. Also, I'd like to extend my gratitude to Prof. M. Al-Amri, Prof. Li-Gang Wang, and Dr. Xiaodong Zeng for offering their expertise through many stimulating discussions. I would also like to thank my dissertation committee Prof. Marlan Scully, Prof. Alexei Sokolov and Prof. Goong Chen for providing me valuable suggestions.

I am grateful to work with several wonderful former and current group members Dr. Qing-qing Sun, Dr. Shuai Yang, Dr. Zeyang Liao, Dr. Wenchao Ge, and Longfei Fan. I am also thankful to my friends Dr. Da-wei Wang, Dr. Shun Mao, Dr. Huawei Gao, Dr. Jing-han Chen and many other friends and colleagues for their help and stimulating discussions during the past years.

Finally, the big vote of thanks though must go to my family for their faith and support. Last, but not least, I am deeply grateful to my parents for their patience and support over the years.

CONTRIBUTORS AND FUNDING SOURCES

First of all, I would like to acknowledge my advisor Prof. M. Suhail Zubairy for his caring, patience, excellent guidance, physics intuition, and insight that insured my research from going in wrong directions to pursuit for answers. Beyond academic guidance, the more valuable things I learned from him are his proficient manner and enthusiastic attitude. Next,I would like to thank my dissertation committee Prof. Marlan Scully, Prof. Alexei Sokolov and Prof. Goong Chen for providing me valuable suggestions. This work was supervised by a dissertation committee consisting of Prof. M. Suhail Zubairy, Prof. Marlan Scully and Prof. Alexei Sokolov in physics department and Prof. Goong Chen from Mathematics department. All work for the dissertation was studied and completed independently by the student.

There are no outside funding offerings to acknowledge related to the research and compilation of this document.

TABLE OF CONTENTS

Page

LIST OF FIGURES

FIGURE Page

1. INTRODUCTION

One of the fascinating subjects that attracts numerous of researchers in different scientific disciplines and has remarkable potential applications in several diverse practical scenarios is the optically controlled dipole-dipole interaction at subwavelength scales. The relevance of this subject stems from its many possible exploitations. Fluctuation-induced electromagnetic forces between neutral bodies, for example, become more and more important as micromechanical and microfluidic devices enter submicrometre scales [1, 2]. Depending on the regime in which these forces operate, they are known by several different names including van der Waals, Casimir-Polder and, more generally, Casimir forces [3, 4, 5]. Therefore, the study of short-range dipole-dipole interaction can be helpful in understanding and measurement of Casimir forces and consequently allow them to be exploited in novel microelectromechanical systems (MEMS) and microfluidic devices.

The Casimir effect was first derived in 1948 by Casimir [6]. In 1948, Hendrik Casimir predicted that two uncharged, perfectly conducting plates in a vacuum would be attracted to each other because of quantum fluctuations in vacuum's electromagnetic field between the plates. Therefore, a change of the zero-point energy of the quantized electromagnetic field in the confined space due to the presence of the boundary surface results in the Casimir force on macroscopic bodies [7]. He considered a pair of neutral perfectly conducting parallel plates separated by a distance d placed in vacuum and found that there is an attractive force between the two plates. In contrast to the ideal case of perfectly reflecting mirrors considered by Casimir, Lifshitz [8] calculated the force acting on two thick (semi-infinite) dielectric slabs by taking into consideration the dispersion and absorption as well as the temperature

effects in the dielectrics. He obtained the force by calculating the Maxwell stress tensor in the region between the slabs by employing a dissipation-fluctuation relation, where he introduced into the Maxwell equations a phenomenological term "random electric field" that acts as a Langevin noise source. Since then, various practical situations with different geometries of the boundary surfaces have been investigated and corrections to the ideal case are found. In most cases the force is found to be attractive. In recent years, with the development of microelectromechanical (MEMS) and nanoelectromechanical (NEMS) systems and nanotechnology, the experimental measurement of the force has become possible [9, 10]. The attractive Casimir force may strongly affect processing in nanotechnology as well as functioning of micromachines and nanomachines devices. This is also could lead to the problem of sticking in MEMS and NEMS, which can be avoided if the Casimir force is repulsive. Clearly, these new developments posture the problem of realistic calculations of the Casimir force on objects in complex environments. Therefore, recently the repulsive Casimir force has attracted attention due to this practical significance [11, 12].

Over the last decades, impressive efforts have been made to investigate the repulsive Casimir force [13]. For example, in recent papers, Rosa et al. [14, 15] used a combination of a purely nonmagnetic Drude-modeled silver and magnetodielectric metamaterials and found a repulsive force in some range of values of the displacement d. Yang et al. [16] found that by adjusting the electromagnetic properties of materials, it is feasible to control the Casimir force between two parallel plates. They realized that the Casimir force can be repulsive (attractive) when the electromagnetic properties of the two plates are different (the same). The mechanism to obtain Casimir repulsion [17] is based on an asymmetric setup of nonmagnetic and magnetic materials. Zhao et al. [18, 19, 20] also studied the Casimir force by considering different types of materials. They concluded that the strong chirality is the

best candidate in producing nanolevitations resulting from the "repulsive Casimir force".

Another vital application of optically controlled dipole-dipole interaction can be appreciated with rapidly growing areas of physics and nanotechnology focuses on plasmonic effects on the nanometre scale, with possible applications ranging from sensing and biomedicine to imaging and information technology. In quantum optics, the strong-coupling regime can usually be achieved via cavity quantum electrodynamics [21, 22]. However, this approach needs a very high quality factor of a cavity or a small effective mode volume, which are difficult to realize by the conventional methods. Recently, Chang et al. [23, 24] proposed a new method to achieve strong, coherent coupling between individual emitters and electromagnetic excitations in conducting nanostructures at optical frequencies, via excitation of plasmons localized to nanoscale dimensions. This strong coupling is possible due to the small mode volume associated with the subwavelength surface-plasmonic confinement [25].

Modern studies of nano-optics concerned with dipole-dipole interaction involve a series of interesting topics, such as long-range plasmon-assisted energy transfer and coupling between fluorescent emitters, which has been a topic of major interest in research over the past decades [26, 27, 28, 29]. In 2003, David Bergman and Mark Stockman proposed such a device that is based on surface plasmons the so-called spaser (short for surface plasmon amplification by stimulated emission of radiation) [30, 31]. Moreover, there has been a large number of investigations on the modifications of spontaneous emission and resonance fluorescence of quantum emitters near various plasmonic structures [32, 33, 34, 35, 36, 37, 38, 39, 40, 41, 42, 43]. More ornate experiments have demonstrated that localized plasmon fields near MNPs profoundly modify the optical properties of single emitters (e.g., fluorescence molecules [44, 45], nitrogen vacancy centers in diamond nanocrystals [46], and photoluminescence decay

of semiconductor quantum dots coupled to nearby metallic nanostructures [47, 48]).

Surface plasmon polaritons, hybrid bound modes encompassing both electromagnetic fields and charge currents, are known to have both a strong subwavelength confinement and propagation lengths of tens or even hundreds of wavelengths [49]. The fascinating applications of plasmonic nanostructures at subwavelength scales are inspiring researchers in different disciplines.

Recently, the interaction between quantum emitters and surface plasmon polaritons has attracted great interest due to their remarkable applications such as generation of single surface plasmon polaritons [24] and that the interaction between two quantum emitters can be mediated by surface plasmon polaritons, resulting in energy transfer, superradiance [27], and entanglement phenomena. Therefore, quantum computation relying on controlled entanglement among the constituent bits of the quantum computer is also benefited from the strong interaction with plasmonic nanostructures. It has been demonstrated that semiconducting quantum dots are promising candidates for the basic device units for quantum information processing [50, 51]. Remarkably, quantum dots offer many advantages over atomic systems, including the small size and large optical dipole moments and transition energies, and they can be positioned deterministically and remain stationary without requiring atom traps [52, 53, 54]. Fundamentally, a strong light-matter interaction is a prerequisite to generate entanglement between quantum bits (qubits) for optical quantum information systems.

In this dissertation, we study the applications of quantum optical coherence to nano-optics at subwavelength scales in three different aspects related to the practical applications of Casimir force and quantum plasmonics. In the first part, the interaction energy between two chiral mediums is considered with the possibility that the Casimir force can be coherently controlled. We have reviewed the general deriva-

tions of Casimir force and generalized the results of the reflection matrices accounting the properties of anisotropic chiral media. We have proposed for the first time, to our knowledge, a practical scheme studying coherent control of the Casimir force at nanoscale with the possibility of switching between attractive and repulsive forces. In the second part, the properties of the spontaneous emission spectra of a system consisting of a quantum dot coupled to a metallic nanoparticle is manipulated via external coherent control. Furthermore, the interaction of the quantum dot in the proximity of plasmonic nanostructure is reconnoitered in different regiems. In the third part, we extended our study to the applications of the quantum entanglement in a hybrid structure consisting of two quantum dots (QDs) in the proximity of a metal nanoshell. Plasmonic modes in such a structure is explored with different materials with finding that nanoshell support surface plasmon resonances with extraordinary properties that are highly geometric dependent [55, 56, 57], and they respond more sensitively to the changes in the environment. This may lead to the design of devices at the nanoscale that may be useful for the quantum computing community.

2. COHERENT CONTROL OF CASIMIR FORCES IN CHIRAL METAMATERIALS *

2.1 Introduction

The Casimir effect is an enthralling quantum electrodynamic phenomenon in which the vacuum energy of the electromagnetic field is changed by the presence of two closely spaced mirrors coupled to the field, resulting in a measurable force between them. A change of the zero-point energy of the quantized electromagnetic field due to the presence of the boundary surfaces results in the Casimir force on macroscopic bodies. The Casimir effect, fluctuation-induced electromagnetic forces, was first derived in 1948 by Casimir [6] for highly idealized system consisting of a pair of neutral perfectly conducting parallel plates separated by a distance d placed in vacuum. He found that there is an attractive force between the two plates. Since then, various practical situations with different geometries of the boundary surfaces have been investigated and corrections to the ideal case are found. In recent years, with the development of microelectromechanical (MEMS) and nanoelectromechanical (NEMS) systems and nanotechnology, the experimental measurement of the force has become possible [9, 10]. In most cases the force is found to be attractive.

The Casimir forces in the nonretarded limit are the van der Waals forces, dominant the interaction between nanostructures and cause permanent stiction in small devices such as MEMS and NEMS systems. Thus, the attractive Casimir force could lead to the problem of sticking in MEMS and NEMS, which can be avoided if the Casimir force is repulsive. Activated by this urgent practical issue in nano-

*Reprinted with permission from "Coherent control of Casimir force in a chiral medium," by Jabir Hakami and M. Suhail Zubairy, 2012, J. Phys. B: At. Mol. Opt. Phys., volume 45, p. 205502, copyright [2012] by IOP Publishing Ltd.

electromechanical systems and the fast development of force detection techniques, experimental and theoretical investigations on these forces between neutral bodies have experienced an extraordinary revitalization in the past few years. Particularly, the repulsive Casimir force has attracted attention due to this practical significance. Consequently, a repulsive Casimir interaction would be advantageous to prevent stiction as well as for frictionless suspension and other applications.

Over the last decades, numerous efforts have been made to investigate the repulsive Casimir forces in variety of setting. For example, based on theoretical magnetic materials, in recent papers, Rosa et al. [14, 15] used a combination of a purely nonmagnetic Drude-modeled silver and magnetodielectric metamaterials and found a repulsive force in some range of values of the displacement d. Yang et al. [16] found that by adjusting the electromagnetic properties of materials, it is feasible to control the Casimir force between two parallel plates. They realized that the Casimir force can be modulated realizing repulsive (attractive) when the electromagnetic properties of the two plates are different (the same). Another mechanism to obtain Casimir repulsion [17] is based on an asymmetric setup of nonmagnetic and magnetic materials. Moreover, Zhao et al. [18, 19, 20] have been suggested that vacuum separated chiral metamaterials may exhibit repulsive interaction and subsequently led to stable repulsive-attractive transitions. They concluded that the strong chirality is the best candidate in producing nanolevitations resulting from the "repulsive Casimir force".

So far, there have been predominantly some mechanisms to realize a repulsive Casimir force: (i) two dielectric objects characterized by the dielectric permittivities $\epsilon_1(i\xi)$ and $\epsilon_2(i\xi)$ embedded in a fluid with $\epsilon_3(i\xi) \equiv \epsilon_{\text{fluid}}(i\xi)$ can become repulsive if their dielectric permittivities satisfy $\epsilon_1(i\xi) < \epsilon_{\text{fluid}}(i\xi) < \epsilon_2(i\xi)$ over a sufficiently wide range of imaginary frequencies ξ [58]. However, this kind of system has friction because of the existence of the liquid. (ii) Boyer's Casimir repulsion, based on

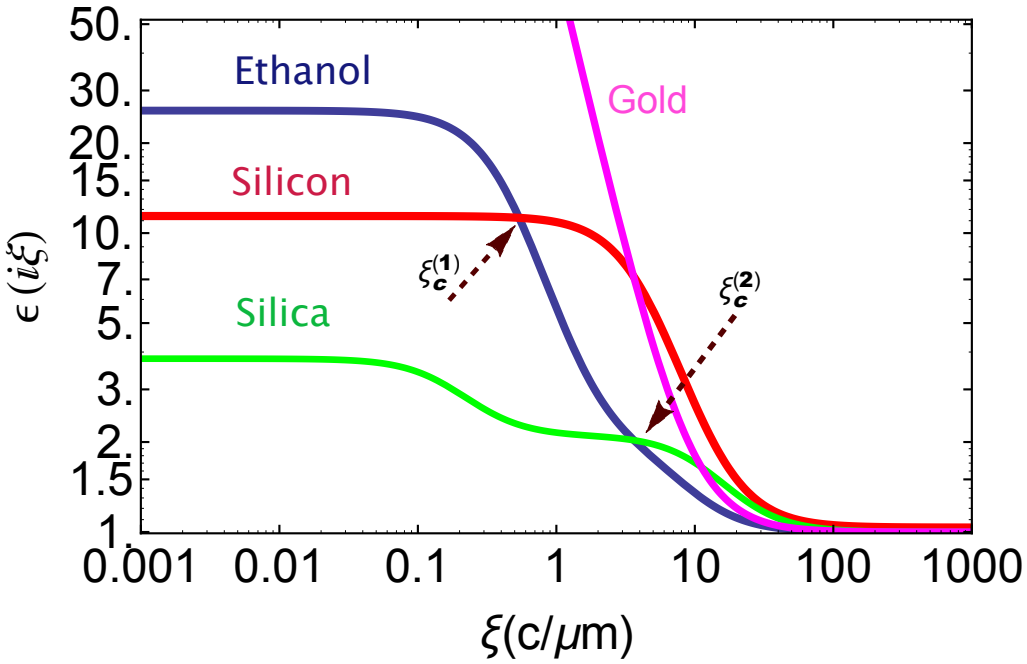

Figure 2.1: The dielectric permittivity $\epsilon(i\xi)$ of various materials (Si, SiO_2, ethanol, and gold) evaluated at imaginary frequency ξ in units of $c/\mu m$. Labeled are the two dielectric crossings $\xi_c^{(1)}$ and $\xi_c^{(2)}$ for obtaining stability that can be used as a guide to establish the existence of stable separations.

asymmetric setup of a nonmagnetic ($\epsilon > \mu$) plate together with a magnetic ($\mu > \epsilon$) plate [17]. Such nontrivial magnetic materials in the optical regime do not exist in nature, and, therefore, this proposal relies on the nontrivial possibility of developing new artificial negative index metamaterials (NIMs). (*iii*) two interacting plates sandwiching a perfect lens [13]. This system needs a perfect lens at all frequencies with simultaneously negative dielectric permittivity and magnetic permeability.

After considering a number of possibilities as shown in figure 2.1, we have identified several material combinations that satisfy condition (*i*) for large ξ (small separations). In figure (2.1), we plot the dielectric permittivity $\epsilon(i\xi)$ of various materials (Si, SiO_2, and ethanol) satisfying condition (*i*) over some large frequencies. The

possibility of obtaining equilibrium or stable separations arises if the force transition from repulsive at small separations which is conceptually dominated by large-ξ contributions to attractive force at large separations which is conceptually dominated by small-ξ contributions. Therfore, a criterion for obtaining stability is that $\epsilon_1(i\xi) < \epsilon_{\rm fluid}(i\xi) < \epsilon_2(i\xi)$ be violated at small ξ, and satisfied for $\xi > \xi_c$, with the transition occurring at some critical frequencies $\xi_c \sim 2\pi c/\lambda_c$, where λ_c is a length scale at which the repulsive-attractive transition occurs.

A question of interest is whether it is possible to control the Casimir force coherently by an external field, e.g., a static magnetic field. In this section, we address this problem and propose an interesting scheme which realizes the coherent control of the Casimir force via the driving field in the appropriate multilevel systems based on electromagnetically induced transparency (EIT) to induce chirality. A variation of the external field can result in coherently control the medium and subsequently the Casimir force would be modified, possibly switching between attractive and repulsive, or even zero at some point.

The chapter is organized as follows. In Sec. 2.2, we briefly discuss some of the basic ideas and methods related to the evaluation of the Casimir energies and forces in some simple models and subsequently introduce Casimir-Lifshitz theory. In Sec. 2.3, the reflection coefficients is elaborated by applying the transformation properties of the electric and the magnetic fields in a chiral medium. In Sec. 2.4, we present the strategy and accuracy of realizing chirality atomic mediums under realistic conditions and implement the rare-earth metals atomic species such as dysprosium as an applicable medium for possible experimental implementation. In Sec. 2.5, we present the results using realistic parameter values and show that, by an external magnetic field we may control Casimir force. Finally, in Sec. 2.6 the conclusions are drawn.

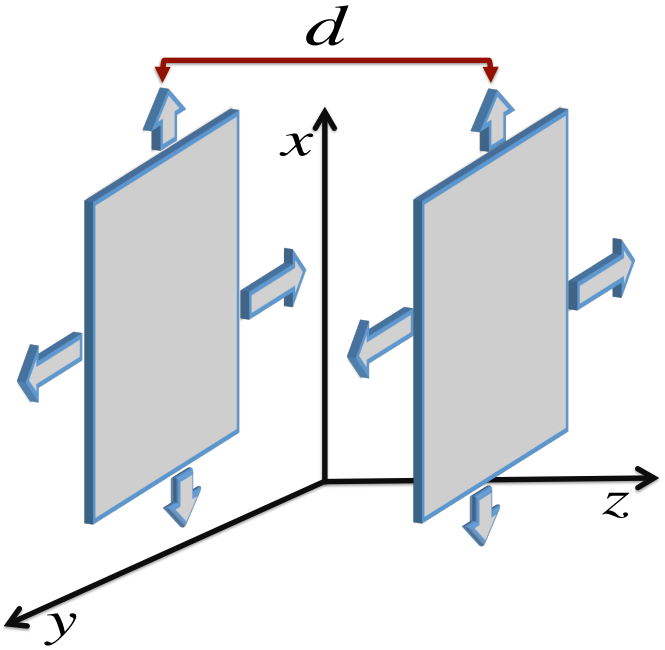

Figure 2.2: The cavity configuration for the calculation of the Casimir force.

2.2 Techniques for evaluation of Casimir force

2.2.1 The Casimir effect in its original formulation

Originally, the Casimir effect was predicted as a feature of irreducible fluctuations of electromagnetic fields between two natural ideally conducting plates. Casimir calculated this force in a geometrical configuration considering the ideal case of perfectly reflecting mirrors where two plane mirrors are positioned a distance d apart and parallel to each other, where the area A of the mirrors being much larger than the square distance $A \gg d^2$. The configuration system is schematically presented in figure (2.2). Inside the cavity, only particular field frequencies are allowed defined by

$$\omega_{\ell mn} = k_{\ell mn} c = \pi c \left[\frac{\ell^2}{L^2} + \frac{m^2}{L^2} + \frac{n^2}{d^2} \right]^{1/2} \tag{2.1}$$

The zero-point energy of the field inside the cavity is therefore

$$\begin{aligned}\Xi(d) &= \sum_{\ell,m,n}{}' (2)\frac{1}{2}\hbar\omega_{\ell,m,n} \\ &= \sum_{\ell,m,n}{}' \pi\hbar c\left[\frac{\ell^2}{L^2}+\frac{m^2}{L^2}+\frac{n^2}{d^2}\right]^{1/2}\end{aligned} \tag{2.2}$$

The factor 2 arises from two independent polarizations of modes with $\ell, m, n \neq 0$, and the prime on the summation symbol indicates that a factor $1/2$ should be inserted if one of these integers is zero.

In the physical situation of interest $L \gg d$ that we may replace the sum over ℓ and m in equation (2.2) by integrals

$$\Xi(d) = \sum_{\ell,m,n}{}' (2)\frac{1}{2}\hbar\omega_{\ell,m,n} \to \frac{L^2}{\pi^2}\hbar c \sum_{n}{}' \int_0^\infty dk_x \int_0^\infty dk_y \left(k_x^2+k_y^2+\frac{n^2\pi^2}{d^2}\right)^{1/2}. \tag{2.3}$$

This is infinite as the zero-point energy of the vacuum is infinite in any finite volume. Taking d to be arbitrarily large, the sum over n could be replaced by an integral. As proposed by Casimir, the energy required to bring the plates from a large separation to the separation d is

$$\begin{aligned}E(d) &= \Xi(d) - \Xi(\infty) \\ &= \frac{L^2\hbar c}{\pi^2}\int_0^\infty dk_x \int_0^\infty dk_y \left[\sum_{n=0}{}' \left(k_x^2+k_y^2+\frac{n^2\pi^2}{d^2}\right)^{1/2} - \frac{d}{\pi}\int_0^\infty dk_z \left(k_x^2+k_y^2+k_z^2\right)^{1/2}\right] \\ &= \frac{L^2\hbar c}{\pi^2}\frac{\pi}{2}\int_0^\infty du\, u \left[\sum_{n=0}{}' \left(u^2+\frac{n^2\pi^2}{d^2}\right)^{1/2} - \frac{d}{\pi}\int_0^\infty dk_z \left(u^2+k_z^2\right)^{1/2}\right].\end{aligned} \tag{2.4}$$

where the polar coordinates is used in the third line ($dk_x dk_y = u du d\theta$). Now, introducing a cutoff function $f(k) = f\left(\left[u^2+k_z^2\right]^{1/2}\right)$ which is unity for $k \ll k_m$ and tends

to zero rapidly for $k \gg k_m$. Physically, this cutoff function can be justified because the assumption of perfectly conducting plates breaks down at small wavelengths. With a change of variables $x = u^2 d^2/\pi^2$ and $\kappa = k_z d/\pi$, we thus replace equation (2.4) by

$$\begin{aligned} E(d) =& \frac{L^2 \hbar c}{4\pi} \frac{\pi^3}{d^3} \left[\int_0^\infty dx \sum_{n=0}^{'} \left(x + n^2\right)^{1/2} f\left(\frac{\pi}{d}\left[x + n^2\right]^{1/2}\right) \right. \\ & \left. - \int_0^\infty d\kappa \int_0^\infty dx \left(x + \kappa^2\right)^{1/2} f\left(\frac{\pi}{d}\left[x + \kappa^2\right]^{1/2}\right) \right] \\ =& \frac{\hbar c \pi^2}{4d^3} L^2 \left[\sum_{n=0}^{'} F(n) - \int_0^\infty d\kappa F(\kappa) \right]. \end{aligned} \tag{2.5}$$

Applying the Euler-Maclaurin formula and the fact that $F(\infty) \to 0$, then

$$\begin{aligned} E(d) =& \frac{\hbar c \pi^2}{4d^3} L^2 \left[-\sum_{m=1}^{\infty} \frac{B_{2m}}{(2m)!} F^{2m-1}(0) \right] \\ =& -\left(\frac{\hbar c \pi^2}{720 d^3}\right) L^2, \end{aligned} \tag{2.6}$$

where

$$F(\kappa) \equiv \int_0^\infty dx \left(x + \kappa^2\right)^{1/2} f\left(\frac{\pi}{d}\left[x + \kappa^2\right]^{1/2}\right). \tag{2.7}$$

The attractive force per unit area between the plates is then $F(d) = -\pi^2 \hbar c/240 d^4$.

2.2.2 Surface mode summation technique

The surface mode summation technique is based on the calculation of the electromagnetic surface modes $\omega(k_\parallel)$ due to the presence of the dielectric stacks and then evaluate the zero-point energy associated with these surface modes, $\sum_i \int dk_\parallel \frac{1}{2}\hbar\omega_i(k_\parallel)$ [7, 59]. This approach originally used by van Kampen et al. [60] to obtain Casimir forces for the case of small separations, where retardation can be ignored. Later, the method was extended to contain retardation effects [61].

We consider the case of a medium with dielectric permittivity $\epsilon_3(\omega)$ occupy the region $0 \leqslant z \leqslant d$ sandwiched between two semi-infinite media with dielectric permittivities $\epsilon_1(\omega)$ and $\epsilon_2(\omega)$ occupy $z < 0$ and $z > d$, respectively. The preceding boundary conditions at $z = 0$ and $z = d$, yields the solutions on the allowed frequencies ω.

$$\frac{\epsilon_3(\omega)K_1(\omega) + \epsilon_1(\omega)K_3(\omega)}{\epsilon_3(\omega)K_1(\omega) - \epsilon_1(\omega)K_3(\omega)} \frac{\epsilon_3(\omega)K_2(\omega) + \epsilon_2(\omega)K_3(\omega)}{\epsilon_3(\omega)K_2(\omega) - \epsilon_2(\omega)K_3(\omega)} e^{2K_3(\omega)d} - 1 \equiv F_a(\omega), \quad (2.8a)$$

$$\frac{K_1(\omega) + K_3(\omega)}{K_1(\omega) - K_3(\omega)} \frac{K_2(\omega) + K_3(\omega)}{K_2(\omega) - K_3(\omega)} e^{2K_3(\omega)d} - 1 \equiv F_b(\omega). \quad (2.8b)$$

where $K_j = \sqrt{k_\parallel^2 - \epsilon_j(\omega)\omega^2/c^2}$. The sums over modes include the continuum of values of k_x and k_y: $\sum_n \to \frac{L^2}{(2\pi)^2} \int d^2\boldsymbol{K}_\parallel \sum_N$.

The zero-point energy associated with these surface modes:

$$\begin{aligned} E(d) &= \sum_n \frac{1}{2}\hbar\omega_{na} + \sum_n \frac{1}{2}\hbar\omega_{nb} \\ &= \frac{\hbar L^2}{2(2\pi)^2} \int_0^\infty d^2\boldsymbol{K}_\parallel \left[\sum_N \omega_{Na}(k_\parallel) + \sum_N \omega_{Nb}(k_\parallel) \right], \end{aligned} \quad (2.9)$$

where $\sum_N$ denotes the sum over all solutions of equations (2.8) for $\omega(k_\parallel)$. The summations can be performed by recalling the argument theorem from the theory of functions of a complex variable: for a function $f(z)$ that is analytic everywhere except for poles on and inside a simple closed curve C,

$$\frac{1}{2\pi i} \oint_C \frac{f'(z)}{f(z)} dz = N - P, \quad (2.10)$$

where N is the number of zeroes and P is the number of poles of a function $f(z)$ inside C. The argument theorem of equation (2.10) can be rewritten in a generalization

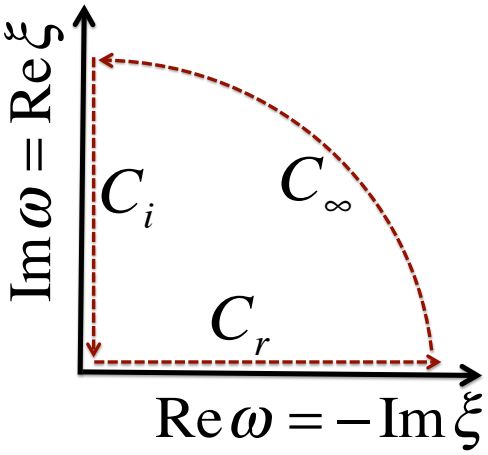

Figure 2.3: Contour representing the frequencies of interest for the evaluation of the Casimir force.

form

$$\frac{1}{2\pi i}\oint_C z\frac{f'(z)}{f(z)}dz = \left[\sum_i z_i\right]_{f(z_i)=0} - \left[\sum_i z_i\right]_{f(z_i)=\infty} \tag{2.11}$$

Here, as shown in figure (2.3), C is a closed curve defined by the imaginary axis of the complex ω plane and a semicircle in the right half of this plane, with a very large radius of the semicircle. Although the surface mode summation method applies only to purely dispersive (lossless) systems, the final result turns out to be applicable to absorbing systems as well when expressed as an integral over the imaginary frequency. This is must be true due to the fact that the dielectric function is always real on the imaginary axis regardless of whether the system is absorbing or not [62]. Equation (2.9) leads to

$$E(d) = \frac{\hbar L^2}{8\pi^2}\frac{1}{2\pi i}\int_0^\infty d^2\boldsymbol{K}_\parallel \left[\oint_C \omega\frac{F_a'(\omega)}{F_a(\omega)}d\omega + \oint_C \omega\frac{F_b'(\omega)}{F_b(\omega)}d\omega\right]. \tag{2.12}$$

Recalling the definition of the curve C, the integral along the imaginary axis is

$$\int_{\infty}^{-\infty}(i\xi)\frac{1}{F_\alpha(i\xi)}\frac{\partial F_\alpha(i\xi)}{\partial(i\xi)}(id\xi)$$

$$= -i\int_{-\infty}^{\infty}d\xi\xi\frac{F'_\alpha(i\xi)}{F_\alpha(i\xi)} = -i\int_{-\infty}^{\infty}d\xi\xi\frac{d}{d\xi}\log F_\alpha(i\xi) = i\int_{-\infty}^{\infty}d\xi\log F_\alpha(i\xi). \qquad (2.13)$$

Equation (2.12) is then

$$E(d) = \frac{\hbar L^2}{4\pi}\int_0^{\infty}\frac{d^2\boldsymbol{K}_\parallel}{(2\pi)^2}\left[\int_{-\infty}^{\infty}d\xi\log F_a(i\xi) + \int_{-\infty}^{\infty}d\xi\log F_b(i\xi)\right]. \qquad (2.14)$$

The force per unit area is therefore

$$F(d) \equiv -\frac{\partial}{\partial d}E(d) = -\frac{\hbar}{\pi}\int_0^{\infty}\frac{d^2\boldsymbol{K}_\parallel}{(2\pi)^2}\int_0^{\infty}d\xi K_3\left[\frac{1}{F_a(k_\parallel,i\xi)} + \frac{1}{F_b(k_\parallel,i\xi)}\right], \qquad (2.15)$$

where $F_a(k_\parallel,i\xi)$ and $F_b(k_\parallel,i\xi)$ are defined in equations (2.8) with $\epsilon_j = \epsilon_j(i\xi)$ and $K_j = \sqrt{k_\parallel + \epsilon_j(i\xi)\xi^2/c^2}$. The Casimir effect in multilayered systems in derived by Zhou and Spruch [59] using this method assuming a purely dispersive system. Klimchiskaya et al. [63] recently considered the problem of absorbing system.

Lifshitz [8] generalized the derivation of Casimir force acting on two thick (semi-infinite) dielectric slabs by taking into consideration the dispersion and absorption as well as the temperature effects in the dielectrics. The details of Lifshitz's calculation are fairly complicated. The Lifshitz approach is based on the calculation of the electromagnetic field due to a random electric field corresponding to some randomly fluctuating currents in the dielectric slabs that he introduced into the Maxwell equations as a phenomenological term that acts as a Langevin noise source and on the subsequent calculation of the Maxwell stress tensor in the region between the slabs by employing a dissipation-fluctuation relation. More recently, the Lifshitz

formula is extended to general bi-anisotropic media. Another alluring method for the calculation of the Casimir force is the so-called scattering approach based on the computation of the free energy of the electromagnetic field in regions bounded by material boundaries using the quantum optical networks theory [64].

2.2.3 The stress tensor method

In this subjection, we base the calculation of the Casimir force by employing the macroscopic field operators as arise from a recently developed scheme for quantizing the electromagnetic field for a give permittivity in inhomogeneous dissipative 3D systems using a source-quantity representation of the field in terms of the classical Green tensor and an infinte set of bosonic fields.

In Appendix A, we have provided the detail derivations of the Casimir force in absorbing multilayer dielectric plates at finite temperatures as used by Tomaš [62] and recently by Raabe et al. [65]. The contributions of all (propagating and evanescent) modes are naturally taken into account on an equal foundation through the Green tensor accounting to a general properties if absorbing multilayer.

The final formula for the Casimir force or the interaction energy per unit area A between two parallel plates separated by a vacuum gap of width d is expressed in terms of the reflection coefficients r_j^{ab} $(j = 1, 2)$, giving the ratio of the amplitudes of a reflected electromagnetic field with b polarization and an incoming electromagnetic field with a polarization. Here a and b stands for either electric (TM or p) or magnetic (TE or s) waves. The frequency integration is evaluated at the imaginary frequencies $\omega = i\xi$. The interaction energy per unit area is given by

$$\frac{E(d)}{A} = \frac{\hbar}{2\pi}\int_0^\infty d\xi \int \frac{d^2\boldsymbol{K}_\parallel}{(2\pi)^2} \ln\det\left[1 - \boldsymbol{R_1}\cdot\boldsymbol{R_2}e^{-2Kd}\right], \tag{2.16}$$

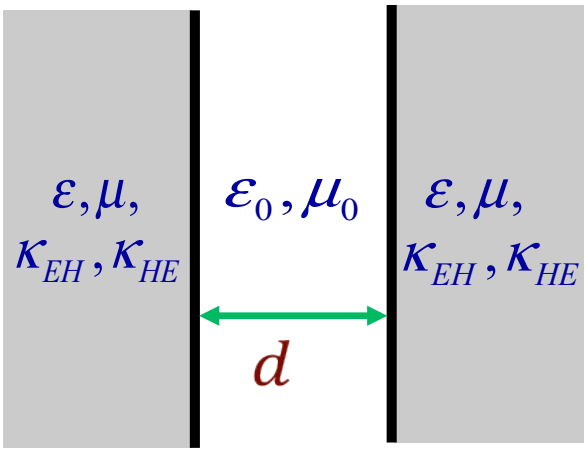

Figure 2.4: The system considered schematically. ϵ, μ, κ_{EH}, and κ_{HE} are the permittivity, the permeability, and the chirality coefficients, respectively. ϵ_0 and μ_0 are the permittivity and the permeability in the free space.

and the expression for the force per unit area is given by

$$\frac{F(d)}{A} \equiv -\frac{\partial}{\partial d}E(d) = 2\hbar \int_0^\infty \frac{d\xi}{2\pi} \int \frac{d^2\boldsymbol{K}_\parallel}{(2\pi)^2} K \mathrm{Tr} \frac{\boldsymbol{R_1} \cdot \boldsymbol{R_2} e^{-2Kd}}{1 - \boldsymbol{R_1} \cdot \boldsymbol{R_2} e^{-2Kd}}, \tag{2.17}$$

where the reflection matrices for general anisotropic chiral media are defined as

$$\boldsymbol{R}_j = \begin{bmatrix} r_j^{s,s}(i\xi, k_\parallel) & r_j^{s,p}(i\xi, k_\parallel) \\ r_j^{p,s}(i\xi, k_\parallel) & r_j^{p,p}(i\xi, k_\parallel) \end{bmatrix}, \tag{2.18}$$

where $\boldsymbol{K}_\parallel$ is the transverse wave vector and $K = \sqrt{\boldsymbol{K}_\parallel^2 + \frac{\xi^2}{c^2}}$.

2.3 Electromagnetic waves in a homogeneous chiral medium

2.3.1 Constitutive relations for an optically active medium

An achiral medium is expressed in terms of the constitutive rrelations $\boldsymbol{D} = \epsilon_0 \boldsymbol{E}$ and $\boldsymbol{B} = \mu_0 \boldsymbol{H}$. On the other hand, in a chiral medium, there is a magnetoelectric

cross coupling that relates the electric polarization $\boldsymbol{P}$ to the magnetic field $\boldsymbol{H}$ and the magnetization $\boldsymbol{M}$ to the electric field $\boldsymbol{E}$ so that [66, 67, 68, 69]:

$$\begin{pmatrix} \boldsymbol{P} \\ \boldsymbol{M} \end{pmatrix} = \begin{pmatrix} \epsilon_0\chi_e & \frac{\kappa_{EH}}{c} \\ \frac{\kappa_{HE}}{c\mu_0} & \chi_m \end{pmatrix} \begin{pmatrix} \boldsymbol{E} \\ \boldsymbol{H} \end{pmatrix}. \tag{2.19}$$

Here ϵ_0 and μ_0 are the permittivity and the permeability of the free space, respectively, while $\chi_e = \epsilon - 1$ and $\chi_m = \mu - 1$ are the electric and magnetic susceptibilities. κ_{EH} and κ_{HE} are the complex chirality coefficients. According to the relations $\boldsymbol{D} = \epsilon_0\boldsymbol{E} + \boldsymbol{P}$ and $\boldsymbol{B} = \mu_0(\boldsymbol{H} + \boldsymbol{M})$, the constitutive relations (2.19) can be rewritten as

$$\begin{pmatrix} \boldsymbol{D} \\ \boldsymbol{B} \end{pmatrix} = \begin{pmatrix} \epsilon_0\epsilon & \frac{\kappa_{EH}}{c} \\ \frac{\kappa_{HE}}{c} & \mu_0\mu \end{pmatrix} \begin{pmatrix} \boldsymbol{E} \\ \boldsymbol{H} \end{pmatrix}. \tag{2.20}$$

In harmonic time dependence, $exp(-i\omega t)$, and using Maxwell's equations, the constitutive relations (2.20) can be written in a matrix form

$$\nabla^2 \begin{pmatrix} \boldsymbol{E} \\ \boldsymbol{H} \end{pmatrix} + \boldsymbol{K}^2 \begin{pmatrix} \boldsymbol{E} \\ \boldsymbol{H} \end{pmatrix} = 0, \tag{2.21a}$$

$$\nabla \times \begin{pmatrix} \boldsymbol{E} \\ \boldsymbol{H} \end{pmatrix} = \boldsymbol{K} \begin{pmatrix} \boldsymbol{E} \\ \boldsymbol{H} \end{pmatrix}, \tag{2.21b}$$

$$\nabla \cdot \begin{pmatrix} \boldsymbol{E} \\ \boldsymbol{H} \end{pmatrix} = 0, \tag{2.21c}$$

where

$$\boldsymbol{K} = \begin{pmatrix} \frac{i\omega}{c}\kappa_{HE} & i\omega\mu_0\mu \\ -i\omega\epsilon_0\epsilon & -\frac{i\omega}{c}\kappa_{EH} \end{pmatrix} \tag{2.22}$$

After some straightforward algebra, the relations (2.20) together with Maxwell's equations $\boldsymbol{\nabla} \times \boldsymbol{E} = i\omega \boldsymbol{B}$ and $\boldsymbol{\nabla} \times \boldsymbol{H} = -i\omega \boldsymbol{D}$ leads to

$$\begin{aligned} &\boldsymbol{\nabla} \times \boldsymbol{\nabla} \times \boldsymbol{E} - (i\omega/c)(\kappa_{HE} - \kappa_{EH}) \boldsymbol{\nabla} \times \boldsymbol{E} \\ &- (\omega^2/c^2)(\epsilon\mu - \kappa_{EH}\kappa_{HE}) \boldsymbol{E} = 0, \end{aligned} \tag{2.23}$$

Note that, in the absence of the cross coupling coefficients, i.e., the chirality coefficients κ_{EH} and κ_{HE}, Eq. (2.23) reduces to the vector Helmholtz equation, $\boldsymbol{\nabla}^2 \boldsymbol{E} + \nu^2 \boldsymbol{E} = 0$, for non-chiral media. In a similar manner we obtain $\boldsymbol{\nabla}^2 \boldsymbol{H} + \nu^2 \boldsymbol{H} = 0$, where $\nu = (\omega/c)\sqrt{\epsilon\mu}$ and the identity $\boldsymbol{\nabla} \times \boldsymbol{\nabla} \times \boldsymbol{E} = \boldsymbol{\nabla}(\boldsymbol{\nabla} \cdot \boldsymbol{E}) - \boldsymbol{\nabla}^2 \boldsymbol{E}$ has been used.

Wave components in Eq. (2.23) possess different wave numbers depending on their helicity. They are expressed in terms of ν^- for the left-circular polarized wave (LCP) and ν^+ for the right-circular polarized wave (RCP)

$$\nu^{\mp} = \frac{\omega}{c} \sqrt{\epsilon^{\mp}\mu^{\mp} - \frac{(\kappa_{EH}^{\mp} + \kappa_{HE}^{\mp})^2}{4}} \pm \frac{i}{2}(\kappa_{EH}^{\mp} - \kappa_{HE}^{\mp}), \tag{2.24}$$

where $\epsilon^{\mp}$ and $\mu^{\mp}$ are the permittivities and the permeabilities, respectively, of the chiral medium. By defining the index of refraction of RCP (LCP) waves as $n^+(n^-)$, and using the relation $\nu^{\pm} = (\omega/c)n^{\pm}$, the general expression [70, 71] for the refractive index for the right (+ sign) and left (− sign) circular polarizations can be expressed as

$$n^{\pm} = \sqrt{\epsilon^{\pm}\mu^{\pm} - \frac{(\kappa_{EH}^{\pm} + \kappa_{HE}^{\pm})^2}{4}} \mp \frac{i}{2}(\kappa_{EH}^{\pm} - \kappa_{HE}^{\pm}). \tag{2.25}$$

In the next section, the coefficients $\epsilon^{\pm}$, $\mu^{\pm}$, $\kappa_{EH}^{\pm}$, and $\kappa_{HE}^{\pm}$ will be derived explicitly. The two reflective indices n^+ and n^- can then be calculated numerically based on Eq. (2.25).

2.3.2 The calculation of reflection elements

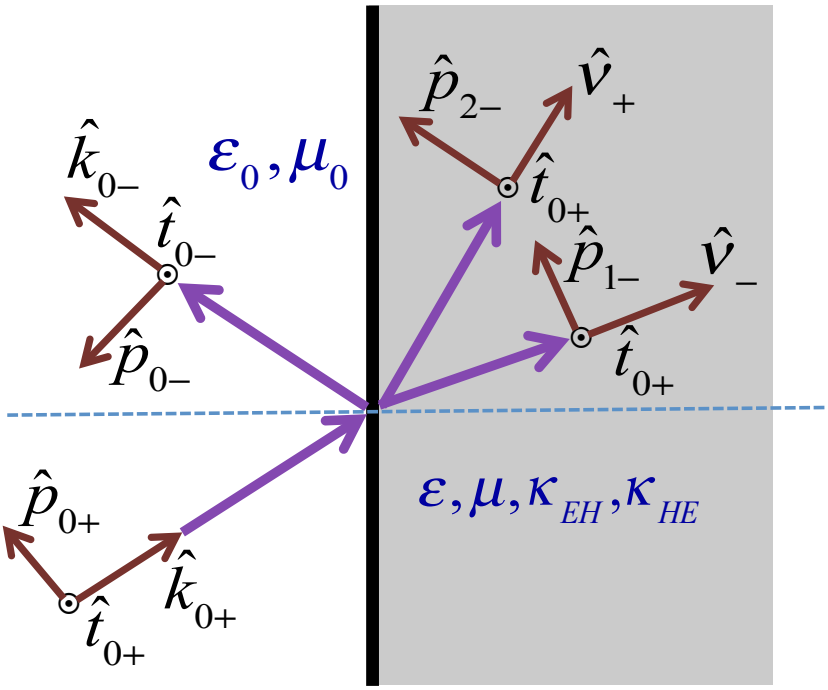

Figure 2.5: Circularly polarized plane wave transmission and reflection on a chiral half-space.

The structured geometry of the problem being considered is schematically presented in figure 2.4. The lower half space $z \leqslant 0$ as well as the zone $z \geqslant d$ are occupied by an isotropic chiral medium ($\boldsymbol{D} = \epsilon_0 \epsilon \boldsymbol{E} + \frac{\kappa_{EH}}{c} \boldsymbol{H}$, $\boldsymbol{B} = \mu_0 \mu \boldsymbol{H} + \frac{\kappa_{HE}}{c} \boldsymbol{E}$), while the infinite slab $0 \leqslant z \leqslant d$ is occupied by free space ($\boldsymbol{D} = \epsilon_0 \boldsymbol{E}$, $\boldsymbol{B} = \mu_0 \boldsymbol{H}$). Using an $\exp(-i\omega t)$ time-dependence, the following quantities are defined: $k_0 = \omega\sqrt{\epsilon_0 \mu_0}$ and $\eta_0 = \sqrt{\mu_0/\epsilon_0}$ for free space; $k = \omega\sqrt{\epsilon\mu}$, $\eta\sqrt{\mu/\epsilon}$, $\beta_1 \equiv \nu_-$ and $\beta_2 \equiv \nu_+$ for the chiral medium. It is worth mentioning that all quantities thus defined have definite magnitudes; furthermore, $\mathrm{Re}[\eta] > 0$, $\mathrm{Re}[\beta_1 > 0]$, $\mathrm{Re}[\beta_2 > 0]$, $\mathrm{Im}[\beta_1 > 0]$ and $\mathrm{Im}[\beta_2 > 0]$.

Let the cartesian unit vectors be denoted by $\boldsymbol{e}_x$, $\boldsymbol{e}_y$ and $\boldsymbol{e}_z$. After defining the quantities indicated in figure 2.5.

$$\boldsymbol{k}_{0\pm}\{k_x, k_y\} = k_x\boldsymbol{e}_x + k_y\boldsymbol{e}_y + k_z\boldsymbol{e}_z \quad , \tag{2.26a}$$

$$\boldsymbol{t}_{0\pm}\{k_x, k_y\} = -(\frac{1}{k_\parallel})(k_y\boldsymbol{e}_x - k_x\boldsymbol{e}_y) \quad , \tag{2.26b}$$

$$\boldsymbol{p}_{0\pm}\{k_x, k_y\} = -(\pm\frac{k_{0z}}{k_\parallel k_0})(k_x\boldsymbol{e}_x + k_y\boldsymbol{e}_y) + (\frac{k_\parallel}{k_0})\boldsymbol{e}_z \quad , \tag{2.26c}$$

$$k_\parallel\{k_x, k_y\} = \sqrt{k_x^2 + k_y^2} \quad , \tag{2.26d}$$

$$k_{0z}\{k_x, k_y\} = \sqrt{k_0^2 - k_\parallel^2} \quad , \tag{2.26e}$$

that are functions of the horizontal wavenumbers k_x and k_y, the electromagnetic fields in the lower half space is given by

$$\begin{aligned}\boldsymbol{E} = \big[&\{A_\perp\boldsymbol{t}_{0+} + A_\parallel\boldsymbol{p}_{0+}\}\exp(ik_{0z}z) \\ &+ \{B_\perp\boldsymbol{t}_{0-} + B_\parallel\boldsymbol{p}_{0-}\}\exp(-ik_{0z}z)\big]\exp[i(k_x x + k_y y)], \qquad z \leqslant 0\end{aligned} \tag{2.27a}$$

and

$$\boldsymbol{H} = \frac{\nabla \times \boldsymbol{E}}{i\omega\mu_0}, \tag{2.27b}$$

$$\begin{aligned}\eta_0\boldsymbol{H} = \big[&\{-A_\parallel\boldsymbol{t}_{0+} + A_\perp\boldsymbol{p}_{0+}\}\exp(ik_{0z}z) \\ &+ \{-B_\parallel\boldsymbol{t}_{0-} + B_\perp\boldsymbol{p}_{0-}\}\exp(-ik_{0z}z)\big]\exp[i(k_x x + k_y y)], \qquad z \leqslant 0\end{aligned} \tag{2.27c}$$

where $\eta = \sqrt{\mu_0\ \epsilon_0}$. The coefficients $A_\perp$ and $A_\parallel$ represent plane-wave eigenmodes incident on the interface, while $B_\perp$ and $B_\parallel$ represent plane-wave eigenmodes reflected off the interface.

On the other hand, the chiral medium is circularly birefringent; hence the plane waves in the regions $z \leqslant 0$ and $z \geqslant d$ are circularly polarized and the field represen-

tation is somewhat more complicated. The transformation properties of the electric and the magnetic fields in a chiral medium are given by [72, 73, 74]

$$\begin{pmatrix} \boldsymbol{E} \\ \boldsymbol{H} \end{pmatrix} = \boldsymbol{A} \begin{pmatrix} \boldsymbol{Q}_- \\ \boldsymbol{Q}_+ \end{pmatrix}, \tag{2.28}$$

where

$$\boldsymbol{A} = \begin{pmatrix} 1 & a_+ \\ a_- & 1 \end{pmatrix} \tag{2.29}$$

with $\boldsymbol{Q}_-$ and $\boldsymbol{Q}_+$ being the left and the right-circularly polarized plane waves, respectively. The parameters, a_- and a_+ in Eqs (2.29) can be obtained explicitly by diagonalizing $\mathbf{K}$ in Eq. (2.22), i.e.,

$$\boldsymbol{A}^{-1}\boldsymbol{K}\boldsymbol{A} = \begin{pmatrix} -\nu^- & 0 \\ 0 & \nu^+ \end{pmatrix}. \tag{2.30}$$

$$a_+ = \frac{i\nu_+ - \frac{\omega}{c}\kappa_{EH}}{\omega\epsilon_0\epsilon}, \tag{2.31a}$$

$$a_- = \frac{i\nu_- - \frac{\omega}{c}\kappa_{HE}}{\omega\mu_0\mu}. \tag{2.31b}$$

Therefore, the transformed fields,$\boldsymbol{Q}_-$ and $\boldsymbol{Q}_+$ satisfy Maxwell equations in the homogeneous chiral medium and the electromagnetic field can be decomposed into two eigenmodes corresponding to the left- and right- circularly polarized waves, and independently satisfy equations of the form

$$(\nabla^2 + \nu_-^2)\boldsymbol{Q}_- = 0, \qquad (\nabla^2 + \nu_+^2)\boldsymbol{Q}_+ = 0 \tag{2.32a}$$

$$\nabla \times \boldsymbol{Q}_- = -\nu_- \boldsymbol{Q}_-, \quad \nabla \times \boldsymbol{Q}_+ = \nu_+ \boldsymbol{Q}_+, \quad \nabla \cdot \boldsymbol{Q}_- = 0, \quad \nabla \cdot \boldsymbol{Q}_+ = 0, \tag{2.32b}$$

where the transform fields in equation (2.28) may be represented by using the vectors

$$\begin{aligned}\boldsymbol{Q}_- =& [\{A_1(\boldsymbol{t}_{0-} + i\boldsymbol{p}_{1-})\}\exp(-i\gamma_{1z}z) \\ &+ \{B_1(\boldsymbol{t}_{0+} + i\boldsymbol{p}_{1+})\}\exp(i\gamma_{1z}z)]\exp[i(k_x x + k_y y)], \qquad z \geqslant 0,\end{aligned} \tag{2.33a}$$

$$\begin{aligned}\boldsymbol{Q}_+ =& [\{A_2(\boldsymbol{t}_{0-} - i\boldsymbol{p}_{2-})\}\exp(-i\gamma_{2z}z) \\ &+ \{B_2(\boldsymbol{t}_{0+} - i\boldsymbol{p}_{2+})\}\exp(i\gamma_{2z}z)]\exp[i(k_x x + k_y y)], \qquad z \geqslant 0,\end{aligned} \tag{2.33b}$$

where $\boldsymbol{Q}_-$ and $\boldsymbol{Q}_+$, respectively, represent left-circularly and right-circularly polarized plane waves. The coefficients A_1 and A_2 represent plane-wave eigenmodes incident on the interface, while B_1 and B_2 represent the plane-wave eigenmodes reflected off into the chiral half-space as defined in figure (2.6). Here,

$$\boldsymbol{p}_{1\pm}\{k_x, k_y\} = -(\pm\frac{\gamma_{1z}}{k_\parallel \beta_1})(k_x \boldsymbol{e}_x + k_y \boldsymbol{e}_y) + (\frac{k_\parallel}{\beta_1})\boldsymbol{e}_z \quad , \tag{2.34a}$$

$$\boldsymbol{p}_{2\pm}\{k_x, k_y\} = -(\pm\frac{\gamma_{2z}}{k_\parallel \beta_2})(k_x \boldsymbol{e}_x + k_y \boldsymbol{e}_y) + (\frac{k_\parallel}{\beta_2})\boldsymbol{e}_z \quad , \tag{2.34b}$$

$$\gamma_{1z}\{k_x, k_y\} = \sqrt{\beta_1^2 - k_\parallel^2} \quad , \tag{2.34c}$$

$$\gamma_{2z}\{k_x, k_y\} = \sqrt{\beta_2^2 - k_\parallel^2} \quad . \tag{2.34d}$$

Application of the boundary conditions at the interfaces, the boundary-value problem is solved by ensuring the continuity of the tangential components of the $\boldsymbol{E}$ and the $\boldsymbol{H}$ fields across the interface $z = 0$ [75, 76]. The resulting solutions is stated in matrix relations as follows:

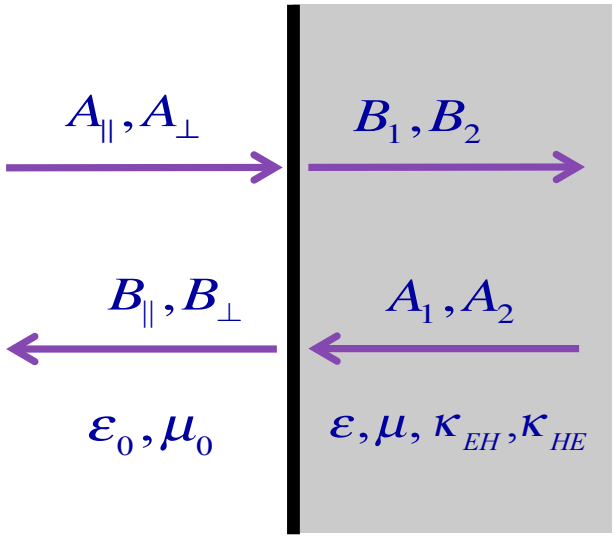

Figure 2.6: The boundary conditions at the interfaces with multipole reflection and transmission coefficients.

$$\begin{bmatrix} B_\perp \\ B_\| \end{bmatrix} = \begin{bmatrix} r_{11} & r_{12} \\ r_{21} & r_{22} \end{bmatrix} \begin{bmatrix} A_\perp \\ A_\| \end{bmatrix} + \begin{bmatrix} T_{11} & T_{12} \\ T_{21} & T_{22} \end{bmatrix} \begin{bmatrix} A_1 \\ A_2 \end{bmatrix} \tag{2.35a}$$

$$\begin{bmatrix} B_1 \\ B_2 \end{bmatrix} = \begin{bmatrix} R_{11} & R_{12} \\ R_{21} & R_{22} \end{bmatrix} \begin{bmatrix} A_1 \\ A_2 \end{bmatrix} + \begin{bmatrix} t_{11} & t_{12} \\ t_{21} & t_{22} \end{bmatrix} \begin{bmatrix} A_\perp \\ A_\| \end{bmatrix} \tag{2.35b}$$

The various Fresnel reflection and transmission coefficients utilized in equations (2.35a) and (2.35b) are given as follows:

$$\Delta r_{11} = -i\eta_0(\zeta_-\zeta_+ - 1)(a_-a_+ - 1) - (\zeta_- + \zeta_+)(a_-\eta_0^2 - a_+), \tag{2.36a}$$

$$\Delta r_{22} = -i\eta_0(\zeta_-\zeta_+ - 1)(a_-a_+ - 1) + (\zeta_- + \zeta_+)(a_-\eta_0^2 - a_+), \tag{2.36b}$$

$$\Delta r_{12} = -2\eta_0(a_- a_+ \zeta_- + \zeta_+), \tag{2.36c}$$

$$\Delta r_{21} = -2\eta_0(a_- a_+ \zeta_+ + \zeta_-), \tag{2.36d}$$

$$\Delta t_{11} = -2i(\eta_0 + i a_+ \zeta_+), \tag{2.36e}$$

$$\Delta t_{12} = -2i(a_+ - i\eta_0 \zeta_+), \tag{2.36f}$$

$$\Delta t_{21} = 2(\zeta_- + i a_- \eta_0), \tag{2.36g}$$

$$\Delta t_{22} = 2i(1 + i\eta_0 a_- \zeta_-), \tag{2.36h}$$

$$\Delta R_{11} = i\eta_0(\zeta_-\zeta_+ - 1)(a_- a_+ - 1) + (\zeta_- - \zeta_+)(a_-\eta_0^2 + a_+), \tag{2.36i}$$

$$\Delta R_{12} = -2\zeta_+(\eta_0^2 + a_+^2), \tag{2.36j}$$

$$\Delta R_{21} = -2\zeta_-(1 + \eta_0^2 a_-^2), \tag{2.36k}$$

$$\Delta R_{22} = i\eta_0(\zeta_-\zeta_+ - 1)(a_- a_+ - 1) - (\zeta_- - \zeta_+)(a_-\eta_0^2 + a_+), \tag{2.36l}$$

$$\Delta T_{11} = -2\eta_0\zeta_-(a_-\eta_0 - i\zeta_+)(a_- a_+ - 1), \tag{2.36m}$$

$$\Delta T_{12} = 2i\eta_0\zeta_+(a_+\zeta_- - i\eta_0)(a_- a_+ - 1), \tag{2.36n}$$

$$\Delta T_{21} = -2\eta_0\zeta_-(1 + i a_-\eta_0\zeta_+)(a_- a_+ - 1), \tag{2.36o}$$

$$\Delta T_{22} = -2\eta_0\zeta_+(i\eta_0\zeta_- - a_+)(a_- a_+ - 1), \tag{2.36p}$$

where

$$\Delta = i\eta_0(\zeta_-\zeta_+ + 1)(a_- a_+ - 1) + (\zeta_- + \zeta_+)(a_-\eta_0^2 + a_+), \tag{2.36q}$$

$$\zeta_- = \frac{k_0}{\beta_1}\frac{\gamma_{1z}}{k_{0z}}, \tag{2.36r}$$

$$\zeta_+ = \frac{k_0}{\beta_2}\frac{\gamma_{2z}}{k_{0z}}. \tag{2.36s}$$

In the next section we introduce an atomic medium that has the characteristics

of chirality, and consequently the off-diagonal coefficients of the reflection matrix survive.

2.4 Atomic chiral medium - dysprosium

2.4.1 Model and Hamiltonian

In this section, we study the atomic level scheme used as the chiral medium. The key idea behind the chiral approach is that, in the optical regime the typical transition magnetic dipole moments are smaller than the corresponding transition electric dipole moments by a factor of the order of the fine structure constant $\alpha \simeq 1/137$. As a consequence, magnetic susceptibilities χ_m are much smaller than the electric susceptibilities χ_e: $\mid \chi_m \mid \sim \alpha^2 \mid \chi_e \mid$. However, in a chiral medium, the magnetic response arising from such a cross coupling is only suppressed by a factor on the order of α and the chirality coefficients can scale as $\kappa_{EH}, \kappa_{HE} \sim \alpha\chi_e$.

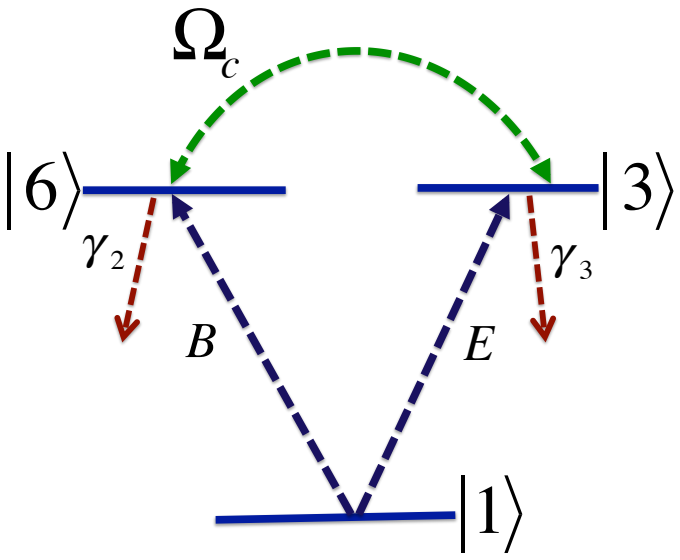

Figure 2.7: Simplistic three-level system for electromagnetically induced chirality. In this scheme, $\boldsymbol{E}$, $\boldsymbol{B}$ are the electric, magnetic components of the probe field, which can experience negative refraction. Ω_c denotes the Rabi frequency of an applied field.

The level configuration of atoms under consideration is illustrated in figure (2.7). The atomic level scheme is originally a three-level system (consisting of level $|6\rangle$, $|3\rangle$, and $|1\rangle$) with Ω_c coupling levels $|6\rangle$ and $|3\rangle$.

However, the system has to be realizable in a realistic media. The energy level structure must be appropriate for media of interest (atoms, molecules, etc.). For these reasons, it is required that the levels $|6\rangle$ and $|3\rangle$ are non-degenerate. To achieve this we need to include the Raman transition to allow a new atomic transition from $|8\rangle$ to $|3\rangle$. As a result, we are able to come up with the required transition, i.e., the electric and magnetic transitions do not share a common state while the transition frequencies are still degenerate. Furthermore, the phase of Ω_c must be adjusted to control the chirality coefficients. These requirements can be resolved by modifies the level scheme of the three-level system to the structure that is shown in figure (2.8) which includes the full Zeeman sublevel structure.

Here, the ground state $|1\rangle$ is replaced by the dark state $|D\rangle$ of the three-level Λ-type subsystem consisting of levels $|1\rangle$, $|8\rangle$, $|9\rangle$ prepared by the two strong control fields Ω_1 and Ω_2, i.e.,

$$|D\rangle = \frac{(\Omega_2|1\rangle - \Omega_1|8\rangle)}{\sqrt{\Omega_1^2 + \Omega_2^2}} \tag{2.37}$$

In figure (2.8) the electric component of the probe field has a transition from the dark state to states $|2\rangle$ and $|4\rangle$ and the magnetic component a transition to level $|5\rangle$ and $|7\rangle$. Thus, the scheme utilizes the dark state of electromagnetically induced transparency (EIT) in order to adjust Ω_c and then to reduce the absorption while enhancing the chiral response. This scheme was first introduced in the context of generating atomic media displaying a negative index of refraction with minimal absorption in [67].

According to the selection rules $\triangle l = \pm 1$, $\triangle S = 0$, and $\triangle J = 0, \pm 1$, magnetic dipole transitions can solely occur between states that have the same parity and

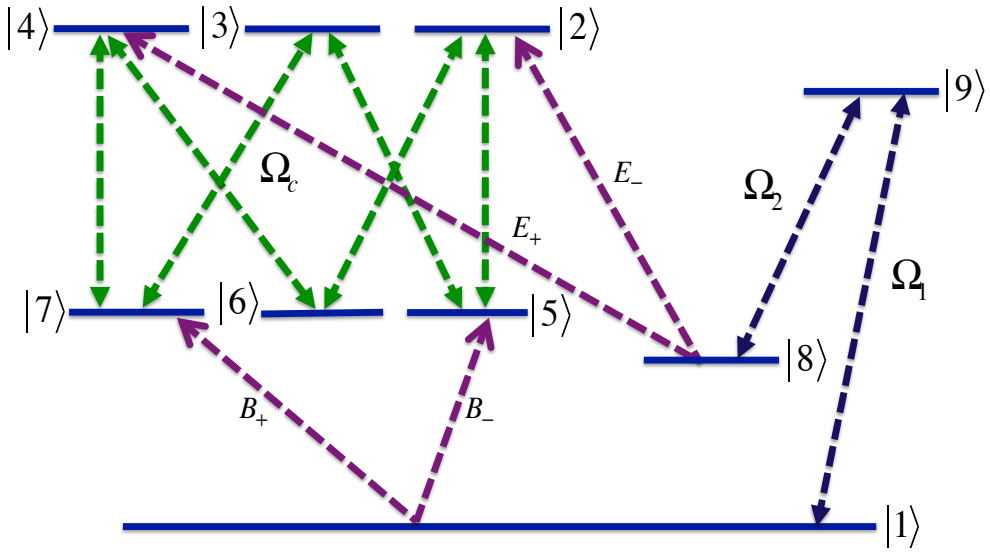

Figure 2.8: Five-level scheme that includes the full Zeeman sublevel structure. Two strong control fields with Rabi frequencies Ω_1 and Ω_2 prepare the atoms in a coherent superposition states $|1\rangle$ and $|8\rangle$. The two circular polarizations of a probe field traveling in z direction with electric E_+, E_- and magnetic B_+, B_- components are used to generate electric dipole transitions to levels $|2\rangle$, $|4\rangle$ and magnetic dipole transitions to levels $|5\rangle$, $|7\rangle$, respectively. The upper levels are coupled by the resonant control field with Rabi frequencies Ω_c (dashed green).

the same main quantum number whereas electric dipole transitions occur between states of different parity and different main quantum number. We believe that the existing works on the rare-earth metals atomic species such as dysprosium (Dy) may be applicable for an experimental implementation for the study of repulsive Casimir force. In this work [77], we have chosen the appropriate combination of the actual level scheme of Dy consistent with the selection rules and the demands of parity: e.g., a probe field at $600nm$ with the $E1$ transition between $4f^{10}5d6s$, $J = 8$ and $4f^{9}5d^{2}6s$, $J = 7$ and the $M1$ transition between $4f^{10}6s6p$, $J = 7$ and $4f^{10}6s6p$, $J = 6$ [67]. The formula (2.25) for a particular polarization gives a freedom to switch the magnitude of the refractive index from positive to negative sign by controlling

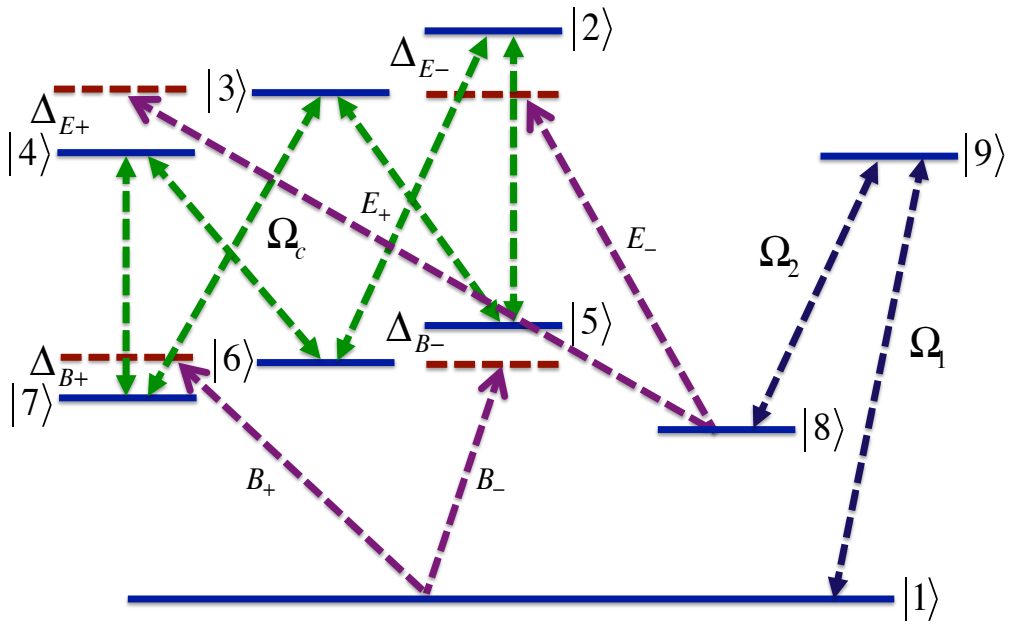

Figure 2.9: Atomic level configuration with characteristic of a chiral medium with two different refractive indices. An external magnetic field B is applied to the atomic levels of figure (2.8) leading to splitting the detuning for the two circularly polarizations.

the phases of the chirality coefficients without requiring both $\epsilon < 0$ and $\mu < 0$. For example, if we set the phase ϕ of the strong coupling laser, i.e., Ω_c, such that the chirality coefficients are imaginary and bi-isotropic medium reduces to a chiral reciprocal medium, $\kappa_{EH} = -\kappa_{HE} = i\kappa$, with $\kappa > 0$, the refractive index (2.25) can be expressed as $n^- = \sqrt{\epsilon\mu} - \kappa$ for a particular polarization. It is possible to see that the refractive index is increased for one circular polarization wave and reduced for the other. Nonetheless, in the literature these potentials are restricted to a particular direction of propagation either for right circular polarization (e+) or left circular polarization (e-) [67, 71]. In this work, we have considered the generalization relation (2.25) to arbitrary polarizations. An external magnetic field is applied to the chiral material in order to break the symmetry. This leads to Zeeman effect as illustrated in figure 2.9. As a consequence, the condition that a natural chiral medium

should have different refractive indices is satisfied. The three-level subsystem $|1\rangle$, $|8\rangle$, and $|9\rangle$) can be solved undisturbed by the probe field corresponding to the pure state $|D\rangle$ via $\rho = |D\rangle\langle D|$, where $|D\rangle = (\Omega_2|1\rangle - \Omega_1|8\rangle)/\sqrt{\Omega_1^2 + \Omega_2^2}$. The detunings of the applied fields are defined as $\Delta E_- = \omega_{28} - \omega_p, \Delta E_+ = \omega_p - \omega_{48}, \Delta B_- = \omega_{51} - \omega_p, \Delta B_+ = \omega_p - \omega_{71}$, and $\delta_c = 0$. We calculate the microscopic properties of the medium, i.e., the permittivity, the permeability, and the chirality coefficients in the linear approximation.

By taking into account the fully coupling Rabi frequencies, the Hamiltonian $H = H_{\text{atom}} - \boldsymbol{d} \cdot \boldsymbol{E}(t) - \boldsymbol{\mu} \cdot \boldsymbol{B}(t)$ of the system can be written explicitly as

$$\begin{aligned} H = & \sum_{n=1}^{9} \hbar\omega_n^A |n\rangle \langle n| + \Bigg\{ -\frac{1}{2} d_{28} E_- e^{-i\omega_p t} |2\rangle \langle 8| - \frac{1}{2} d_{48} E_+ e^{-i\omega_p t} |4\rangle \langle 8| \\ & - \frac{1}{2}\mu_{51} B_- e^{-i\omega_p t} |5\rangle \langle 1| - \frac{1}{2}\mu_{71} B_+ e^{-i\omega_p t} |7\rangle \langle 1| - \frac{\hbar}{2}\Omega_c e^{-i\omega_c t} |4\rangle \langle 7| \\ & - \frac{\hbar}{2}\Omega_c e^{-i\omega_c t} |4\rangle \langle 6| - \frac{\hbar}{2}\Omega_c e^{-i\omega_c t} |3\rangle \langle 7| - \frac{\hbar}{2}\Omega_c e^{-i\omega_c t} |3\rangle \langle 5| \\ & - \frac{\hbar}{2}\Omega_c e^{-i\omega_c t} |2\rangle \langle 6| - \frac{\hbar}{2}\Omega_c e^{-i\omega_c t} |2\rangle \langle 5| - \frac{\hbar}{2}\Omega_1 e^{-i\omega_1 t} |9\rangle \langle 1| \\ & - \frac{\hbar}{2}\Omega_2 e^{-i\omega_2 t} |9\rangle \langle 8| + H.C. \Bigg\}, \end{aligned} \tag{2.38}$$

where $d_{ij} = \langle i| e\boldsymbol{r}.\hat{\boldsymbol{e}}_{\boldsymbol{E}} |j\rangle$ and $\mu_{ij} = \langle i| \boldsymbol{\mu}.\hat{\boldsymbol{e}}_{\boldsymbol{B}} |j\rangle$ are the electric and magnetic dipole moments and E and B are the electric and magnetic components of the probe field with frequency ω_p. The Rabi frequencies Ω_1, Ω_2, and Ω_c belong to strong coupling lasers which oscillate at ω_1, ω_2, and ω_c, respectively. The strong coupling Rabi frequency Ω_c is chosen to be complex for the closed loop scheme. The energy of state $|i\rangle$ is given by $\hbar\omega_i^A$ with (i=1,2,3,4,5,6,7,8,9). We derive the equations of motion for the slowly varying matrix elements of the density operator of the atom. Here $\gamma_{ij} = [\sum_k (\Gamma_{ik} + \Gamma_{kj})]/2$ is the dephasing rate of atomic coherence ρ_{ij} with $\Gamma_{ij} =$

$\langle i|\,\Gamma\,|j\rangle = \gamma_i\delta_{ij}$ being the population decay rate from level $|i\rangle$ to level $|j\rangle$.

2.4.2 Equations of motion

The equations of motion can be obtained analytically using the Liouville equation of motion for the density matrix $\dot{\rho} = -i\hbar^{-1}[H,\rho] - 2^{-1}\{\Gamma,\rho\}$ [78]. Here, the ijth matrix element is given as

$$\dot{\rho}_{ij} = -\frac{i}{\hbar}\sum_k (H_{ik}\rho_{kj} - \rho_{ik}H_{kj}) - \frac{1}{2}\sum_k (\Gamma_{ik}\rho_{kj} + \rho_{ik}\Gamma_{kj}). \tag{2.39}$$

$$i\dot{\tilde{\rho}}_{28} = (\Delta E_- - i\gamma_{28})\tilde{\rho}_{28} - \frac{d_{28}E_-}{2\hbar}\tilde{\rho}_{88} - \frac{\Omega_c}{2}\tilde{\rho}_{58}, \tag{2.40a}$$

$$i\dot{\tilde{\rho}}_{51} = (\Delta B_- - i\gamma_{51})\tilde{\rho}_{51} - \frac{\mu_{51}B_-}{2\hbar}\tilde{\rho}_{11} - \frac{\Omega_c^*}{2}\tilde{\rho}_{21}, \tag{2.40b}$$

$$i\dot{\tilde{\rho}}_{58} = (\Delta E_- - i\gamma_{58})\tilde{\rho}_{58} - \frac{\mu_{51}B_-}{2\hbar}\tilde{\rho}_{18} - \frac{\Omega_c^*}{2}\tilde{\rho}_{28}, \tag{2.40c}$$

$$i\dot{\tilde{\rho}}_{21} = (\Delta B_- - i\gamma_{21})\tilde{\rho}_{21} - \frac{d_{28}E_-}{2\hbar}\tilde{\rho}_{81} - \frac{\Omega_c}{2}\tilde{\rho}_{51}, \tag{2.40d}$$

$$i\dot{\tilde{\rho}}_{48} = (-\Delta E_+ - i\gamma_{48})\tilde{\rho}_{48} - \frac{d_{48}E_+}{2\hbar}\tilde{\rho}_{88} - \frac{\Omega_c}{2}\tilde{\rho}_{78}, \tag{2.40e}$$

$$i\dot{\tilde{\rho}}_{71} = (-\Delta B_+ - i\gamma_{71})\tilde{\rho}_{71} - \frac{\mu_{71}B_+}{2\hbar}\tilde{\rho}_{11} - \frac{\Omega_c^*}{2}\tilde{\rho}_{41}, \tag{2.40f}$$

$$i\dot{\tilde{\rho}}_{78} = (-\Delta E_+ - i\gamma_{78})\tilde{\rho}_{78} - \frac{\mu_{71}B_+}{2\hbar}\tilde{\rho}_{18} - \frac{\Omega_c^*}{2}\tilde{\rho}_{48}, \tag{2.40g}$$

$$i\dot{\tilde{\rho}}_{41} = (-\Delta B_+ - i\gamma_{41})\tilde{\rho}_{41} - \frac{d_{48}E_+}{2\hbar}\tilde{\rho}_{81} - \frac{\Omega_c}{2}\tilde{\rho}_{71}. \tag{2.40h}$$

Here $\gamma_{ij} = [\sum_k(\Gamma_{ik} + \Gamma_{kj})]/2$ is the dephasing rate of atomic coherence ρ_{ij} with $\Gamma_{ij} = \langle i|\,\Gamma\,|j\rangle = \gamma_i\delta_{ij}$ being the population decay rate from level $|i\rangle$ to level $|j\rangle$.

By transforming the equations of motion into a rotating frame and solving these equations in linear response we get

$$\tilde{\rho}_{28} = \frac{2id_{28}\gamma_{58}E_{-}\rho_{88}^{(0)} - 2d_{28}\Delta E_{-}E_{-}\rho_{88}^{(0)} - \mu_{51}\rho_{18}^{(0)}\Omega_c B_{-}}{\hbar(4\gamma_{58}\gamma_{28} + 4i(\gamma_{58}+\gamma_{28})\Delta E_{-} - 4\Delta E_{-}^2 + \mid \Omega_c \mid^2}, \tag{2.41a}$$

$$\tilde{\rho}_{51} = \frac{2i\mu_{51}\gamma_{21}B_{-}\rho_{11}^{(0)} - 2\mu_{51}\Delta B_{-}B_{-}\rho_{11}^{(0)} - d_{28}\rho_{81}^{(0)}\Omega_c E_{-}}{\hbar(4\gamma_{21}\gamma_{51} + 4i(\gamma_{21}+\gamma_{51})\Delta B_{-} - 4\Delta B_{-}^2 + \mid \Omega_c \mid^2}, \tag{2.41b}$$

$$\tilde{\rho}_{48} = \frac{2id_{48}\gamma_{78}E_{+}\rho_{88}^{(0)} + 2d_{48}\Delta E_{+}E_{+}\rho_{88}^{(0)} - \mu_{71}\rho_{18}^{(0)}\Omega_c B_{+}}{\hbar(4\gamma_{48}\gamma_{78} - 4i(\gamma_{48}+\gamma_{78})\Delta E_{+} - 4\Delta E_{+}^2 + \mid \Omega_c \mid^2}, \tag{2.41c}$$

$$\tilde{\rho}_{71} = -\frac{2i\mu_{71}\gamma_{41}B_{+}\rho_{11}^{(0)} - 2\mu_{71}\Delta B_{+}B_{+}\rho_{11}^{(0)} + d_{48}\rho_{81}^{(0)}\Omega_c E_{+}}{\hbar(-4\gamma_{41}\gamma_{71} + 4i(\gamma_{41}+\gamma_{71})\Delta B_{+} + 4\Delta B_{+}^2 - \mid \Omega_c \mid^2}. \tag{2.41d}$$

2.4.3 Chirality coefficients

The ensemble electric polarization $\boldsymbol{P}$ and magnetization $\boldsymbol{M}$ of the atomic medium at the probe field frequency are given by

$$\boldsymbol{P_{-}} = Nd_{28}\tilde{\rho}_{28} = N\alpha_{-}^{EE}\boldsymbol{E_{-}} + N\alpha_{-}^{EB}\boldsymbol{B_{-}}, \tag{2.42a}$$

$$\boldsymbol{M_{-}} = N\mu_{51}\tilde{\rho}_{51} = N\alpha_{-}^{BE}\boldsymbol{E_{-}} + N\alpha_{-}^{BB}\boldsymbol{B_{-}}, \tag{2.42b}$$

$$\boldsymbol{P_{+}} = Nd_{48}\tilde{\rho}_{48} = N\alpha_{+}^{EE}\boldsymbol{E_{+}} + N\alpha_{+}^{EB}\boldsymbol{B_{+}}, \tag{2.42c}$$

$$\boldsymbol{M_{+}} = N\mu_{71}\tilde{\rho}_{71} = N\alpha_{+}^{BE}\boldsymbol{E_{+}} + N\alpha_{+}^{BB}\boldsymbol{B_{+}}, \tag{2.42d}$$

where N is the density of the atoms.

Substituting the Eqs. (2.41) back to the density matrices $\tilde{\rho}_{28}, \tilde{\rho}_{51}, \tilde{\rho}_{48}, \tilde{\rho}_{71}$ we arrive at the cross-coupling polarizabilities as

$$\alpha_{-}^{EE} = \frac{i}{2\hbar}\frac{d_{28}^2\rho_{88}^{(0)}(\gamma_{85} + i\Delta E_{-})}{(\gamma_{85} + i\Delta E_{-})(\gamma_{28} + i\Delta E_{-}) + \mid \Omega_c \mid^2/4}, \tag{2.43a}$$

$$\alpha_{-}^{EB} = -\frac{1}{4\hbar}\frac{d_{28}\mu_{51}\rho_{81}^{(0)}\Omega_c}{(\gamma_{85}+i\Delta E_{-})(\gamma_{28}+i\Delta E_{-})+\mid\Omega_c\mid^2/4}, \tag{2.43b}$$

$$\alpha_{-}^{BB} = \frac{i}{2\hbar}\frac{\mu_{51}^2\rho_{11}^{(0)}(\gamma_{21}+i\Delta B_{-})}{(\gamma_{21}+i\Delta B_{-})(\gamma_{51}+i\Delta B_{-})+\mid\Omega_c\mid^2/4}, \tag{2.43c}$$

$$\alpha_{-}^{BE} = -\frac{1}{4\hbar}\frac{d_{28}\mu_{51}\rho_{81}^{(0)}\Omega_c^*}{(\gamma_{21}+i\Delta B_{-})(\gamma_{51}+i\Delta B_{-})+\mid\Omega_c\mid^2/4}. \tag{2.43d}$$

$$\alpha_{+}^{EE} = \frac{i}{2\hbar}\frac{d_{48}^2\rho_{88}^{(0)}(\gamma_{78}-i\Delta E_{+})}{(\gamma_{48}-i\Delta E_{+})(\gamma_{78}-i\Delta E_{+})+\mid\Omega_c\mid^2/4}, \tag{2.44a}$$

$$\alpha_{+}^{EB} = -\frac{1}{4\hbar}\frac{d_{48}\mu_{71}\rho_{18}^{(0)}\Omega_c}{(\gamma_{48}-i\Delta E_{+})(\gamma_{78}-i\Delta E_{+})+\mid\Omega_c\mid^2/4}, \tag{2.44b}$$

$$\alpha_{+}^{BB} = \frac{i}{2\hbar}\frac{\mu_{71}^2\rho_{11}^{(0)}(\gamma_{41}-i\Delta B_{+})}{(\gamma_{71}-i\Delta B_{+})(\gamma_{41}-i\Delta B_{+})+\mid\Omega_c\mid^2/4}, \tag{2.44c}$$

$$\alpha_{+}^{BE} = -\frac{1}{4\hbar}\frac{d_{48}\mu_{71}\rho_{81}^{(0)}\Omega_c^*}{(\gamma_{71}-i\Delta B_{+})(\gamma_{41}-i\Delta B_{+})+\mid\Omega_c\mid^2/4}. \tag{2.44d}$$

Here, α^{EE}, α^{BB}, are the polarizabilities and α^{EB}, and α^{BE} are the cross-coupling polarizabilities.

We would like to emphasize that the strong resonant coherent coupling field between the upper states with a Rabi frequency Ω_c is added in order to induce a cross coupling in the sense of Eqs. (2.19). In view of this, it is possible to observe that these cross couplings are proportional to the strength of the ground state coherence of sates $|8\rangle$ and $|1\rangle$ and the coherent control field Ω_c. This can be readily seen from Eqs. (2.44). Therefore, by adjusting Ω_c, the phase of the magneto electric cross couplings (chirality) can be readily controlled. For instance for $\Omega_c = 0$ the cross coupling coefficients α_{EB} and α_{BE} vanish.

2.4.4 Local-field corrections

In calculating the susceptibilities and chirality coefficients, we have included both electric and magnetic Clausius-Mossotti type local-field corrections [79, 80, 81, 82] by replacing the macroscopic field quantities in Eqs. (2.42) by the microscopic fields given by

$$\boldsymbol{E}^{micro} = \boldsymbol{E} + \frac{1}{3\epsilon_0}\boldsymbol{P}, \tag{2.45a}$$

$$\boldsymbol{H}^{micro} = \boldsymbol{H} + \frac{1}{3}\boldsymbol{M}. \tag{2.45b}$$

On substituting the relations $\boldsymbol{D} = \epsilon_0\boldsymbol{E} + \boldsymbol{P}$ and $\boldsymbol{B} = \mu_0(\boldsymbol{H} + \boldsymbol{M})$ into Eqs. (2.42) together with Eqs. (2.45) and Eq. (2.19), we obtain the following expressions for the permittivity, the permeability, and the chirality coefficients:

$$\epsilon^{\pm} = 1 + \frac{N}{\epsilon_0 L^{loc}}\{\alpha^{\pm}_{EE} + \frac{N}{3}\mu_0(\alpha^{\pm}_{EB}\alpha^{\pm}_{BE} - \alpha^{\pm}_{EE}\alpha_{BB})\}, \tag{2.46a}$$

$$\mu^{\pm} = 1 + \frac{N\mu_0}{L^{loc}}\{\alpha^{\pm}_{BB} + \frac{N}{3\epsilon_0}(\alpha^{\pm}_{EB}\alpha^{\pm}_{BE} - \alpha^{\pm}_{EE}\alpha_{BB})\}, \tag{2.46b}$$

$$\kappa^{\pm}_{EH} = \sqrt{\frac{\mu_0}{\epsilon_0}}\frac{N\alpha^{\pm}_{EB}}{L^{loc}}, \tag{2.46c}$$

$$\kappa^{\pm}_{HE} = \sqrt{\frac{\mu_0}{\epsilon_0}}\frac{N\alpha^{\pm}_{BE}}{L^{loc}}, \tag{2.46d}$$

where

$$\begin{aligned} L^{loc} =& 1 - \frac{N}{3}\frac{1}{\epsilon_0}\alpha^{\pm}_{EE} - \frac{N}{3}\mu_0\alpha^{\pm}_{BB} \\ & - \left(\ \tfrac{N}{3}\ \right)^2 \frac{\mu_0}{\epsilon_0}(\alpha^{\pm}_{EB}\alpha^{\pm}_{BE} - \alpha^{\pm}_{EE}\alpha_{BB}). \end{aligned} \tag{2.47}$$

Once we have the solutions of $\epsilon^{\pm}$, $\mu^{\pm}$, $\kappa_{EH}^{\pm}$, and $\kappa_{HE}^{\pm}$, we can now proceed to study the influence of a chiral atomic medium on the Casimir force.

A chiral medium should have different response to a left and a right circularly polarized field, i.e., $n^- \neq n^+$, and this is what we have obtained in the case of non-zero magnetic field. Consequently, the off-diagonal coefficients of the reflection matrix survive and our atomic medium has the characteristics of chirality.

In the next section we investigate the Casimir force or the Casimir interaction energy dynamics based on a coherently prepared chiral atomic medium and show that the Casimir interaction energy can be controlled via controlling the magnetic field.

2.5 Results and discussions

In this section we present and discuss results for the Casimir force. For this purpose, in the numerical calculations we have chosen typical parameters to calculate the polarizabilities in Eqs. (2.43) and (2.44) [67, 66]. The spontaneous emission rates and the Rabi frequencies are taken as $\gamma_5 = 10^2 s^{-1}, \gamma_7 = 2 \times 10 s^{-1}, \gamma_2 = 137^2\gamma_5, \gamma_9 = 137^2\gamma_5, \gamma_1 = \gamma_8 = 0, \Omega_1 = \Omega_2 = 10^6 s^{-1}$. The electric and magnetic dipole matrix elements can be expressed as $d_{28(48)} = \sqrt{3\epsilon_0\hbar\gamma_2(\gamma_4)\lambda^3/8\pi^2}$, $\mu_{51(71)} = c\sqrt{3\epsilon_0\hbar\gamma_5(\gamma_7)\lambda^3/8\pi^2}$. Here $N = 1 \times 10^{22}/m^3$ and $\lambda = 600nm$ for a typical optical wavelength. The coupling Rabi frequencies are chosen to be $\Omega_c^- = 10^4\gamma_5 e^{i\frac{\pi}{2}}$ and $\Omega_c^+ = 10^4\gamma_7 e^{i\frac{\pi}{2}}$. The frequency shifts, as a consequence of Zeeman effect, are given by $(m_J g_J - m'_J g'_J)\mu_B B/\hbar$, where $\mu_B = e\hbar/2m_e = 9.274 \times 10^{-24} JT^{-1}$ is the Bohr-magneton and B is the magnetic field. Here, g_J is called the Lande' g-factor and depends on the spin angular momentum S, the orbital angular momentum L, and the total angular momentum J. The expression of the Lande' g-factor is given by [83]

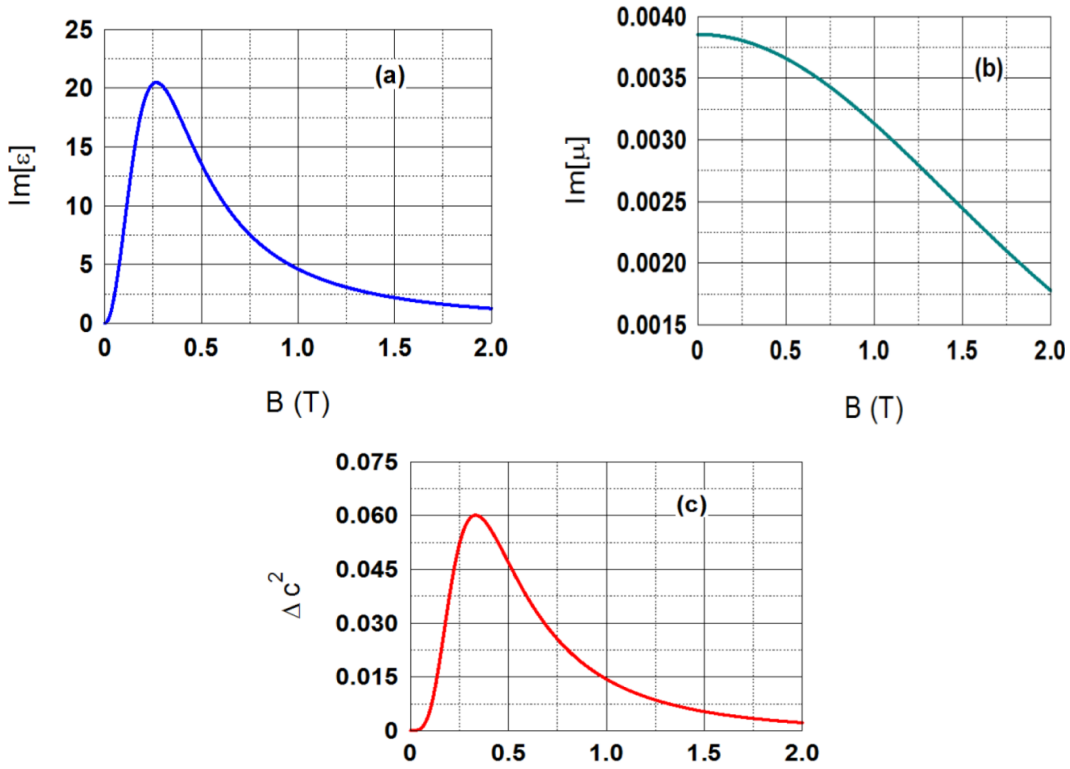

Figure 2.10: Imaginary part of the (a). permittivity $\mathrm{Im}\{\epsilon\}$, (b). permeability $\mathrm{Im}\{\mu\}$, and (c). $\Delta c^2 = [\mathrm{Im}\{\epsilon\}\mathrm{Im}\{\mu\} - (\mathrm{Im}\{\kappa\})^2]$ as a function of the magnetic field.

$$g_J = 1 + \frac{J(J+1) + S(S+1) - L(L+1)}{2J(J+1)} \tag{2.48}$$

In the numerical results, we have considered the level scheme of atomic dysprosium that is mentioned in Sec. IV. According to the selection rules, the quantum number m_J and the gyromagnetic factors g_J can be easily computed. We set $\triangle E \neq \triangle B$ in the numerical calculations.

It is important at this point to emphasize that the integrand $\ln\det\left[1-\boldsymbol{R_1}\boldsymbol{R_2}e^{-2kd}\right]$ in the formula (2.16) is analytical in the upper half space in the complex plan $\mathrm{Re}\,\xi > 0$. The conditions for analyticity in the derivation of the Casimir force are discussed

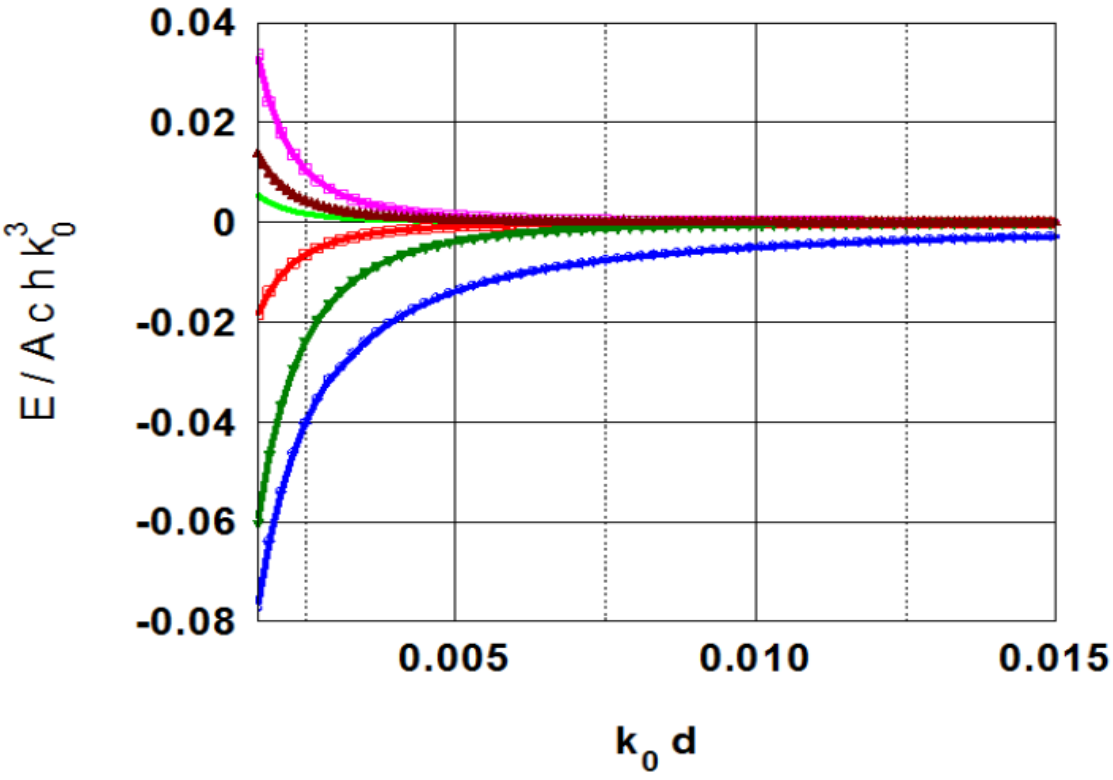

Figure 2.11: Casimir interaction energy E/A per unit area in units of hck_0^3 versus $k_0 d$; where $k_0 = 10^{-2}/\mu m$ for different values of the magnetic field. The first lower circle curve (blue) corresponds to $B = 0$ ($\triangle E_- = \triangle E_+ = \triangle B_- = \triangle B_+$), i.e., $n_+ = n_-$. The subsequent four curves have the following values for the magnetic field: $B = 0.05T$ (dark green), $0.2T$ (red), $1.5T$ (green), $3T$ (brown). The upper curve (pink) corresponds to $5T$ (pink), respectively.

in Ref. [7]. Based on thermodynamical considerations, it is shown in [20] that the conditions for passivity are fulfilled with the following set of inequalities: $\mathrm{Im}\{\epsilon\} > 0$, $\mathrm{Im}\{\mu\} > 0$, and $\Delta > 0$, where $\Delta = \frac{1}{c^2}[\mathrm{Im}\{\epsilon\}\mathrm{Im}\{\mu\} - (\mathrm{Im}\{\kappa\})^2]$. Here κ is the chirality coefficient. We emphasize that our atomic chiral medium fulfills all these necessary and sufficient conditions. Furthermore, we verified numerically that the real and imaginary parts $\epsilon_R(\omega) = \mathrm{Re}\{\epsilon(\omega)\}$ and $\epsilon_I(\omega) = \mathrm{Im}\{\epsilon(\omega)\}$, respectively, are causal and thus satisfy the well-known Kramers-Kronig relations. In Figs. (2.10a-

2.10c) we plot the imaginary part of the permittivity $\mathrm{Im}\{\epsilon\}$, the imaginary part of the permeability $\mathrm{Im}\{\mu\}$, and the determinant of the matrix Δ as a function of the magnetic field B. We can see from these figures that $\mathrm{Im}\{\epsilon\}$, $\mathrm{Im}\{\mu\}$, $\frac{1}{c^2}[\mathrm{Im}\{\epsilon\}\mathrm{Im}\{\mu\} - (\mathrm{Im}\{\kappa\})^2]$, are always positive in agrement with the passivity conditions.

In Fig. (2.11), we plot the Casimir interaction energy E/A per unit area as a function of $k_0 d$; where $k_0 = 10^{-2}/\mu m$ for different values of the magnetic field. First, we consider the case when no external magnetic field is present. In this case $\triangle E_- = \triangle E_+ = \triangle B_- = \triangle B_+ = 0$. This leads to the refractive indices of the left and the right circularly polarizations to be identical, i.e., $n^+ = n^-$. Therefore, there is no chirality and the Casimir force is attractive for all values of d. This result is indicated by the lower circle curve (blue) in Fig. (2.11).

Next, we consider the situation when an external magnetic field is applied to the chiral medium so as to break the symmetry and get different refractive indices, i.e., $n^+ \neq n^-$. The circular polarization components have different refractive indices and the condition of a chiral medium has been fulfilled. We observe from the curves for $B = 0.05T$(the second lower curve), $B = 0.2T$, $B = 1.5T$, $B = 3T$, $B = 5T$ (the upper curve), that a control of the magnetic field can provide sufficient new freedom to derive the force to negative values (i.e., repulsive) at least for some range of values of d. This behavior can be explained using Eqs. (2.16) and (2.17). The Casimir force is minus the slope of this curve. This means that the Casimir force is positive or attractive for values of E that are negative, and the force is negative or repulsive for values of the energy that are positive. It can be easily seen from Fig. (2.11) that, as the magnetic field is increased from $0T$, the Casimir energy increases from a negative maximum, to zero, and then to positive values. The crossover occurs between $0.2T$ and $1.5T$.

In Fig. (2.12) we plot the Casimir interaction energy as a function of the magnetic

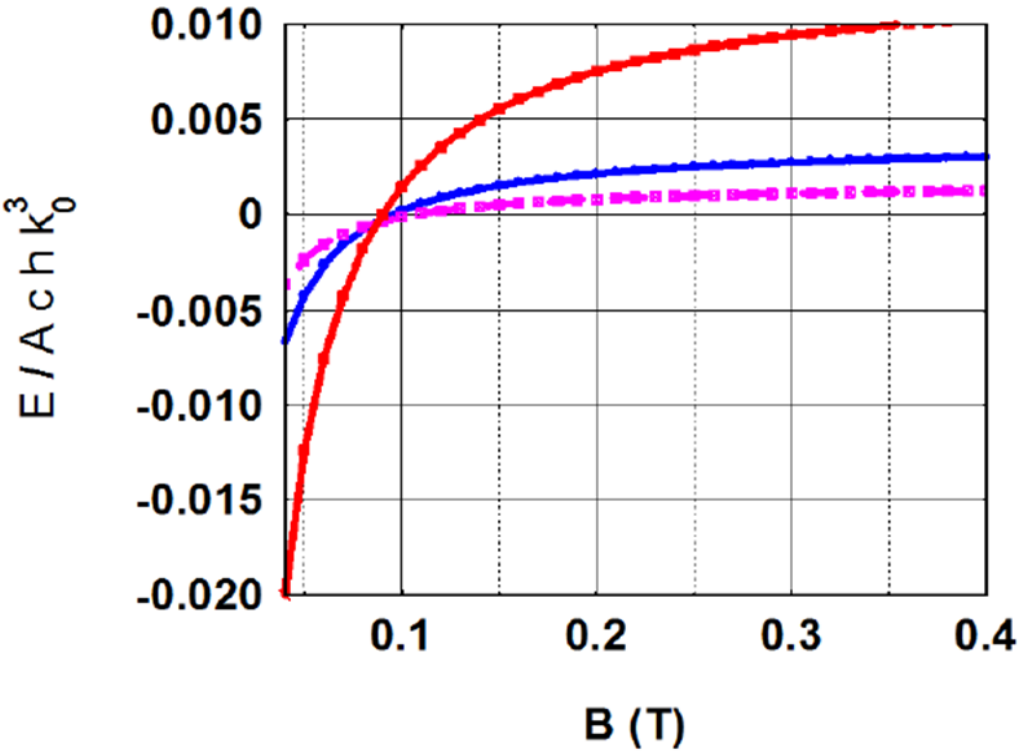

Figure 2.12: Casimir interaction energy E/A per unit area in units of hck_0^3 as a function of the magnetic field B in unit of tesla. The full square lower curve (red) corresponds to $k_0 d = 0.002$, while the circle curve (blue) obtains for $k_0 d = 0.003$, finally, the triangle upper curve (pink) corresponds to $k_0 d = 0.004$.

field for different values of d. We have found that the response of the Casimir force to the magnetic field depends on the values of d between the chiral atomic media.

To summarize the proposal arrangement, we have employed strong coherent Raman coupling with complex Rabi frequencies Ω_1 and Ω_2 to the atomic scheme (consisting of level $|6\rangle$, $|3\rangle$, and $|1\rangle$), which creates a dark superposition of state $|1\rangle$ and $|8\rangle$. This scheme enhances the freedom of choice of energy level structure to be suitable and realizable in a realistic media. The two circular polarizations of a probe field traveling in z direction with electric E_+, E_- and magnetic B_+, B_- components are used to generate electric dipole transitions to levels $|2\rangle$, $|4\rangle$ and magnetic dipole

transitions to levels $|5\rangle$, $|7\rangle$, respectively. Here, the five-level scheme shown in Fig. (2.8) that includes the full Zeeman sublevel structure is placed in an external magnetic field in order to split the detuning as well as the refractive amplitudes for the two circular polarizations, which consequently leads to chirality.

The rare-earth metals atomic species, for instance, dysprosium (Dy), may be an applicable medium for the forthcoming studies of possible experimental implementation of our technique [84]. Dysprosium is a heavy atom and it has many stable isotopes. Numerous combinations of valence electron couplings in Dy atom lead to highly complex multitude of electronic energy levels and therefore a level structure similar to our scheme can be easily found [85]. Furthermore, Dy atom has a large ground-state magnetic dipole moment (10 Bohr magnetons) and thus it serves as a prime candidate for the study of ultracold trapping [86, 87]. Laser cooling technique has been used to trap high-density ultracold atomic clouds at the microKelvin temperatures [85] and it may be suitable for the experimental implementation of our approach.

An alternative method is buffer-gas cooling and magnetic trapping. Through buffer-gas cooling technology [87], cooled magnetically trapped atom clouds may be utilized for experimental implementation of our approach with rare-earth atoms. Buffer-gas cooling and magnetic trapping technology has been used by Hancox et al. to trap $> 10^{11}$ Dy atoms [87]. These densities will likely be possible to increase by performing evaporative cooling in the magnetic trap [87]. They have demonstrated that this machinery may serve as an excellent starting point for producing high-density clouds. These are very exciting advances, and we have the feeling that this technology has a considerable promise for the study of Casimir force. A thorough theoretical modeling to investigate Casimir force with these exiting developments will be among our future investigations.

2.6 Conclusion

In this work we have investigated the Casimir interaction energy with two identical chirality atomic mediums. The five-level system shown in Fig. (2.8) that includes the full Zeeman sublevel structure is placed in an external magnetic field in order to split the detuning as well as the refractive amplitudes for the two circular polarizations, which leads to chirality. We took explicit caution regarding the requirements of passivity and causal response of the materials, since these requirements are essential for the application of the Lifshitz' formula. We have calculated numerically the Casimir interaction energy as a function of the magnetic field and we have shown that the Casimir force can be coherently controlled. Thus, by controlling the applied magnetic field we can switch the sign of the force from plus (i.e., attractive) to minus (i.e., repulsive).

There are many open questions that needs to be addressed. One future direction would be to perform a thorough detailed theoretical modeling to identify the most suitable and applicable atomic species and experimental system for observing repulsive Casimir force. If achieved, we expect that our technique may have potential applications in nanoelectromecanical (NEMS) devices.

3. SPECTRAL PROPERTIES OF A STRONGLY COUPLED QUANTUM DOT-METAL NANOPARTICLE SYSTEM *

3.1 Introduction

In quantum optics, the strong coupling regime can usually be achieved via cavity quantum electrodynamics [21, 22]. However, this approach needs a very high quality factor of a cavity or a small effective mode volume, which are difficult to realize by the conventional methods. Recently, Chang et al. [23, 24] proposed a new method to achieve strong, coherent coupling between individual emitters and electromagnetic excitations in conducting nanostructures at optical frequencies, via excitation of plasmons localized to nanoscale dimensions. This strong coupling is possible due to the small mode volume associated with the subwavelength surface-plasmonic confinement.

The quantum nature of the surface plasmons was demonstrated using energy-loss spectroscopy experiments on thin metallic films as reported by Powell and Swan [25]. Yannopapas et al [88] further showed that the quantum interference between two spontaneous emission channels can be greatly enhanced when a three-level V-type atom is placed near plasmonic nanostructures such as metallic slabs, nanospheres, or periodic arrays of metal-coated spheres. Such enhancement of quantum interference is attributed to the strong anisotropy of the spontaneous emission rates due to the surface plasmons [88, 89, 90]. Through controlling the population distributions of excited states and modifying the decay rate of quantum emitters near plasmon structures, the fluorescence enhancement and quenching effects of molecules and quantum

*Reprinted with permission from "Spectral properties of a strongly coupled quantum-dotmetal-nanoparticle system," by Jabir Hakami, Ligang Wang, and M. Suhail Zubairy, 2014, Phys. Rev. A, vol. 89, p. 053835, copyright [2014] by American Physical Society.

dots (QDs) have been discovered [91]. By confining the light into nanoscale volumes, various plasmonic elements allow for a nanoscale realization of Mollow triplet of emission spectra [92, 93] and non-classical photon correlations between the emissions from the QD and the ends of nanowire [94]. The objective of these investigations is to enhance the local photon density of states to be large enough, leading to the strong coupling regime.

There has been a large number of investigations on the modifications of spontaneous emission and resonance fluorescence of quantum emitters near various plasmonic structures. Moreover, the photon-emitter interaction via sub-wavelength confinement optical fields in the vicinity of metallic nanoscale structure has also been investigated [95, 96].

Metallic nanoparticles (MNPs) are currently attracting intense attention due to their remarkable potentials in physics, chemistry, and life sciences [56, 57]. A MNP supports localized surface plasmons that are tightly confined spatially, which enhance their ability for enhancing and focusing optical fields to spots much smaller than diffraction limit. More recently, Evangelou et al [97] have explored the modification of the spontaneous emission spectrum by the presence of the plasmonic nanostructure. The spontaneous emission spectra emitted by a dipole emitter in the vicinity of a spherical particle has been studied in Ref. [98] via a Green function technique. The authors discussed a coupled MNP and a dipole emitter (e.g., a QD) beyond the dipole approximation where the higher-order mode can not be neglected when the emitter and MNP are in close proximity. This treatment is based on the Markov approximation.

Nanoscale integration of metals and semiconductors is particulary interesting because the strengths of both materials are combined in such a hybrid system [99, 100]. More ornate experiments have demonstrated that localized plasmon fields

near MNPs profoundly modify the optical properties of single emitters (e.g., fluorescence molecules [44, 45], nitrogen vacancy centers in diamond nanocrystals [46], and photoluminescence decay of semiconductor QDs coupled to nearby metallic nanostructures [47, 48]). Our motivation is that, could the spontaneous emission spectrum from the strong coupling due to the surface plasmons be manipulated via the external coherent control?

In this work [101], we investigate the emission spectra of surface plasmon in a MNP with higher-order modes coupled to a QD with three-levels in lambda configuration. We show that the spontaneous decay of the transition coupled to the surface plasmons can be further modified by the coherent control on the adjacent transitions.

The chapter is organized as follows. In the next section, we present the theoretical model for the QD-MNP system. The spectral density (local density of photon states) and the derivations of the emission spectra in both weak- and strong- coupling regiems are rigorously provided. In Secs. 3.3 and 3.4, the detailed properties of the quantum light-matter interactions and the emission spectrum are discussed. In Sec. 3.5, we give a brief discussion about potential experimental configurations.

3.2 Theory

3.2.1 Model and the quantized surface plasmon

A schematic diagram for the present system is shown in Fig. (3.1). A hybrid system consists of a three-level lambda-type QD and a MNP. The QD is located at a distance h from the surface of a MNP, which is characterized by a radius R and permittivity $\epsilon_m(\omega)$. The center- to- center distance between the QD and MNP is taken as Z. The QD considered here has three discrete states designated $|\ell\rangle$ for $\ell \in \{1, 2, 3\}$ and the transition frequency $\omega_{\ell\ell'}$ corresponds to $|\ell\rangle \leftrightarrow |\ell'\rangle$. The levels $|3\rangle$ and $|1\rangle$ are the lower energy states, and the level $|2\rangle$ is the common op-

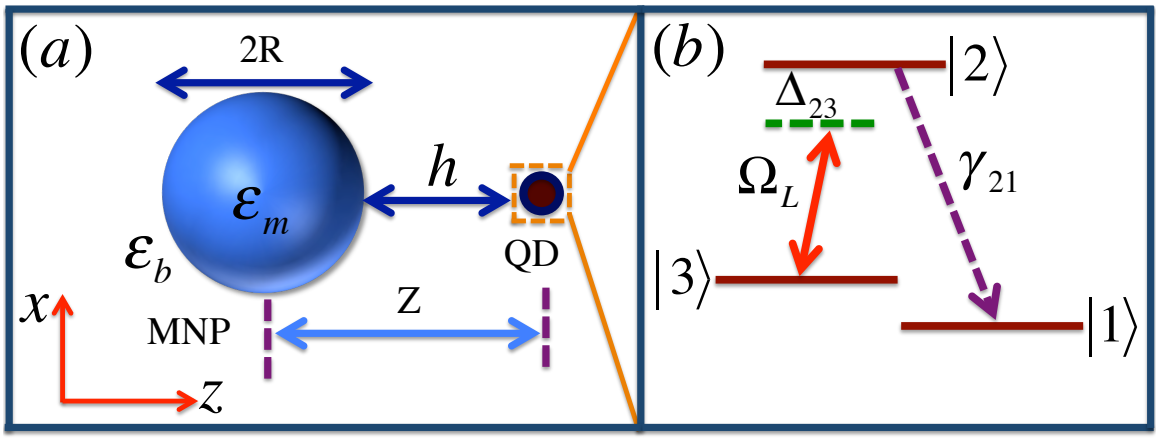

Figure 3.1: (a) A schematic diagram of the QD-MNP system embedded in a homogeneous background medium with permittivity ϵ_b. A QD located at h from the surface of a MNP which characterized by a radius R and permittivity ϵ_m. (b) The energy discrete states of the QD, where $|3\rangle$ and $|1\rangle$ are the lower-energy states, and the level $|2\rangle$ is the common optically excited state.

tically excited state. Here, the excitons of the QD are created by the transitions $|3\rangle \leftrightarrow |2\rangle$ and $|1\rangle \leftrightarrow |2\rangle$ with frequencies (dipole moments) ω_{23} (d_{23}) and ω_{21} (d_{21}), respectively. This discrete energy-level configuration has been recently achieved in semiconductor QDs and quantum optical effects such as electromagnetically induced transparency and coherent population trapping have been observed [102, 103, 104]. The transition$|3\rangle \leftrightarrow |2\rangle$ is resonantly driven by an external coherent field, Ω_L, while the transition $|2\rangle \leftrightarrow |1\rangle$ is nearly resonant to the plasmon mode of the MNP.

The fundamental mechanisms by which the radiative and nonradiative decay of particle plasmons occur in noble-metal nanoparticles is schematically shown in Fig. (3.2). Following light absorption and localized surface plasmon resonance excitation in these nanostructures, electromagnetic decay takes place either radiatively through re-emitted photons or non-radiatively by transferring the energy to hot

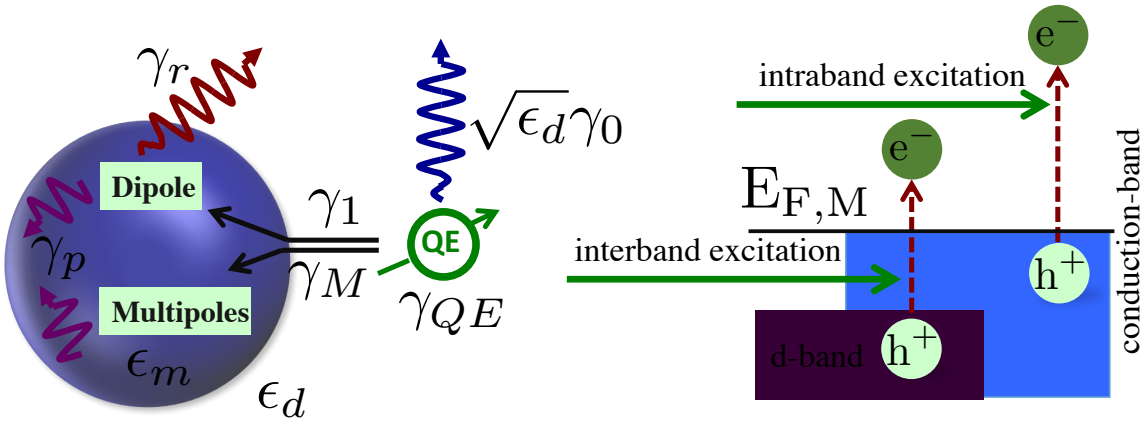

Figure 3.2: Schematic representation of localized surface plasmon decay: radiatively via re-emitted photons or non-radiatively via excitation of hot electrons. The non-radiative decay occurs through intraband excitations within the conduction band or through interband excitations resulting from transitions between other bands (for example, d bands) and the conduction band.

electrons (electron-hole excitations). Non-radiative decay can take place through intraband excitations within the conduction band or through interband excitations due to transitions between other bands (for example, d bands of nobel metals) and the conduction band. However, the d band energy levels respectively lie 2.4 eV and 4 eV below the Fermi energy levels for Au and Ag, which result in making the interband excitations considerably more unlikely than intraband excitations. The remaining photoexcited electrons relax through electron-electron and electron-phonon collisions, and are ultimately converted into heat. Fig. (3.3) shows the dielectric function of silver including size effect. Here, the frequency-dependent dielectric function of the metal-nanoparticle is given by $\epsilon_m(\omega) = \epsilon_{interband}(\omega) + \epsilon_{intraband}(\omega)$.

A microscopic consistent description of quantized radiation has been carried out for arbitrarily structured dielectrics [105] by integrating the semiclassical microscopic nonlocal theory developed by K. Cho [106]. Recently, plasmon-enhanced photocat-

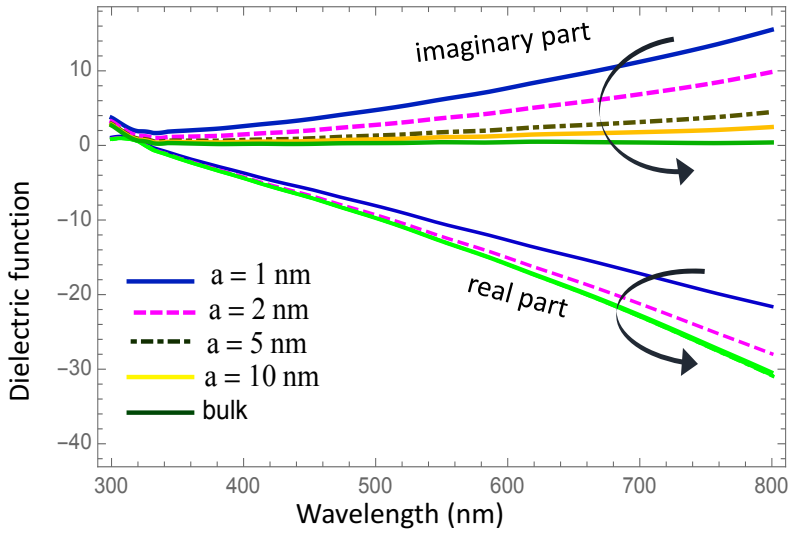

Figure 3.3: Dielectric function of silver nanoparticle including size effect.

alytic activity has been investigated experimentally in spirit of the interplay of a coupled nanocomposite system consisting of QD and MNP [107]. Also, the interplay and modification of the photoexcitation processes in a hybrid system composed of QD and MNP is treated self consistently [108] by applying the theory in Ref [106].

Our formulation is based on the quantization of the electromagnetic radiation in the presence of dispersive and absorbing media. Dispersion and absorption are related to each other by the Kramers-Kroning relations. The quantization is performed by means of a source-quantity representation based on the classical Green tensor. Here, the media are introduced as phenomenological noise currents that are associated with the electric and magnetic losses due to material absorption in Maxwell's equations, and the field operators are obtained indirectly from the noise operators via the classical Green's function [109]. By including the external driving field, the total Hamiltonian of the full system can be written as

$$\hat{H} = \sum_{i=1}^{3} \hbar\omega_i \hat{\sigma}_{ii} + \int d\boldsymbol{r} \int_0^\infty d\omega \hbar\omega \hat{\boldsymbol{f}}^\dagger(\boldsymbol{r},\omega) \cdot \hat{\boldsymbol{f}}(\boldsymbol{r},\omega)$$
$$- \left[\hat{\sigma}_{21} \int_0^\infty d\omega \boldsymbol{d}_{21} \cdot \hat{\boldsymbol{E}}(\boldsymbol{r}_d,\omega) + \text{H.c.}\right] + \left[\hbar\Omega_L e^{-i\omega_L t} \hat{\sigma}_{23} + \text{H.c.}\right], \tag{3.1}$$

where $\hat{\boldsymbol{f}}^\dagger(\boldsymbol{r},\omega)$ and $\hat{\boldsymbol{f}}(\boldsymbol{r},\omega)$ are the bosonic vector field operators for the elementary excitations of the system. The first term is the energy of a three-level system. The second term describes the total energy of the electromagnetic field. The third term is the interaction between the QD and the MNP under rotating wave approximation, where $\boldsymbol{d}_{21}$ is the transition dipole moment and $\hat{\sigma}$ is the coherence operator. The fourth term illustrates the interaction of the external driving field with the transition between $|3\rangle$ and $|2\rangle$. The Rabi field $\Omega_L = \boldsymbol{E}_L(\boldsymbol{r}_d) \cdot \boldsymbol{d}_{23}/\hbar\epsilon_{eff}$ is defined through the coherent external field $\boldsymbol{E}_L(\boldsymbol{r}_d)$ of frequency ω_L at the location of the QD ($\boldsymbol{r}_d$) and the transition dipole moment $\boldsymbol{d}_{23}$. The pump field at $\boldsymbol{r}_d$ contains the direct pumping term $\boldsymbol{E}_0(\boldsymbol{r}_d,\omega_L)$ plus the (dominant) scattered field contribution from the MNP where the spatial integration is carried out over the volume of the MNP

$$\boldsymbol{E}_L(\boldsymbol{r}_d,\omega_L) = \boldsymbol{E}_0(\boldsymbol{r}_d,\omega_L) + \int_{V_{\text{MNP}}} d\boldsymbol{r}' \boldsymbol{G}(\boldsymbol{r}_d,\boldsymbol{r}',\omega_L)$$
$$\times \left[\epsilon_{\text{MNP}}(\omega_L) - 1\right] \boldsymbol{E}_0(\boldsymbol{r}',\omega_L), \tag{3.2}$$

Here, $\epsilon_{eff} = (2\epsilon_b + \epsilon_s)/3\epsilon_b$ [110], with ϵ_b being the dielectric constant of the embedding medium and ϵ_s is the dielectric constant of the QD. The interaction with the QD is strong when the QD and MNP are in close proximity and their optical excitation frequencies are resonant with each other.

The electric field operator or the quantized emission field (source) in a system containing absorptive and dispersive media at the position of the QD is defined

through [109]

$$\hat{\boldsymbol{E}}(\boldsymbol{r}) = \hat{\boldsymbol{E}}^{(+)}(\boldsymbol{r}) + \hat{\boldsymbol{E}}^{(-)}(\boldsymbol{r}), \tag{3.3}$$

$$\hat{\boldsymbol{E}}^{(+)}(\boldsymbol{r}) = \int_0^\infty d\omega \hat{\boldsymbol{E}}(\boldsymbol{r},\omega), \quad \hat{\boldsymbol{E}}^{(-)}(\boldsymbol{r}) = \left[\hat{\boldsymbol{E}}^{(+)}(\boldsymbol{r})\right]^\dagger \tag{3.4}$$

$$\hat{\boldsymbol{E}}(\boldsymbol{r},\omega) = i\sqrt{\frac{\hbar}{\pi\epsilon_0}} \int d\boldsymbol{r}' \frac{\omega^2}{c^2} \sqrt{\epsilon_I(\boldsymbol{r}',\omega)} \boldsymbol{G}(\boldsymbol{r},\boldsymbol{r}',\omega) \cdot \hat{\boldsymbol{f}}(\boldsymbol{r}',\omega), \tag{3.5}$$

where $\epsilon_I(\boldsymbol{r}',\omega)$ is the imaginary part of the dielectric constant and $\boldsymbol{G}(\boldsymbol{r},\boldsymbol{r}',\omega)$ is the electric dyadic Green function. The dyadic Green's function for this geometry has two contributions,

$$\boldsymbol{G}(\boldsymbol{r},\boldsymbol{r}',\omega) = \boldsymbol{G}^0(\boldsymbol{r},\boldsymbol{r}',\omega) + \boldsymbol{G}^R(\boldsymbol{r},\boldsymbol{r}',\omega), \tag{3.6}$$

where $\boldsymbol{G}^0(\boldsymbol{r},\boldsymbol{r}',\omega)$ is the direct contribution from the radiation sources in an unbounded medium or free space solution and $\boldsymbol{G}^R(\boldsymbol{r},\boldsymbol{r}',\omega)$ is the reflection contribution coming from the interaction of the dipole with the materials.

3.2.2 Spectral density and photon Green function

The action of the dissipative medium on the QD in the system depicted in Fig. (3.1) is described completely by the spectral density

$$\kappa(\omega) = \frac{1}{\pi\epsilon_0} \boldsymbol{d}_{21} \cdot \left[\frac{\omega^2}{c^2} \mathrm{Im}[\boldsymbol{G}(\boldsymbol{r}_d,\boldsymbol{r}_d,\omega)]\right] \cdot \boldsymbol{d}_{21}, \tag{3.7}$$

which is related with the QD-MNP coupling $g(\omega)$ and the local density of states (LDOS) of the MNP $\rho(\omega)$ by means of $\kappa(\omega) = g^2(\omega)\rho(\omega)$. In this case, all the matter parameters that are relevant to the QD dynamics are contained in the Green function.

The classical photonic Green function in the dissipative medium characterized by a complex dielectric function $\epsilon_m(\boldsymbol{r},\omega) = \epsilon_R(\boldsymbol{r},\omega) + i\epsilon_I(\boldsymbol{r},\omega)$ with $\mu = 1$ satisfies the following equation

$$\left[\nabla \times \nabla \times -\frac{\omega^2}{c^2}\epsilon_m(\boldsymbol{r},\omega)\right] \boldsymbol{G}(\boldsymbol{r},\boldsymbol{r}',\omega) = \boldsymbol{I}\boldsymbol{\delta}(\boldsymbol{r}-\boldsymbol{r}'), \tag{3.8}$$

where $\boldsymbol{I}$ is the unit dyadic. The dyadic Green function is constructed from the expansion of the spherical vector wave function with the boundary conditions at the spherical interface satisfying. The details are provided in Appendix B. For the interesting problem of the MNP, we will discuss the Green function within and beyond the dipole approximation.

In the case of small MNPs ($ka \ll 1$) of permittivity $\epsilon_m(\omega)$, embedded in a material with permittivity ϵ_b, the particle can be modelled as an electric dipole. In this case, the Green function described in the dipole approximation can be written as [111]

$$\begin{aligned}\boldsymbol{G}(\boldsymbol{r},\boldsymbol{r}',\omega) =& \boldsymbol{G}^0(\boldsymbol{r},\boldsymbol{r}',\omega) \\ &+ \frac{k^2}{\epsilon_0}\boldsymbol{G}^0(\boldsymbol{r},\boldsymbol{r}_m,\omega)\cdot\alpha_m(\omega)\boldsymbol{G}^0(\boldsymbol{r}_m,\boldsymbol{r}',\omega),\end{aligned} \tag{3.9}$$

where $\boldsymbol{G}^0$ is the free-space Green function, $\alpha_m(\omega)$ is the polarizability of the spherical MNP, and $\boldsymbol{r}_m$ is the position of the MNP. The second term in Eq. (3.9) describes the modification of the free-space Green function due to the presence of the MNP. The polarizability is given by [112, 113]

$$\alpha_m(\omega) = \alpha_m^0(\omega)\left[1 - i(k^3/6\pi\epsilon_0)\alpha_m^0(\omega)\right]^{-1}, \tag{3.10}$$

where $\alpha_m^0(\omega)$ is the quasi-static polarizability defined by

$$\alpha_m^0(\omega) = 4\pi\epsilon_b a^3 \frac{(\epsilon_m(\omega)-\epsilon_b)}{[\epsilon_m(\omega)+2\epsilon_b]}. \tag{3.11}$$

The second term in the denominator in Eq. (3.10) accounts for the radiation reaction and originates from the action of the MNP on itself.

To account for the finite-size effect of the MNP we also compute the Green function beyond the dipole approximation. The generalized Drude model is employed for the dielectric function of the MNP,

$$\epsilon_m(\omega) = \epsilon_\infty - \frac{\omega_p^2}{\omega^2 + i\gamma_e\omega}, \tag{3.12}$$

where ϵ_∞ is the high-frequency limit of the metal dielectric function which account for the contribution due to the interband transitions; it is unity for the case of a perfectly free-electron gas, ω_p is the bulk plasmon frequency, and γ_e is the Landau damping constant.

We consider a spherical silver MNP with typical parameters: $\epsilon_\infty = 6$, $\hbar\omega_p = 7.90eV$, and $\hbar\gamma_e = 51meV$, which provide a reasonably good fit to tabulated experimental data for photon energies smaller than $3eV$ [114].

Without lack of generality, we assume the dipole to be oriented along the z axis. In Figs. (3.4a) and (3.4b), we plot the z-projected local density of states (LDOS), $\rho_{zz} = \mathrm{Im}[\boldsymbol{G}_{zz}(\boldsymbol{r}_d, \boldsymbol{r}_d, \omega)]$ in units of ρ_0, where, $\rho_0 = \mathrm{Im}[\boldsymbol{G}^0_{zz}(\omega)] = k/6\pi$ for a silver MNP with radius 8 nm and 20 nm, respectively. Here, $\boldsymbol{G}^0(\omega)$ is the free-space Green function given in Appendix C. The detail derivations of these expressions are given in Appendix C.

For a small separation, $h = 2\ nm$, the QD exciton is strongly coupled to the MNP. From Fig. (3.4a), it is readily seen that the LDOS (blue, upper line) at higher-order plasmon mode is several times larger than that of the dipole mode peak. For larger separations between the QD and the surface of the MNP (when the dipole moves away from the MNP) the dipole-dipole interaction and correspondingly the strong

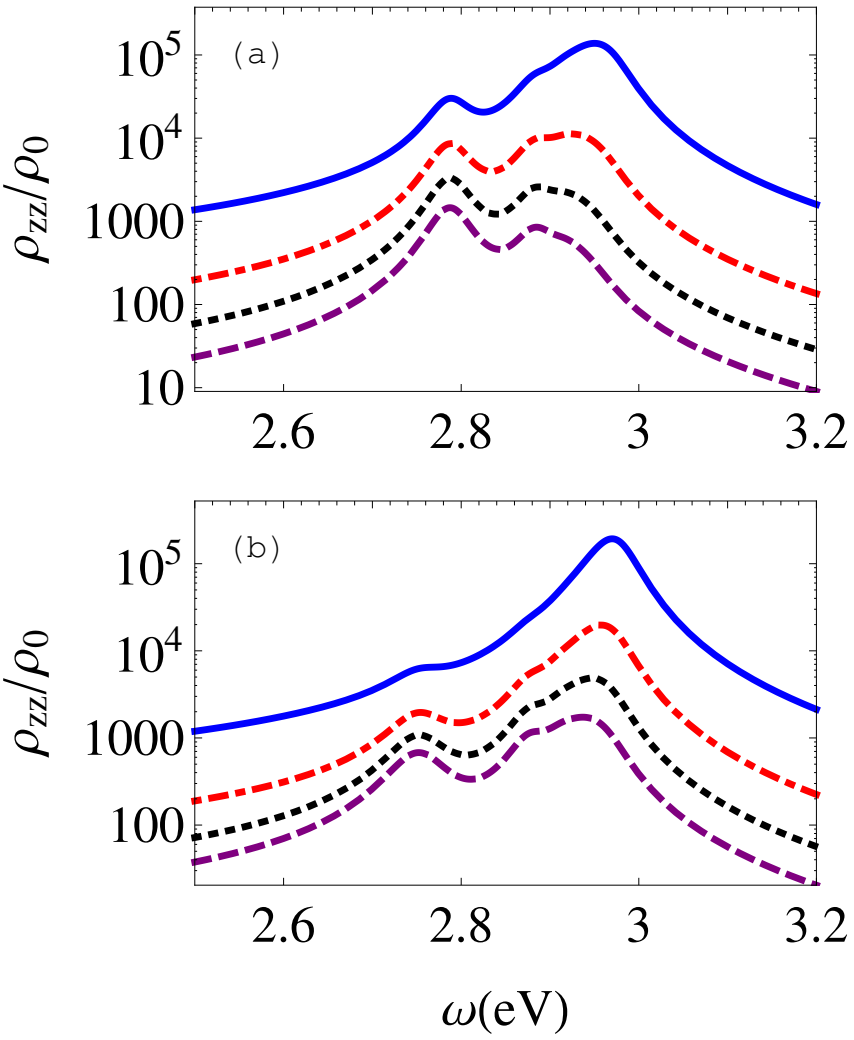

Figure 3.4: (a) Dependence of the LDOS ρ_{zz} in units of ρ_0 as a function of frequency ω for different separations: $h = 2$ nm (blue, upper curve), 4 nm (red, dashed-dotted curve), 6 nm (black, dotted curve), and 8 nm (purple, lower curve), near a MNP with $R = 8$ nm. (b) The same as (a) but with $R = 20$ nm.

coupling regime is hardly resolvable. Therefore, for a small MNP, the high-order surface plasmon mode has a dominant contribution to the spectrum at small QD-MNP separation. However, when the dipole moves away from the MNP, only the lowest mode is contributed.

Fig. (3.4b) shows the LDOS with a larger MNP with $R = 20$ nm. For a small

separation between the QD and MNP ($h = 2\ nm$), the contribution of the higher-order plasmon mode to the dipole-dipole interaction increases dramatically. In this situation, the contribution from the dipole mode is approximately negligible. Interestingly, even for larger h (up to 8 nm), the higher-order plasmon mode is still dominant and it is several times larger than that of the dipole mode peak. This difference between the two cases has a simple physical interpretation. The radiation reflected back from the MNP towards the dipole is proportional to the size of the MNP. It is worth noting that as the radius of the MNP increases the interval between the fundamental dipole peak and higher-order modes increases correspondingly. In the large sphere limit ($R \to \infty$), the theory of the dipole near a planer surface becomes applicable.

The localized surface plasmon resonance corresponds to the left peak on the curves in Fig. 3.4. It can be obtained analytically from the frequency-dependent complex coefficient $\alpha_m^0(\omega)$, see Eq. (3.11). However, the plasmon resonance can be obtained beyond the nonretarded approximation from the explicit form of the reflection coefficients (see Appendix B) by noting that the coefficients R^H and R^V derived in Eqs. (B.49a)- (B.49h) contain poles at the points where the denominator vanishes. These poles correspond to the excitations of surface plasmon modes of the system which show the explicit dependence on the radius R of the MNP. We note that the frequencies of the peaks in Fig. 3.4 do not coincide with that calculated from Eq. (3.11) but are slightly shift towards the low frequency side. This is because the frequencies obtained from Eq. (3.11) are those for the $R \to 0$ limit.

3.3 Populations and spontaneous emission spectrum

In this subsection, we derive the equations of motion for the populations and the light intensity spectrum for the three-level Lambda-type QD located in the vicinity

of the MNP as depicted in Fig. 3.1. The wave function of the system can be written in the form

$$\begin{aligned}|\psi(t)\rangle =& C_2(t)e^{-i\omega_2 t}\,|2\rangle\,|\{0\}\rangle + C_3(t)e^{-i\omega_3 t}\,|3\rangle\,|\{0\}\rangle \\ &+ \int d\boldsymbol{r}\int_0^\infty d\omega C_1(\boldsymbol{r},\omega,t)e^{-i(\omega+\omega_1)t}\,|1\rangle\,|\mathbf{1}(\boldsymbol{r},\omega)\rangle\,,\end{aligned} \tag{3.13}$$

where $|\mathbf{1}(\boldsymbol{r},\omega)\rangle = \hat{\boldsymbol{f}}^\dagger(\boldsymbol{r},\omega)\,|\{0\}\rangle$. Here, C_ℓ for $\ell \in \{1,2,3\}$ is the excitation amplitude of state $|\ell\rangle$ and $|\ell\rangle\,|\{0\}\rangle$ indicates QD in state $|\ell\rangle$ and no plasmon.

Using the time-dependent Schrödinger equation, the differential equations for the probability amplitudes are given by:

$$\dot{C}_2(t) = \int_0^t dt' K(t-t')C_2(t') - i\Omega_L e^{-i(\omega_L-\omega_{23})t}C_3(t), \tag{3.14a}$$

$$\dot{C}_3(t) = -i\Omega_L e^{i(\omega_L-\omega_{23})t}C_2(t), \tag{3.14b}$$

$$\dot{C}_1(\boldsymbol{r},\omega,t) = \frac{1}{\sqrt{\hbar\pi\epsilon_0}}\frac{\omega^2}{c^2}\sqrt{\epsilon_I(\boldsymbol{r},\omega)}\boldsymbol{d}_{21}^*\cdot\boldsymbol{G}^*(\boldsymbol{r}_d,\boldsymbol{r},\omega)e^{i(\omega-\omega_{21})t}C_2(t), \tag{3.14c}$$

where we used Eq. (3.1). Here, the kernel function

$$\begin{aligned}K(t-t') =& -\frac{1}{\hbar\pi\epsilon_0}\int_0^\infty d\omega\frac{\omega^2}{c^2}e^{-i(\omega-\omega_{21})(t-t')} \\ &\times \boldsymbol{d}_{21}\cdot\mathrm{Im}[\boldsymbol{G}(\boldsymbol{r}_d,\boldsymbol{r}_d,\omega)]\cdot\boldsymbol{d}_{21},\end{aligned} \tag{3.15}$$

in which we have used the relationship [109]

$$\int d\boldsymbol{s}\frac{\omega^2}{c^2}\epsilon_I(\boldsymbol{s},\omega)\boldsymbol{G}(\boldsymbol{r},\boldsymbol{s},\omega)\boldsymbol{G}^*(\boldsymbol{s},\boldsymbol{r}',\omega) = \mathrm{Im}[\boldsymbol{G}(\boldsymbol{r},\boldsymbol{r}',\omega)], \tag{3.16}$$

One way of solving Eqs. (3.14) is to calculate the dispersion relations over the whole spectra of n, where n indicates the mode as defined by the Green function in Appendix B. Consequently, $C_2(t)$ can be obtained by performing a numerical inverse Laplace transformation. An alternative way to solve Eqs. (3.14) is by first taking the time integral of both sides of Eq. (3.14a). This integral equation is a well-known Volterra integral equation of the second kind [115]. We have adopted the second approach, although, both these methods are equivalent.

The emitted light spectrum $S(\boldsymbol{r},\omega)$ registered at a point $\boldsymbol{r}$ sufficiently away from the source can be defined as [116, 117]

$$S(\boldsymbol{r},\omega) = \frac{1}{2\pi}\int_0^\infty dt_2 \int_0^\infty dt_1 e^{-i\omega(t_2-t_1)} \left\langle \hat{\boldsymbol{E}}^{(-)}(\boldsymbol{r},t_2)\cdot\hat{\boldsymbol{E}}^{(+)}(\boldsymbol{r},t_1)\right\rangle . \tag{3.17}$$

Using Eqs. (3.3), (3.5), and (3.13) we get

$$\begin{aligned}\hat{\boldsymbol{E}}^{(+)}(\boldsymbol{r})\left|\psi(t_1)\right\rangle =& i\sqrt{\frac{\hbar}{\pi\epsilon_0}}\int_0^\infty d\omega' \frac{\omega'^2}{c^2}\int d\boldsymbol{r}'\sqrt{\epsilon_I(\boldsymbol{r}',\omega')} \\ & \times \boldsymbol{G}(\boldsymbol{r},\boldsymbol{r}',\omega')C_1(\boldsymbol{r}',\omega',t_1)e^{-i\omega' t}\left|1\right\rangle\left|\{0\}\right\rangle . \end{aligned}\tag{3.18}$$

Formal integration of Eq. (3.14c) and substitution of Eq. (3.18) into Eq. (3.17) leads to, upon using relation (3.16),

$$\begin{aligned} & S(\boldsymbol{r},\omega) \\ & \quad = \frac{1}{2\pi}\left|\int_0^\infty dt e^{-i(\omega_{21}-\omega)t}\int_0^t dt' C_2(t') \right. \\ & \qquad \left. \times \int_0^\infty d\omega' \frac{\omega'^2}{\pi\epsilon_0 c^2}\boldsymbol{d}_{21}\cdot \mathrm{Im}[\boldsymbol{G}(\boldsymbol{r},\boldsymbol{r}_d,\omega')]e^{-i(\omega'-\omega_{21})(t-t')}\right|^2 . \end{aligned}\tag{3.19}$$

Note that Eq. (3.19) can be equivalently rewritten as

$$S(\boldsymbol{r},\omega) = \frac{1}{2\pi}\left|\int_0^\infty dt e^{-i(\omega_{21}-\omega)t}\int_0^t dt' C_2(t')\bar{K}(t-t')\right|^2. \tag{3.20}$$

with

$$\bar{K}(t-t') = \int_0^\infty d\omega' \frac{\omega'^2}{\pi\epsilon_0 c^2}\boldsymbol{d}_{21}\cdot \mathrm{Im}[\boldsymbol{G}(\boldsymbol{r},\boldsymbol{r}_d,\omega')]e^{-i(\omega'-\omega_{21})(t-t')}. \tag{3.21}$$

The term in the absolute square of Eq. (3.20) is equivalent to the Laplace transform, calculated at the point $i(\omega_{21}-\omega)$, of the Laplace convolution of the two functions. Then,

$$S(\boldsymbol{r},\omega) = \frac{1}{2\pi}\left|\mathcal{L}\int_0^t dt' C_2(t')\bar{K}(t-t')\right|^2. \tag{3.22}$$

The function, $\mathcal{L}[C_2(t)]$, is the Laplace transform of $C_2(t)$ at the point $i(\omega_{21}-\omega)$, which describes the spectrum at the QD location. The expression of $\mathcal{L}[C_2(t)]$ can be derived from the differential equations of the coefficients, Eqs. (3.14), as

$$\mathcal{L}[C_2(t)] = \frac{C_{20}[s+i\triangle_{23}] - i\Omega_L C_{30}}{[s+i\triangle_{23}]\left[s-\mathcal{L}[K]+\frac{|\Omega_L|^2}{[s+i\triangle_{23}]}\right]}, \tag{3.23}$$

where C_{20} and C_{30} are the initial states of the amplitudes and $\mathcal{L}[K]$ is the Laplace transform of the kernel function defined in Eq. (3.15), and it is given by

$$\begin{aligned}\mathcal{L}[K] = &-\frac{1}{\hbar\pi\epsilon_0}\int_0^\infty d\omega' \frac{\omega'^2}{c^2}\boldsymbol{d}_{21}\cdot\mathrm{Im}[\boldsymbol{G}(\boldsymbol{r}_d,\boldsymbol{r}_d,\omega')]\cdot\boldsymbol{d}_{21}\\ &\times\frac{1}{[s+i(\omega'-\omega_{21})]}.\end{aligned} \tag{3.24}$$

$\Delta_{23} = \omega_{23}-\omega_L$ is the detuning of the coherent field of frequency ω_L from the transition frequency between states $|2\rangle$ and $|3\rangle$.

The second term, $\mathcal{L}[\bar{K}(\tau)]$, accounts for the photon propagation from the QD to a detector. Thus can be calculated from Eq. (3.21) as

$$\mathcal{L}[\bar{K}][i(\omega_{21}-\omega)] = \int_0^\infty d\tau \int_0^\infty d\omega' \frac{\omega'^2}{\pi\epsilon_0 c^2}$$

$$\times \boldsymbol{d}_{21}\cdot \mathrm{Im}[\boldsymbol{G}(\boldsymbol{r},\boldsymbol{r}_d,\omega')]e^{-i(\omega'-\omega)\tau} \tag{3.25a}$$

$$= -\, i\frac{\omega^2}{\epsilon_0 c^2}\boldsymbol{d}_{21}\cdot\boldsymbol{G}(\boldsymbol{r},\boldsymbol{r}_d,\omega). \tag{3.25b}$$

in which we have used the relation $\frac{i}{\omega'-\omega+i\epsilon} = \pi\delta(\omega'-\omega)+iP(\frac{1}{\omega'-\omega})$, with P the principle value. Finally, the exact expression of the emitted spectrum is given explicitly by

$$S(\boldsymbol{r},\omega)$$
$$= \frac{1}{2\pi}\left|\frac{\left[C_{20}\left(\omega_{21}-\omega+\Delta_{23}\right)-\Omega_L C_{30}\right]\left(\omega+\omega_{21}\right)\omega^2}{\left(\omega_{21}-\omega+\Delta_{23}\right)\epsilon_0 c^2}\right.$$
$$\left.\times \frac{\boldsymbol{d}_{21}\cdot\boldsymbol{G}(\boldsymbol{r},\boldsymbol{r}_d,\omega)}{\left\{\omega_{21}^2-\omega^2-i\omega\gamma_d-2\omega_{21}\frac{1}{\hbar\pi\epsilon_0}\int_0^\infty d\omega'\frac{\omega'^2}{c^2}\boldsymbol{d}_{21}\cdot\mathrm{Im}[\boldsymbol{G}(\boldsymbol{r}_d,\boldsymbol{r}_d,\omega')]\cdot\boldsymbol{d}_{21}\frac{1}{(\omega'-\omega)}-\frac{(\omega+\omega_{21})|\Omega_L|^2}{[\omega_{21}-\omega+\triangle_{23}]}\right\}}\right|^2. \tag{3.26}$$

The emission spectra is dependent on the initial state of the QD and is mainly affected by both the driving field Ω_L and the coupling between the QD and the MNP. By adjusting the intensity of the external control field and the separation distances between the QD and the MNP, the spectral properties can be modified. We highlight that the above equation is derived rigorously with no Markov approximation so it can be applied to both weak- and strong -coupling regimes. It should be emphasized that Eq. (3.26) can be used to calculate the emitted light spectrum for more complicated

configurations whenever the corresponding Green functions are known. It shows precisely the features of the non-Markovian spectra and the propagation effects to the detector.

3.4 Results

In this section, we illustrate and discuss the results for the quantum light-matter interactions and the emission spectra based on our expression (3.26) under different initial conditions and different strengths of the control field. Here, we mainly focus on two different schemes: first, we investigate the spectrum of a QD exciton initially in the excited state, where the external control field is turned off. Second, the spectrum of a QD with three-level in Lambda configuration initially in its ground state and driven by means of a coherent laser field. The later scheme shows a great degree of coherent control over the field interaction. We show that the emission spectra can be controlled by adjusting the control field along with the separation distances from the MNP.

3.4.1 The spectrum with $\Omega_L = 0$

First, we investigate spontaneous emission spectrum in the absence of the control field, i.e., $\Omega_L = 0$, when the QD is initially in the excited state. For all numerical calculations, we consider a dipole emitter with a dipole moment $d_{21} = 0.5\ e\ nm$, which is comparable to the dipole moments used in other works that model QDs coupling to metals [118]. We also use $\gamma_d = 15\ meV$, which corresponds to the decay of a typical QD exciton, for example, the $PbSe$ colloidal QDs at room temperature [119].

The characteristic of the strong-coupling regime of the QD-MNP system in the spectral domain is shown in Fig. (3.5). A consequence of the strong coupling regime, there is a vacuum Rabi splitting when the transition frequency of the QD exciton

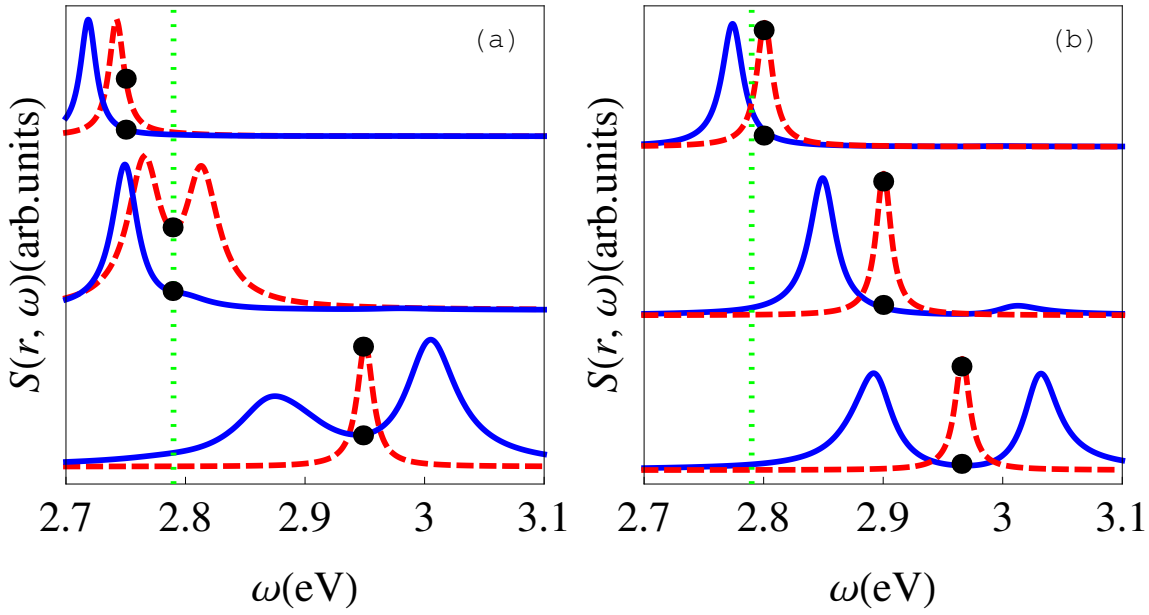

Figure 3.5: The spontaneous emission spectra (a) for a silver nanosphere with $R = 8$ nm and $h = 2$ nm; (b) for a silver nanosphere with $R = 20$ nm and $h = 2$ nm. The red-dashed curves correspond for the results of the dipole approximation, and the blue-solid curves correspond for the results including the contributions from the higher-order of the plasmonic modes. Each curve is normalized independently of the others. The location of the QD transition frequencies are indicated by superimposed black dots on the curves. The vertical green-dotted lines in these graphs characterize the localized surface plasmon resonance [i.e., the maximum of the frequency-dependent complex coefficient $\alpha_m(\omega)$].

is at resonance with the surface plasmon. In Fig. (3.5a), we show the spectrum with $R = 8$ nm and $h = 2$ nm. The dashed curves are calculated using the dipole approximation, while the solid curves include the contributions from higher-order plasmonic mode. The location of the QD transition frequency is indicated by black dots on the curves. The vertical green dotted lines in these graphs characterize the localized surface plasmon resonance which depends on the radius of the MNP beyond the quasi-static approximation. Interestingly, when the QD exciton transition frequency is resonant with the localized surface plasmon resonance ($\omega \simeq 2.79eV$), there is a clear peak-splitting effect which confirmed the strong coupling regime

in this system as shown by the red-dashed curve in Fig. (3.5a). In addition, the predicted Lamb shifts are perceptible in the spectra as the exciton spectral peaks are substantially shifted in energy. These results are somewhat different from that in Ref. [98], where the authors assumed that, generally, the dipole result shows no indication of strong coupling. However, we have found that when the QD exciton transition frequency is resonant with the localized surface plasmon and the radius of the MNP is typically small ($R = 8\ nm$ in Fig. (3.5a), the clear evidence of the strong coupling regime of the system can be readily observed. Higher-order plasmon mode also demonstrated the vacuum Rabi splitting in the spectra with $R = 8\ nm$. However, as shown by the blue-solid curve in Fig. (3.5b), the splitting between the peaks in the spectrum are notably larger for the case of $R = 20\ nm$ due to the dominant contribution from the higher-order plasmon modes near $\omega \simeq 2.968eV$.

We have numerically solved the time-dependent dynamical equations (3.14) to demonstrate the decay evaluations of the QD exciton, assuming that initially there is an exciton in the QD and no plasmon excitation. The results are shown in Fig. (3.6) with $h = 2\ nm$. The purple dashed-dotted and blue solid lines represent the non-Markovian dynamics of the QD exciton for $R = 8\ nm$ and $R = 20\ nm$, respectively, including the contributions from the higher-order plasmonic mode of the system (the nondipole results). The red dashed curve shows the dynamics of the QD exciton with $R = 8\ nm$ using the dipole approximation. It is worth noting the existence of the oscillating behavior in the decay profile, demonstrating the decay dynamics for small h contains the non-Markovian features. The oscillatory behavior in Fig. (3.6) shows the strong coupling between the QD and MNP, and it is a direct consequence of strong interaction between the QD and its own localized radiation. The oscillating dynamics of the QD is more pronounced in the case of $R = 8\ nm$ with the contribution from high-order surface plasmon modes since the LDOS is very large

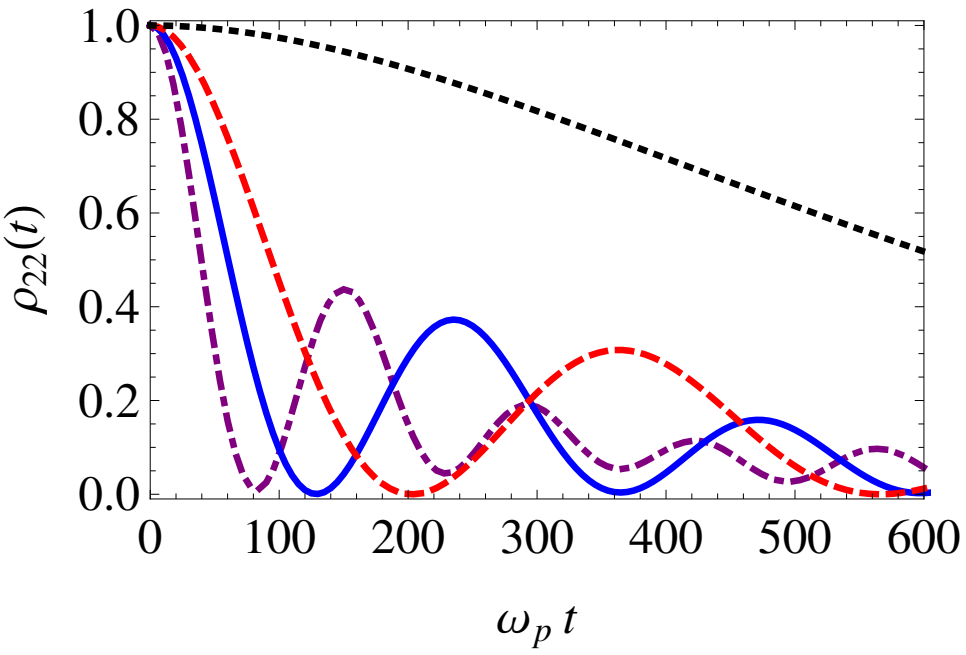

Figure 3.6: Evaluation of the non-Markovian decay dynamics of the QD exciton, $\rho_{22}(t) = |C_2(t)|^2$, with $h = 2\ nm$. The dashed-dotted curve and the solid curve represent the nondipole (exact) results with $R = 8\ nm$ and $R = 20\ nm$, respectively. The dashed curve shows the dynamics of the QD with $R = 8\ nm$ under the dipole approximation. The transition frequency of the QD exciton used in these curves is taken corresponding to the peaks of the LDOS (*i.e.*, $\omega_{21} \approx \omega_{sp}$). The black, dotted line shows the dynamics of the QD exciton at $h = 10\ nm$ away from the surface of the MNP.

in this case. These results agree very well with the elaborate experiment reported in Ref. [107]. The results in Fig. (3.6) are in good agreement with the results in Fig. (3.5). Finally, for $h > 10\ nm$, the strong coupling regime is diminished and the spontaneous decay state becomes almost exponential as shown by the black dotted line in Fig. (3.6).

3.4.2 The spectrum with $\Omega_L \neq 0$

In this subsection, we calculate the spontaneous emission spectrum for the Λ system shown in Fig. (3.1) using Eq. (3.26). The QD is initially in its ground state

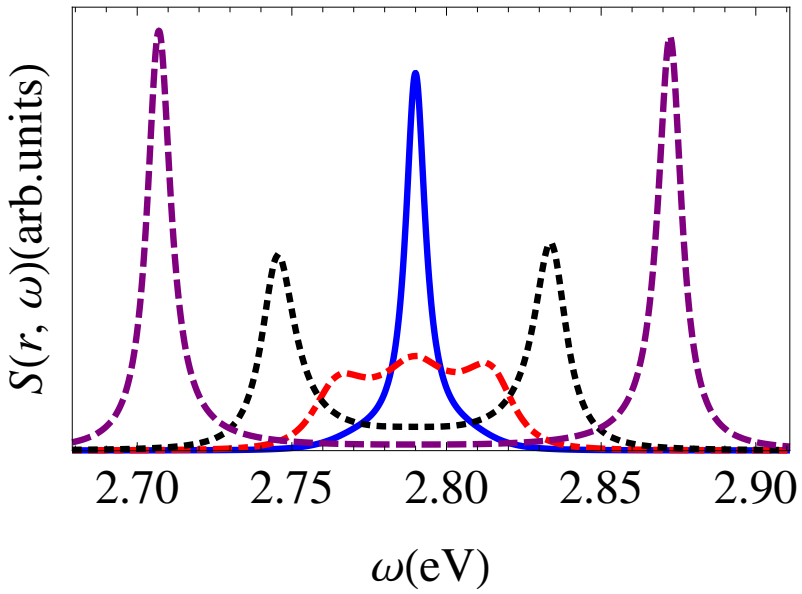

Figure 3.7: Calculated spectra of the QD located at $h = 2\ nm$ with $R = 8\ nm$ and $\Delta_{23} = 0$ for different Rabi fields: $\Omega_L = 10$ (solid curve), 20 (dashed-dotted curve), 40 (dotted curve), and 60 meV (dashed curve) using the dipole approximation.

$|3\rangle$ and driven externally by the coherent laser field to state $|2\rangle$. The transition $|2\rangle \leftrightarrow |1\rangle$ is nearly resonant with the plasmon mode of the metallic nanostructure, which leads to the energy transfer from the dipole to surface plasmons. The local fields of surface plasmons in turn provide feedback by stimulating $|2\rangle \rightarrow |1\rangle$ transition. It is worth noting that the coherent driving field is applied at a different frequency from that of the transition $|2\rangle \rightarrow |1\rangle$, and it is not resonant with the surface plasmon modes. Our interest is to coherently control the strong interaction in the QD-MNP system due to surface plasmon modes.

In Fig. (3.7), we show the spectra for the QD located close from the surface of the MNP ($h = 2\ nm$) with different Rabi field intensities using the dipole approximation. First, when the Rabi field is weak, $\Omega_L = 10meV$ (blue, solid curve), the light emitted will be absorbed by the MNP via nonradiative transfer energy from the dipole emitter to the surface plasmon. We observe a Lorentzian-type spectrum

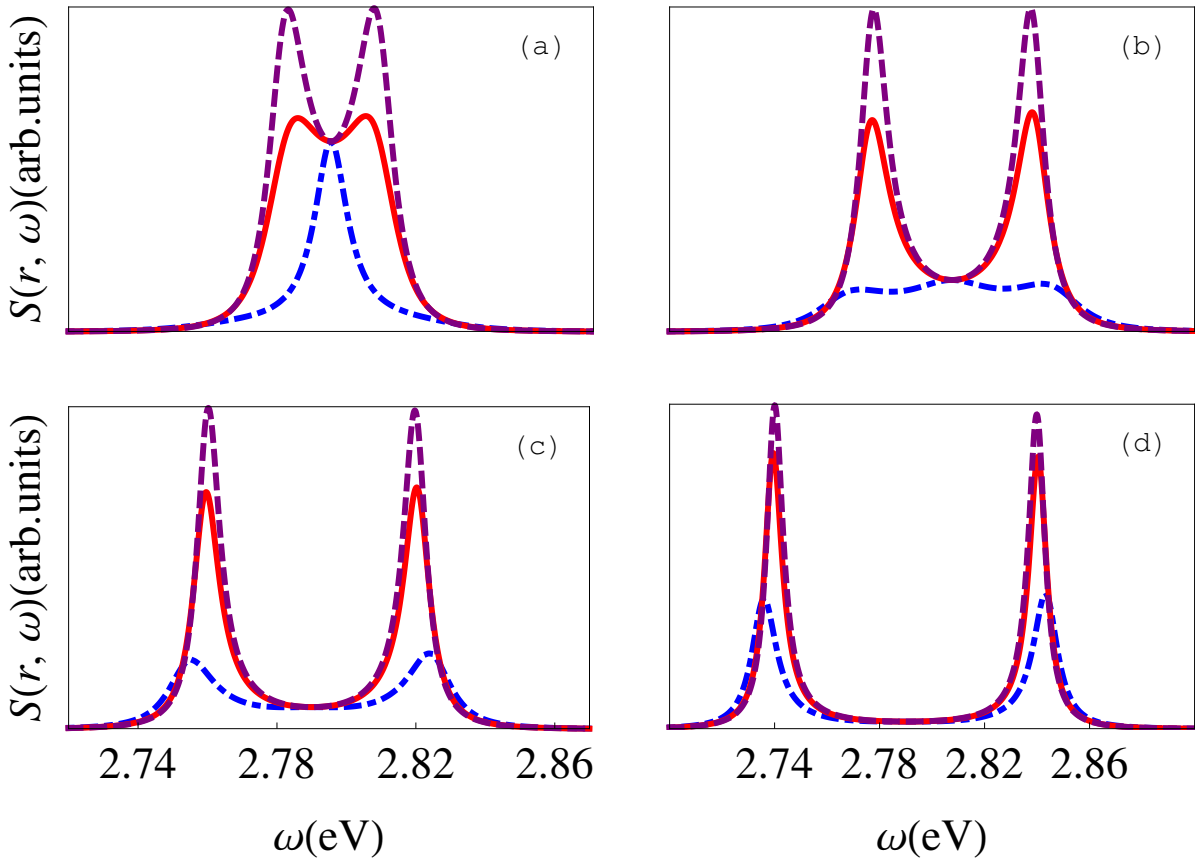

Figure 3.8: The dependence of the spontaneous emission spectra for the QD located at different distances from the surface of the MNP, $h = 2\ nm$ (blue, dashed-dotted curve), $5\ nm$ (red, solid curve), and $8\ nm$ (purple, dashed curve) with different Rabi fields: $(a)\ \Omega_L = 10meV$, $(b)\ \Omega_L = 20meV$, $(c)\ \Omega_L = 30meV$, and $(d)\ \Omega_L = 50meV$. Here, $\Delta_{23} = 0$ and $R = 8\ nm$

at the dipole transition frequency. This behavior can be readily explained from the dynamics of the QD exciton. We have found that by solving the time-dependent Schrödinger equation in non-Markovian way there is no oscillation in the dynamics decay of the QD exciton, $|C_2(t)|^2$. Nonetheless, when the MNP moves far from the QD, the Lorentzian peak at $\Omega_L = 10meV$ will split into two peaks. The splitting depends on the intensity of the control field.

In Fig. (3.7), we show that by fixing the distance between the QD and the MNP,

$h = 2\ nm$, as the intensity of the control field increases, the manifestation of the oscillations and consequently the splitting of the spontaneous emission spectrum is clearly observed (see dotted and dashed lines, respectively).

The behavior of the spectra in Fig. (3.7) can be straightforwardly explained by Fig. (3.8), which shows the dependence of the spontaneous spectra on the coherent laser field (Ω_L) along with the separation distances from the surface of the MNP (h). When the MNP enters the subwavelength distance range, the total (radiative and nonradiative) decay rates of the emitter are significantly enhanced compared to that in the free-space (Purcell effect). The total decay rates are predominantly nonradiative due to Förster energy transform. This effect, responsible for fluorescence quenching [120, 121], corresponds to the absorption of the emitted photons by metallic structures itself. In Fig. (3.8a), we show the spectra with a typically weak control field, $\Omega_L = 10meV$. The curves correspond to different QD locations: $h = 2$ nm (blue, dashed-dotted curve), 5 nm (red, solid curve), and 8 nm (purple, dashed curve). The effects of the MNP can be tailored by moving the QD further away from its surface as shown with the dashed line. In Fig. (3.8b-3.8d), we show how the spectra for the QD can be manipulated by adjusting the intensity of the coherent field. In Fig. (3.8d), we show a clear evidence of large splitting for the state $|2\rangle$ when the coherent field is $\Omega_L = 50meV$, although the QD is in the vicinity of the MNP.

The Green function entering into Eq. (3.26) can be understood in terms of the contributions from the fundamental plasmon dipole mode (usually referred as a localized surface plasmon mode of the nanosphere) and a reservoir of higher-order plasmon modes. In the strong coupling regime, the energy is highly concentrated in the higher-order plasmon modes which are mainly coupled into the near field and are responsible for the optical enhancement. However, the dipole mode propagates and does couple to the far field. The near-field excitation of higher-order multipoles

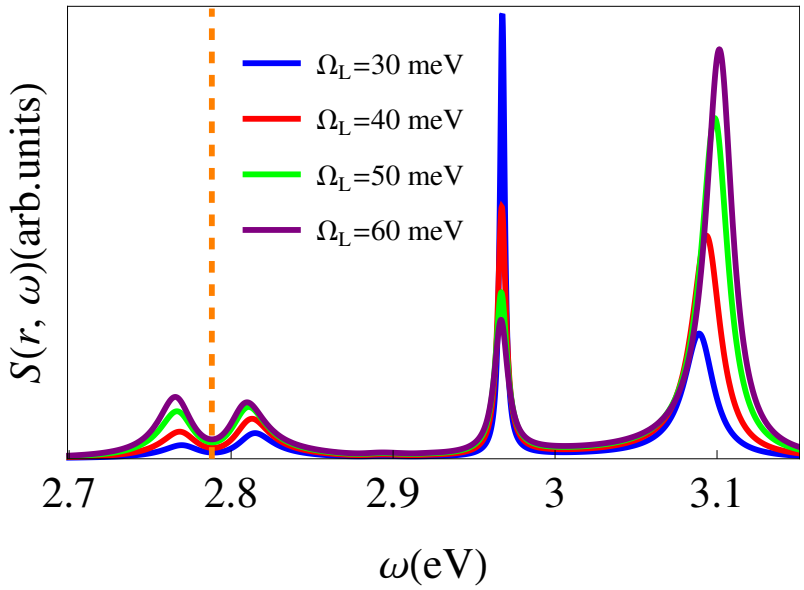

Figure 3.9: Calculated spectra for the QD located at $h = 2\ nm$ with $R = 8\ nm$ and $\Delta_{23} = 0$. Here we calculate the spectra by including the contributions from all the higher-order plasmonic modes of the system with increasing Rabi fields, for $\Omega_L = 30$ (blue curve), 40 (red curve), 50 (green curve), and 60 meV (purple curve). The vertical orange line indicates the localized surface plasmon resonance [at the maximum of $\alpha_m(\omega)$].

extract the energy out of the emitter in a nonradiative fashion. These features are demonstrated in Fig. (3.9) with the presence of the control field, Ω_L. In Fig. (3.9), we calculate the emission spectra for the QD located at $h = 2\ nm$ with $R = 8$ nm by including the contributions of higher-order plasmon modes. The transition frequency of the QD is chosen as $\omega_{21} = 2.968eV$ corresponding to the larger LDOS in Fig. (3.6). We observed peaks due to the reservoir near field at the QD transition frequency but dips or dark regions at the center of the localized surface plasmon resonance.

Physically, with the small volume of the MNP and the small separation between the QD and the MNP, the LDOS is very large and the coupling to higher-order plasmon modes is dominated by means of a high nonradiative decay rate of the

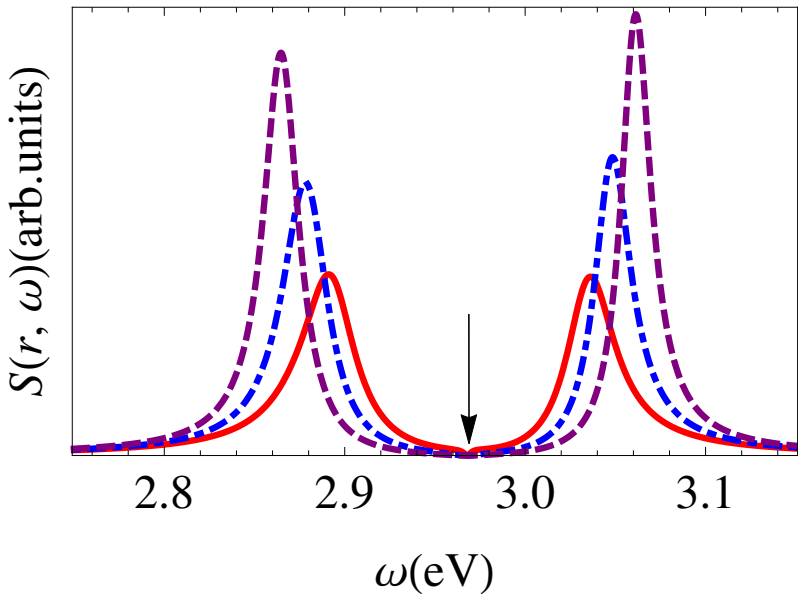

Figure 3.10: Calculated spectra for the QD located at $h = 2\ nm$ from the surface of the MNP with $R = 20\ nm$ and $\Delta_{23} = 0$ using the nondipole results with increasing Rabi fields, for $\Omega_L = 20$ (red, solid curve), 40 (blue, dashed-dotted curve), and 60 meV (purple, dashed curve) assuming the QD initially in the excited state. The dip or the dark region in the spontaneous emission spectra is designated by an arrow.

emitter. Therefore, most of the energy is transferred into the surface plasmons of the MNP. The coupling to far field or the radiation efficiencies is reduced [122]. With the large volume of the MNP, $R = 20\ nm$, and a small separation, the contribution from the dipole mode is approximately negligible and no effect may be observed. The energy coupling into the higher-order plasmon modes may be reduced with larger separations. We have found from the calculation of the emission spectra (not shown) that, the effects of the absorption can be reduced dramatically and the scattering can be increased by increasing the size of the MNP structure.

In Fig. (3.10), we show the emission spectra for the case of the QD initially in the excited state, when $h = 2\ nm$ and $R = 20\ nm$. Here, we observed a dip or dark region in the emission spectra at the QD transition frequency ($\omega_d \simeq 2.968eV$), which

can be elucidated as the interference phenomena between the coherent laser field and the field generated by surface plasmon with the presence of the MNP. In Fig. (3.10), we show that the splitting with different control fields is larger and approximately symmetric due to the effect of the large size of the MNP. The height of these peaks are different and increase with the intensity of the control field. We have also found that the splitting of the emission spectrum can be further increased by decreasing the distances between the QD and the surface of the MNP. When the MNP moves far from the QD (not shown), the drastic reduction in the spectrum splitting is observed, along with the narrowing of the spectra peaks which is a manifestation of the effects played by the MNP on the spectrum. This specificity can be exploited to accomplish spectral selectivity for different MNP sizes and separation distances. With the absence of the coherent laser field, the results in Fig. (3.10) resemble to that presented in Fig. (3.6).

In Fig (3.11), we have further investigated the non-Markovian decay dynamics of $\rho_{11}(t) = |C_1(t)|^2$ for the QD initially in its ground state $|3\rangle$ with the present of the control driving field. The oscillations dynamics is a manifestation of the important role from the MNP. This effect is observable even with the significant metal losses. This assertion can be checked by looking at different locations of the QD from the surface of the MNP as shown in Fig. (3.11b). In Fig. (3.11a), we show the non-Markovian dynamics of $\rho_{11}(t)$ for the QD located at $h = 2\ nm$ for different control fields. With increasing the intensity Ω_L, the non-Markovian dynamics has similar features. However, the oscillation of the $\rho_{11}(t)$ is larger and it may starts at an earlier time.

In Fig. (3.11b), we demonstrate the non-Markovian dynamics $\rho_{11}(t)$ of the QD for different separations of the QD-MNP system. Here, $R = 10\ nm$ and $\Omega_L = 50\ meV$. When the LDOS becomes very large, entering the strong coupling regime is

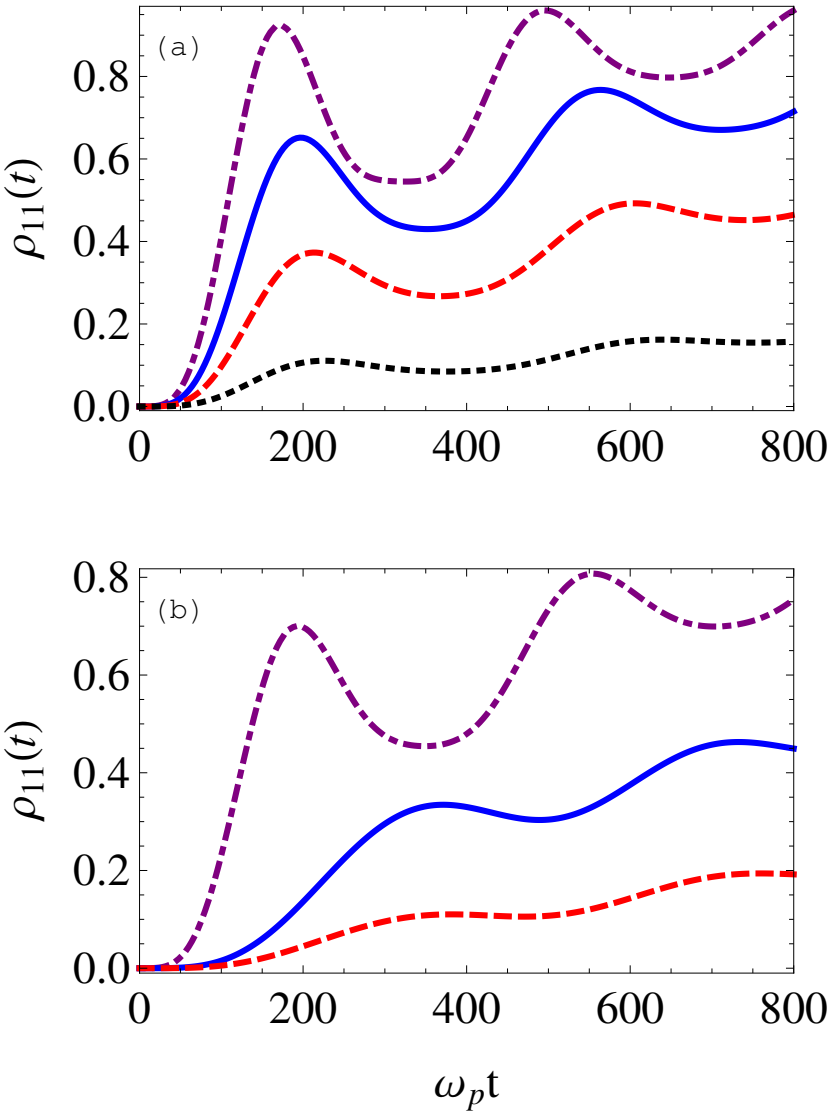

Figure 3.11: (a) Evaluation of the non-Markovian decay dynamics of the QD, $\rho_{11}(t) = |C_1(t)|^2$, for $\Omega_L = 15\ meV$ (black, dotted line), $30\ meV$ (red, dashed line), $50\ meV$ (blue, solid line), and $70\ meV$ (purple, dashed-dotted line). Here, $h = 2\ nm$, $R = 10\ nm$, and $\Delta_{23} = 0$. (b) Evaluation of the non-Markovian decay dynamics of the QD, $\rho_{11}(t) = |C_1(t)|^2$, for $h = 10\ nm$ (red, dashed line), $7\ nm$ (blue, solid line), and $2\ nm$ (purple, dashed-dotted line). Here, $R = 10\ nm$, $\Omega_L = 50\ meV$, and $\Delta_{23} = 0$.

accessible where instead of the irreversible process of the emitter dynamics decaying and emitting a photon into the environment (i.e., weak coupling), the emitter can reversibly exchange the photon with the environment resulting in the oscillations.

When the QD moves far from the surface of the MNP, $h = 10\ nm$, the dipole-dipole interaction is very weak. The local fields of surface plasmons which provide feedback by stimulating $|2\rangle \leftrightarrow |1\rangle$ transition is insignificant. Therefore, $\rho_{11}(t)$ increases very slowly and the oscillations are diminished as shown in the red dashed line.

3.5 Discussion and conclusion

We have investigated the control of spontaneous emission spectra in a QD-MNP system. The strong coupling regime in this system is demonstrated by the Rabi splitting when the QD is located very close from the surface of the MNP and their optical transition frequencies are resonant with each other. Nevertheless, when the QD exciton moves far away from the MNP, that is, with Markov approximation, only the Lorentzian-type spectrum can be observed. We have demonstrated that the spontaneous decay and the emission spectrum of the transition coupled to the surface plasmons may be further modified by the coherent control on the adjacent transitions. Moreover, we have presented a clear evidence for the role of the local surface plasmon resonances in the QD dynamics, i.e., the oscillatory behavior with the presence of the MNP is clearly noticeable. The advantage of our system is that the driving field is applied at a different frequency from that of the adjacent transition avoiding overheating effects which could degrade the performance of the MNP. This is practically important for designing devices such as spasers or dipole nanolasers [123].

Rapid advances in nanofabrication techniques for MNPs put such a system within experimental reach. One example is to prepare spin coating colloidal QDs onto a substrate, locating the dots by correlating photoluminescence informations with the atomic force microscopy (AFM) images and positioning the MNPs in the proximity of the QDs using the AFM cantilever tip to control the coupling between the QD

and the MNP. This was done by Ratchford et al. [48] who showed a dramatic change in the life time rate along with a drastic reduction in luminescence blinking. An alternative possible method for observing the emission spectra of coupled QD-MNP systems could use an array of MNPs arranged on a substrate with controllable inter-particle separation distances and immersed in a solution of colloidal QDs [124]. Our work is motivated by the development of plasmonic-based applications and a lot of interesting discoveries of quantum plasmonics. Since plasmonics has emerged as a promising technique for optically trapped [125, 126] within nanoscale region, we are anticipating that our results may have potential applications for nanoswitch applications in plasmonic nanoparticles.

4. NANOSHELL-MEDIATED ROBUST ENTANGLEMENT BETWEEN COUPLED QUANTUM DOTS *

4.1 Introduction

Conducting nanostructures at optical frequencies have long held the promise for multiple technological applications. Such structures have recently received considerable interest due to their potential in achieving strong, coherent coupling between individual emitters and electromagnetic excitations via excitation of plasmons localized to nanoscale dimensions. This strong coupling is possible due to the small mode volume associated with the subwavelength surface-plasmonic confinement [127]. By confining the light into nanoscale volumes, various interesting plasmonic elements allow, for example, for a nanoscale realization of Mollow triplet of emission spectra [92, 93] and non-classical photon correlations between the emissions from the quantum dot and the ends of nanowire [94]. Furthermore, plasmon-enhanced photocatalytic activity has been investigated experimentally in the spirit of the interplay of a coupled nanocomposite system consisting of quantum dot (QD) and metal nanoparticle (MNP) [107]. Also, the interplay and modification of the photoexcitation processes in a hybrid system composed of QD and MNP is treated self consistently [108] by applying the theoretical work reported in [106]. In addition, integrating semiconductor QDs with MNP provides useful means to couple light and matter. This coupling can be enhanced tremendously by placing QDs in proximity to nanostructured optical environment that enable strong confinement of light and thus increase the light-matter interaction. Remarkably, QDs offer many advantages over

*Reprinted with permission from "Nanoshell-mediated robust entanglement between coupled quantum dots," by Jabir Hakami and M. Suhail Zubairy, 2016, Phys. Rev. A, vol 93, p. 022320, copyright [2016] by American Physical Society.

the atomic systems including the small size, large optical dipole moments and transition energies, and they can be positioned deterministically and remain stationary without requiring atom traps [53, 54].

One of the fascinating applications of these nanostructures is their ability to generate entangled states of a two-qubit system. It has been demonstrated that semiconductors QDs are promising candidates for the basic device units for quantum information processing [50, 51]. Fundamentally, a light-matter strong interaction is prerequisite to generate entanglement between quantum bits (qubits) for optical quantum information systems. Recently, the entanglement dynamics in a system consisting of two identical quantum emitters in the vicinity of a solid sphere MNP is investigated [128, 129]. However, in these models the MNPs are treated in a quasistatic approximation where the contribution of retardation effects are ignored. Also, while the spherical MNP has a simpler structure, the plasmon resonance appears at higher frequencies where the contribution of the interband absorption is magnified, thus leading to a fast decay of entanglement. On the other hand, nanoshells with extraordinary properties support surface plasmon resonances (SPRs) that are highly geometric-dependent (their resonance frequencies depend significantly on the shell thickness) and they respond more sensitively to the changes in the environment [55]. This leads to a structure that has extraordinary properties.

In the present work [130], we study the entanglement generation in a hybrid structure, consisting of two QDs in the vicinity of a metal nanoshell. The entanglement arises impulsively due to common coupling to the plasmonic nanostructure, without demanding postselective measurement or mediating the dissipative environment. We use a self-consistent photon Green's function technique to explore the quantum optical and entanglement dynamics between two QDs that cover all the coupling regimes. We demonstrate that the QDs, which are resonantly coupled to the nanoshell with

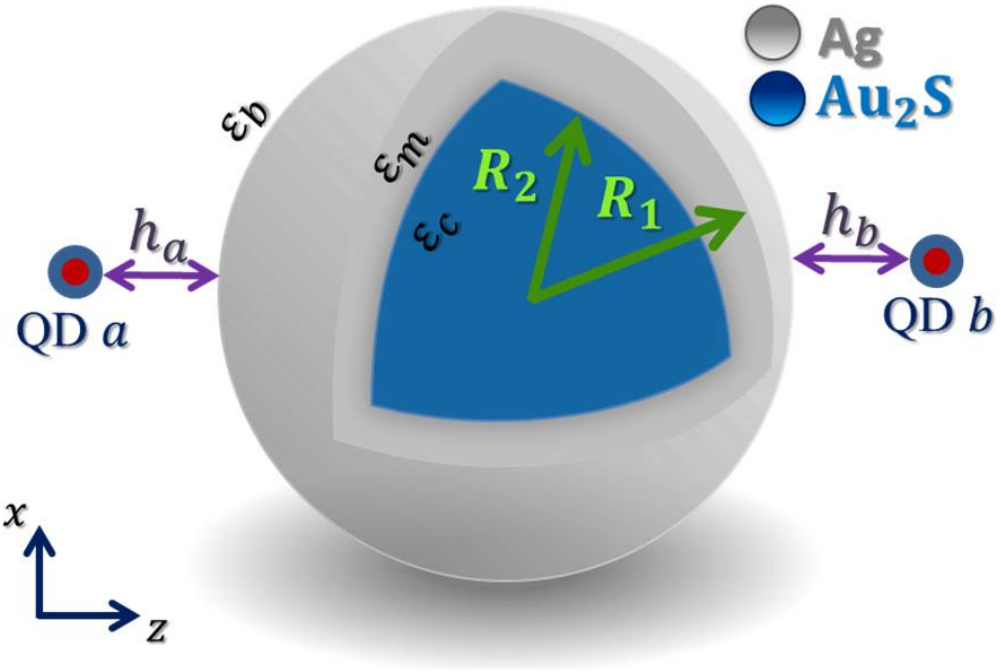

Figure 4.1: Schematic diagram of the hybrid system consisting of two QDs labelled QD a and QD b located at different distances $r_a = R_1 + h_a$ and $r_b = R_1 + h_b$ from the center of a Au_2S/Ag nanoshell. The QDs-nanoshell system is embedded in a homogeneous background medium with permittivity ϵ_b. The Au_2S core has radius R_2 and dielectric constant ϵ_c. The concentric Ag shell has a total nanoparticle radius R_1 and permittivity $\epsilon_m(\omega)$.

only one being initially excited, can form coherent superposition state significantly faster than the losses in the system. We have found that the long-lived entangled state depend perceptively on the shell thickness as well as on the ratio of the distances between the two QDs and the surface of the shell. Contrary to a nanosphere, the entanglement mediated by a nanoshell is robust even when the dephasing rate and the detuning between the transition frequencies of the two QDs are rigorously included.

The organization of this chapter is as follows. In the next subsection, we present

the theoretical model for the hybrid system. In Sec. 4.2, we study the enhancement of the local density of states in the proximity of the nanoshell. In Sec. 4.3 , we calculate and discuss the results of the concurrence of two QDs in homogeneous background, coupled by the nanoshell localized surface plasmon. Our conclusion is presented in Sec. IV.

4.2 Theoretical framework

4.2.1 Model and Hamiltonian.

The hybrid system consisting of two QDs in the proximity of a metal nanoshell is schematically presented in Fig. (4.1). The QDs labelled QD a and QD b are located at distances h_a and h_b with respect to the surface of the metallic shell. Unless stated otherwise, the structure of the nanoshell is modelled as a spherical Au_2S core of radius R_2 and permittivity $\epsilon_c = 5.4$ [131]. Surrounding Au_2S core is a concentric Ag shell of $d = R_1 - R_2$ with a frequency-dependent dielectric permittivity $\epsilon_m(\omega)$ taken from Ref. [114]. Here, R_1 is the external radius of the shell. The core-shell system is entrenched in an aqueous medium of dielectric constant $\epsilon_b = 1.78$ [131]. The distances from QD a and QD b from the center of the nanoshell are $r_a = R_1 + h_a$ and $r_b = R_1 + h_b$, respectively. The QDs are treated as two-level systems for resonant excitation of the energetically lowest electronic transition between valence and conduction band states. The methodology to map the full many body problem on a discrete energy level scheme for the strongly confined excitons is advocated by numerous theoretical and experimental studies [50, 132, 133, 134, 135, 136]. Each QD is modelled as a two-level system with the optical transition frequency ω_i for the ith QD, internal nonradiative decay rate γ_i', and the transition dipole moment $\boldsymbol{d}_i$.

The size-dependent dielectric function due to the finite-size effect of the nanoparticle can be accounted empirically using the "limited mean free path model" [137].

In this model, the damping constant is given by $\Gamma = \Gamma_{bulk} + A\upsilon_F/\ell$, where Γ_{bulk} is the damping constant for the bulk, $\upsilon_F = 1.39 \times 10^8 cm/s$ is the Fermi velocity of the conduction electrons in the silver, and ℓ is the characteristic dimension depending on the geometry of the nanoparticle which is in our model proportional to the thickness of the nanoshell. The constant A depends on the nanoparticle shape and on the theory. The best agreement with the experiments is found for $A = 0.25$ [138]. Here, the frequency-dependent dielectric function of the silver nanoshell including the size effect can be expressed as [137]

$$\epsilon_m(\omega, d) = \epsilon_{exp}(\omega) + \frac{\omega_p^2}{\omega^2 + i\omega\Gamma_{bulk}} - \frac{\omega_p^2}{\omega^2 + i\omega\Gamma}, \tag{4.1}$$

where $\omega_p = 1.3987 \times 10^{16} s^{-1}$ is the bulk plasmon frequency, and $\Gamma_{bulk} = 0.03 \times 10^{15} s^{-1}$ is the bulk collision frequency of conduction electrons in silver. $\epsilon_{exp}(\omega)$ is the experimental frequency-dependent dielectric function taken from Ref. [114].

To scrutinize the strong coupling case, we adopt a macroscopic QED formalism [127, 109] for calculating the entanglement of coupled QDs in a lossy, nonhomogeneous environment. It relies on the diagonalization of a Hamiltonian that includes the coupled QDs, the electromagnetic modes of the nanoshell metal nanoparticle including their inherent losses, and the light matter coupling by means of a dipolar interaction,

$$\begin{aligned} \hat{H} = &\int d\boldsymbol{r} \int_0^\infty d\omega \hbar\omega \hat{\boldsymbol{f}}^\dagger(\boldsymbol{r}, \omega) \cdot \hat{\boldsymbol{f}}(\boldsymbol{r}, \omega) + \sum_{i=a,b} \frac{\hbar\Omega_i}{2} \hat{\sigma}_i^z \\ &- \sum_{i=a,b} \int_0^\infty d\omega \left[[\hat{\sigma}_i^- + \hat{\sigma}_i^+] \boldsymbol{d}_i \cdot \hat{\boldsymbol{E}}(\boldsymbol{r}_i, \omega) + \text{H.c.} \right], \end{aligned} \tag{4.2}$$

where $\Omega_i = \omega_i - i\gamma_i'/2$. Here, $\hat{\boldsymbol{f}}(\boldsymbol{r}, \omega)$ is the bosonic vector field annihilation operator

for the elementary excitations of the system. The QDs are described in terms of the fermionic operators $\hat{\sigma}_i$. The first and the second terms shown in Eq. (4.2) describe the noninteracting Hamiltonian of the total electromagnetic field and the energy of the QDs, respectively. The third term illustrates the interaction energy between QDs and the excitation of surface plasmon at the QDs locations.

The electric field is quantized by introducing the media as phenomenological noise currents that are associated with the electric and magnetic losses due to material absorption in Maxwell's equations, and the field operators are obtained indirectly from the noise operators via the classical Green's function. The electric field operator at the position of the QD is given by [109]

$$\begin{aligned}\hat{\boldsymbol{E}}(\boldsymbol{r},\omega) =& i\sqrt{\frac{\hbar}{\pi\epsilon_0}}\int d\boldsymbol{r}'\frac{\omega^2}{c^2} \\ &\times\sqrt{\epsilon_I^m(\boldsymbol{r}',\omega)}\boldsymbol{G}(\boldsymbol{r},\boldsymbol{r}',\omega)\hat{\boldsymbol{f}}(\boldsymbol{r}',\omega),\end{aligned} \tag{4.3}$$

where ϵ_I^m is the imaginary part of the complex dielectric function $\epsilon_m(\boldsymbol{r},\omega) = \epsilon_R^m(\boldsymbol{r},\omega) + i\epsilon_I^m(\boldsymbol{r},\omega)$ and $\left[\hat{f}_{\lambda i}(\boldsymbol{r},\omega), \hat{f}^\dagger_{\lambda' j}(\boldsymbol{r}',\omega')\right] = \delta_{\lambda\lambda'}\delta_{ij}\delta(\boldsymbol{r}-\boldsymbol{r}')\delta(\omega-\omega')$, $\left[\hat{f}_{\lambda i}(\boldsymbol{r},\omega), \hat{f}_{\lambda' j}(\boldsymbol{r}',\omega')\right] = 0$. Here, $\boldsymbol{G}(\boldsymbol{r},\boldsymbol{r}',\omega)$ is the frequency-dependent electromagnetic Green's function, describing the system response at $\boldsymbol{r}$ to a point source at $\boldsymbol{r}'$:

$$\left[\boldsymbol{\nabla}\times\boldsymbol{\nabla}\times -\frac{\omega^2}{c^2}\epsilon_m(\boldsymbol{r},\omega)\right]\boldsymbol{G}(\boldsymbol{r},\boldsymbol{r}',\omega) = \boldsymbol{I}\boldsymbol{\delta}(\boldsymbol{r}-\boldsymbol{r}'), \tag{4.4}$$

where $\boldsymbol{I}$ is the unit dyadic. In this hybrid system, the direct dipole-dipole interactions are naturally included in the total Green's function.

Before closing this theory section, we highlight that our general approach can be adapted beyond the dipole approximation in order to include non-dipole effects for the QDs using the same Green function introduced above [54, 139, 140]. Nonetheless,

the dipole approximation is justified for strongly confined dots where the higher-lying energy levels become substantially separated [141, 98]. We have found that the near-field distributed uniformly over a small volume of QD, showing a good agreement with the results reported in Ref. [98]. Additionally, Kristensen et al. [142] have verified that the Purcell effect is independent of the size of the wave function for the case of spherically symmetric exciton wave functions, i.e., is determined only by the photonic response in the center of the emitter. For a practical application, their exact calculations have been confirmed by computing the Purcell factor for a spherical QD near a silver metal and the conclusion is that the results coincide with the dipole approximation and there is no spatial averaging of the local density of states across the volume of the QD, in spite of the large field gradients near the metal in their structure. It is meaningful to compare this to the experimental results reported in Ref. [54] where the dipole approximation failed for relatively small self-assembled QDs. This is because, for simplicity, we consider only heavy-hole transitions and leave the modeling of strained QDs for future studies.

4.2.2 Modified spontaneous emission dynamics

We consider the decay dynamics of the two coupled QDs that have the states a and b as their respective upper excited level. The initial field is assumed to be in vacuum, thus all the resultant dynamics in this system will be driven by the initial excitation of QDs. We assume that, at most, one QD is excited at any time. Thus a possible initial condition is that the QD system is in the state $|\psi(t=0)\rangle = C_a(0)\,|U_a\rangle + C_b(0)\,|U_b\rangle$, where $|U_a\rangle \equiv |1\rangle_a\,|0\rangle_b$ and $|U_b\rangle \equiv |0\rangle_a\,|1\rangle_b$, which can be prepared through appropriate optical or electronic excitation of the solid state QD system. Here, $|0\rangle_i$ and $|1\rangle_i$ represent the ith QD in the ground and excited state, respectively.

The time evaluation for this initial state is given by

$$|\psi(t)\rangle = \sum_i C_i(t) e^{-i(\Omega_i - \overline{\Omega})t} |U_i\rangle |0\rangle + \int d\boldsymbol{r} \int_0^\infty d\omega C_L(\boldsymbol{r}, \omega, t) e^{-i(\omega - \overline{\Omega})t} |L\rangle |\mathbf{1}(\boldsymbol{r}, \omega)\rangle , \tag{4.5}$$

where $|\mathbf{1}(\boldsymbol{r}, \omega)\rangle = \hat{\boldsymbol{f}}^\dagger(\boldsymbol{r}, \omega) |\{0\}\rangle$, $|L\rangle$ is the state where both QDs are in the lower state, i.e., $|L\rangle = |0\rangle_a |0\rangle_b$, and $\overline{\Omega}$ is the average of the frequencies Ω_i where in the case of $\gamma_i' = 0$, we have $\overline{\Omega} = \overline{\omega} \equiv \frac{1}{2} \sum_i \omega_i$ ($i = a$ or b).

The time-dependent Schrödinger equation in the rotating wave approximation leads to the following equation of motion for the probability amplitudes

$$\dot{C}_i(t) = -\frac{1}{\sqrt{\hbar \pi \epsilon_0}} \int_0^\infty d\omega \frac{\omega^2}{c^2} \int d\boldsymbol{r} \sqrt{\epsilon_I(\boldsymbol{r}, \omega)} \times \boldsymbol{d}_i^* \cdot \boldsymbol{G}(\boldsymbol{r}_i, \boldsymbol{r}, \omega) C_L(\boldsymbol{r}, \omega, t) e^{-i(\omega - \Omega_i)t}, \tag{4.6a}$$

$$\dot{C}_L(\boldsymbol{r}, \omega, t) = \frac{1}{\sqrt{\hbar \pi \epsilon_0}} \frac{\omega^2}{c^2} \sqrt{\epsilon_I(\boldsymbol{r}, \omega)} \times \sum_j \boldsymbol{d}_j \cdot \boldsymbol{G}^*(\boldsymbol{r}_j, \boldsymbol{r}, \omega) C_j(t) e^{i(\omega - \Omega_j)t}, \tag{4.6b}$$

where we assumed for the pure dephasing rate $\gamma_i' = \gamma_{a/b}'$. Integrating Eq. (4.6*b*) and substituting into Eq. (4.6a), we obtain the integro-differential equations for the probability amplitudes $C_i(t)$. Introducing the kernel function $K_{r_i r_j}(t, t')$ leads to

$$\dot{C}_a(t) = -\int_0^t dt' [K_{r_a r_a}(t, t') C_a(t') + K_{r_a r_b}(t, t') C_b(t')], \tag{4.7a}$$

$$\dot{C}_b(t) = -\int_0^t dt' [K_{r_b r_b}(t, t') C_b(t') + K_{r_b r_a}(t, t') C_a(t')], \tag{4.7b}$$

where the kernel function

$$\begin{aligned} K_{r_i r_j}(t,t') =& \frac{1}{\hbar\pi\epsilon_0}\int_0^\infty d\omega e^{-i(\omega-\Omega_i)t}e^{i(\omega-\Omega_j)t'} \\ & \times \boldsymbol{d}_i^* \cdot \left\{\frac{\omega^2}{c^2}\mathrm{Im}[\boldsymbol{G}(\boldsymbol{r}_i,\boldsymbol{r}_j,\omega)]\right\}\cdot \boldsymbol{d}_j \\ =& \int_0^\infty d\omega J_{ij}(\omega)e^{-i(\omega-\Omega_i)t}e^{i(\omega-\Omega_j)t'}. \end{aligned} \tag{4.8}$$

(i,$j = a$ or b). Taking the time integral of both sides of Eqs. (4.8), leads to well-known Volterra integral equations of the second kind [115].

Here, the action of the dissipative medium depicted in Fig. (4.1) on the ith QD is described by the so-called spectral density [112] defined as

$$J_{ii}(\omega) = \frac{1}{\hbar\pi\epsilon_0}\boldsymbol{d}_i^* \cdot \left\{\frac{\omega^2}{c^2}\mathrm{Im}[\boldsymbol{G}(\boldsymbol{r}_i,\boldsymbol{r}_i,\omega)]\right\}\cdot \boldsymbol{d}_i. \tag{4.9}$$

This expression can be expressed in terms of the electromagnetic density of states as

$$J_{ii}(\omega) = \frac{1}{2}\frac{\omega}{3\hbar\epsilon_0}|\boldsymbol{d}_i|^2\rho(\boldsymbol{r}_i,\omega), \tag{4.10}$$

where $\rho(\boldsymbol{r}_i,\omega)$ is the local density of state expressed in terms of the system's dyadic Green's function as

$$\rho(\boldsymbol{r}_i,\omega) = \frac{6\omega}{\pi c^2}\left\{\boldsymbol{n}_p \cdot \mathrm{Im}[\boldsymbol{G}(\boldsymbol{r}_i,\boldsymbol{r}_i,\omega)]\cdot \boldsymbol{n}_p\right\}, \tag{4.11}$$

where $\boldsymbol{n}_p$ is a unit vector pointing in direction of $\boldsymbol{p}$. The enhancement of the projected local density of state, in direction $\boldsymbol{n}_p$, is defined as

$$F_{\boldsymbol{n}_p}(\omega) = \frac{\boldsymbol{n}_p \cdot \mathrm{Im}[\boldsymbol{G}(\boldsymbol{r}_i,\boldsymbol{r}_i,\omega)]\cdot \boldsymbol{n}_p}{\boldsymbol{n}_p \cdot \mathrm{Im}[\boldsymbol{G}^0(\boldsymbol{r}_i,\boldsymbol{r}_i,\omega)]\cdot \boldsymbol{n}_p}, \tag{4.12}$$

where $\mathrm{Im}[\boldsymbol{G}^0(\boldsymbol{r}_i, \boldsymbol{r}_i, \omega)] = \frac{k_1}{6\pi}\boldsymbol{I}$ is the imaginary part of the homogeneous Green tensor. Here, $k_1 = \omega\sqrt{\epsilon_b}/c$ where ϵ_b is the dielectric constant of the surrounding medium. In this case, all the matter parameters that are relevant to the geometrical and materia information are directly included in the Greens function. The plasmon resonance can be obtained including retardation effect from the explicit form of the reflection coefficients derived in Appendix B by noticing that these coefficients contain poles at the points where the denominator vanishes. These poles give the eigenfrequency relation of the the electric modes supported by the metallic shell. The detail derivations are given in Appendix D.

The enhancement of the z-projected local density of states, $F_z(\omega)$, for a QD exciton located at $\boldsymbol{r}_{a/b} = 19\ \hat{\boldsymbol{e}}_z$ from the center of the Au_2S/Ag nanoshell is shown in Fig. (4.2a). The plasmon resonance peaks can be obtained analytically from the solutions of the eigenfrequency relation given in Appendix D [see Eq. (D1)]. Each mode splits into two modes, cavity-like ω_{n+} at high frequencies (antisymmetric SPR modes) converging to $\sum_n \omega_{n+}$ and sphere-like ω_{n-} modes at low frequencies (symmetric SPR modes). The splitting originates from the hybridization or coupling of plasmons bound to different (internal and external) surfaces of the shell. In Fig. (4.2a), the low frequencies modes $\omega_{n-}$are shown explicitly and the converged high frequencies modes $\sum_n \omega_{n+}$ are shown as the peak on the right. This doublet structure of optical spectra of metallic shells has been demonstrated theoretically and observed experimentally [137]. Remarkably, the localized SPR in our structure appears at low frequency around 1.6 eV, which is close to the wavelengths that have potential applications in the biomedicine, optical communication, and for many QD emitters. The appearance of this resonance frequency in the near-infrared, where the losses of the metal silver are at a minimum, results in the spectral width, i.e., the full width at half-maximum (FWHM) of only 18 meV (see Fig. (4.2a). Interestingly,

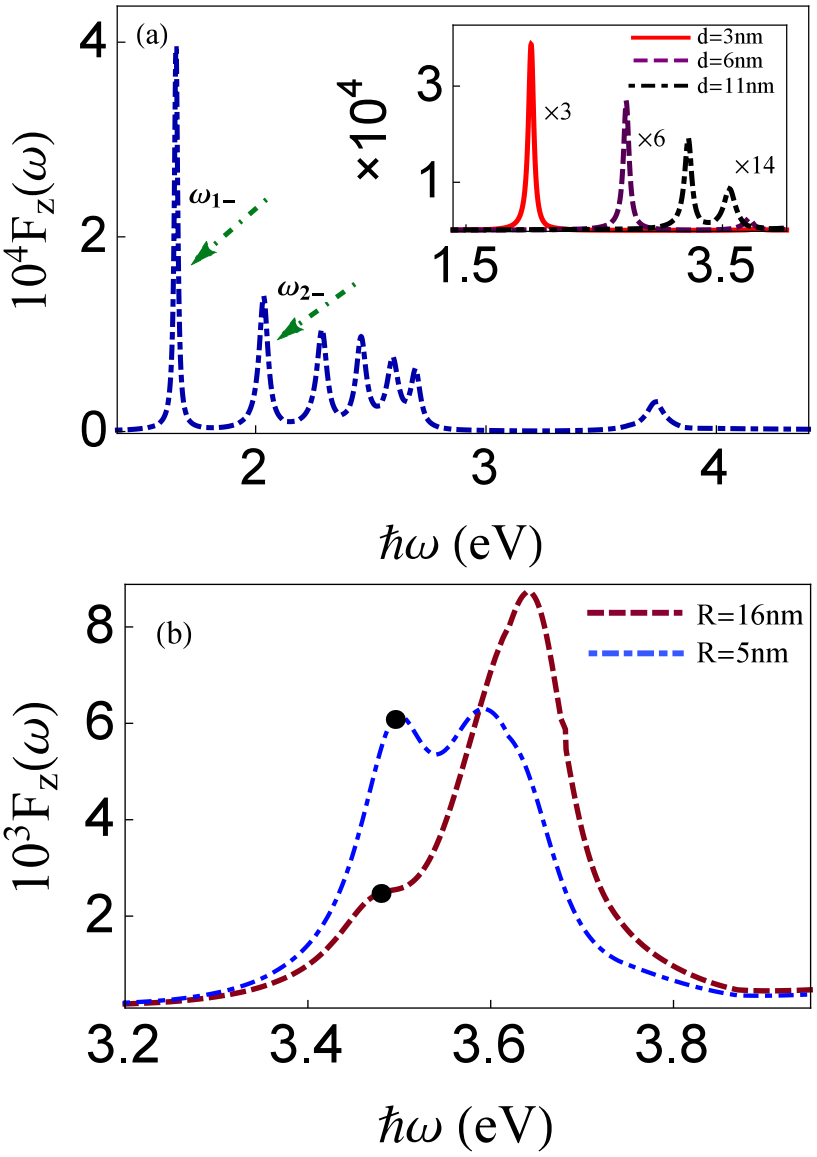

Figure 4.2: (a) Enhancement of z-projected local density of state, $\hat{\boldsymbol{e}}_z \cdot \mathrm{Im}[\boldsymbol{G}(\boldsymbol{r}_{a/b}, \boldsymbol{r}_{a/b}, \omega)] \cdot \hat{\boldsymbol{e}}_z$ in units of $\hat{\boldsymbol{e}}_z \cdot \mathrm{Im}[\boldsymbol{G}^0(\boldsymbol{r}_{a/b}, \boldsymbol{r}_{a/b}, \omega)] \cdot \hat{\boldsymbol{e}}_z$ calculated at $h_{a/b} = 3nm$ from the surface of a Au_2S/Ag nanoshell. The Au_2S core has radius $R_2 = 14nm$ and refractive index $n_c^2 \equiv \epsilon_c = 5.4$. The concentric shell has a total radius $R_1 = 16nm$ and frequency-dependent permittivity $\epsilon_m(\omega, d)$ given in the text. Inset: The dependence of the plasmon resonance on the shell thickness (in the dipole approximation): $d = 3nm$ (solid red curve), $6nm$ (dash purple curve), and $d = 11nm$ (dash-dotted black curve). (b) Enhancement of z-projected local density of state calculated at $h_{a/b} = 3nm$ from the surface of a Ag solid sphere nanoparticle with different radius: $R = 16nm$ (dash red curve) and $R = 5nm$ (dash-dotted blue curve). Here, $\epsilon_c \equiv \epsilon_m(\omega) = \epsilon_m(\omega, R)$. The location of the localized SPRs are indicated by superimposed black dots on the curves.

the inverse of the linewidth of the nanoparticle plasmon is directly proportional to the field strength at the surface of the nanoshell. The dependence of the localized SPR on the shell thickness is shown (in the dipole approximation) in the inset of Fig. (4.2a). These results show the strong sensitively of the plasmon resonance to the shell thickness although the outer radius is fixed at 16 nm. In addition, the interband contribution diminishes the intensity of the SPR if it occurs at shorter wavelengths than the threshold wavelength. This explains the lower intensities for the shell thickness $d = 11nm$ (dash-dotted black curve) than for $d = 3nm$ (solid red curve).

In Fig. (4.2b) we demonstrate the enhancement of the z-projected local density of states, $F_z(\omega)$, for the case of a solid sphere nanoparticle with different sizes: $R = 16nm$ (dash red curve) and $R = 5nm$ (dash-dotted blue curve). This is a consequence of the fact that when $\epsilon_c \equiv \epsilon_m(\omega) = \epsilon_m(\omega, R)$, the coefficients of the shell-core nanoparticle [see Appendix B] reduces to those of a solid sphere with radius R_1. The location of the localized SPRs are indicated by superimposed black dots on the curves. In contrast to the nanoshell (Fig. (4.2a), the localized SPRs for the solid sphere occurs at higher frequencies near 350 nm, where the interband absorption is magnified. Additionally, the corresponding localized SPR is redshifted slightly and broadened with increasing the size of the nanoparticle. In this case, the contribution of the retardation effects are dominated and the reservoir function $\rho(\boldsymbol{r}_i, \omega)$ cannot be described by a single Lorentzian lineshape.

In Fig. (4.3), we exemplify the dependence of the local density of states on the geometric of the nanoshell. Here, Eq. (4.13) is calculated numerically for two different core materials: (a) Si with the highest refractive index [143] and (b) SiO_2 with the lowest refractive index [144]. Recently, it was established that the silicon/silver (Si/Ag) interface is significantly importance in industrial solar cells and understand-

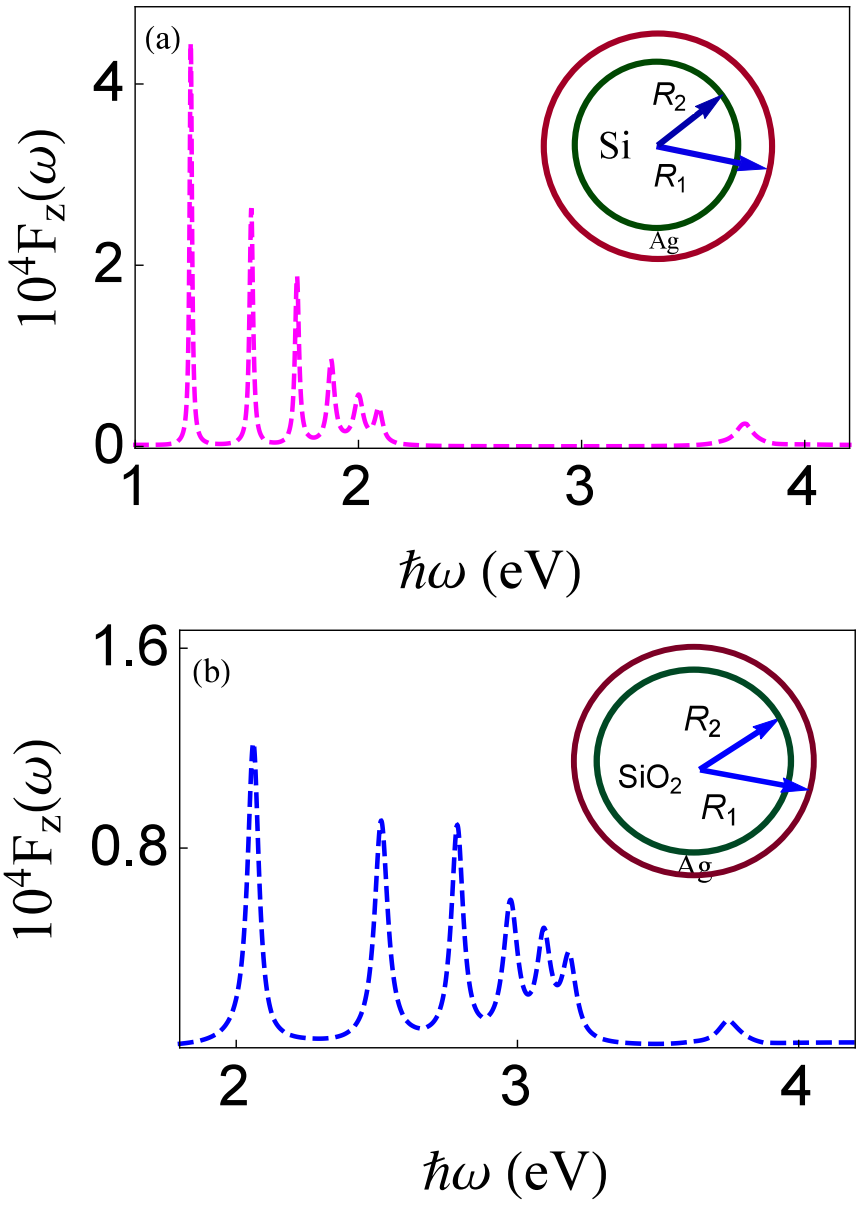

Figure 4.3: Enhancement of z-projected local density of state, $\hat{\boldsymbol{e}}_z \cdot \mathrm{Im}[\boldsymbol{G}(\boldsymbol{r}_{a/b}, \boldsymbol{r}_{a/b}, \omega)] \cdot \hat{\boldsymbol{e}}_z$ in units of $\hat{\boldsymbol{e}}_z \cdot \mathrm{Im}[\boldsymbol{G}^0(\boldsymbol{r}_{a/b}, \boldsymbol{r}_{a/b}, \omega)] \cdot \hat{\boldsymbol{e}}_z$ calculated at $h_{a/b} = 3nm$ from the surface of a (a) Si/Ag nanoshell and (b) SiO_2/Ag nanoshell, respectively. It exemplifies the dependence of the local density of states on the geometric of the nanoshell. Here, equation (2.14) is calculated numerically for two different core materials: (a) Si with the highest refractive index and (b) SiO2 with the lowest refractive index. The spherical silicon core, Si, has radius $R_2 = 14nm$ and refractive index $n_c = 3.42$ while the spherical silica core, SiO_2, has radius $R_2 = 14nm$ and refractive index $n_c = 1.46$. The concentric shell, Ag, has a total radius $R_1 = 16nm$ and frequency-dependent permittivity $\epsilon_m(\omega, d)$ given in the text. Inset: Sketch of the shell-core nanoparticle with different core material.

ing and tailoring the metal-semiconductor interface is practically important in all semiconductor devices [145]. In Fig. (4.3a), we show that the silicon core can significantly influence the optical properties of metal nanoshell. The localized SPR peak is considerably redshifted and the FWHM becomes very narrow. Thus, increasing the core dielectric constant increases nanoparticle absorption efficiency, reduces plasmon line width, and adjusts plasmon energies. These results agree very well with the elaborate experiment reported in Ref. [146]. This is encouraging results showing that even the higher-order modes such as quadrupole SPR become practically useful due to significant low losses. This leads to a structure that has extraordinary properties. This is in contrast to the results shown in Fig. (4.3b) for the SiO_2 core where the linewidth is enlarged and losses as a result of the contributions of the higher-order modes become severe.

4.3 Results and discussion

In this section, we have numerically solved the time-dependent dynamical equations (4.8) motivated with the results in Figs. (4.2) and (4.3) to demonstrate the decay evolutions of the QDs excitons and the corresponding entanglement with QD a being initially excited, i.e., with the initial wave function $|\psi(t=0)\rangle = |1\rangle_a |0\rangle_b$. The population dynamics is exact as we have performed neither Born nor the Markov approximation. For all numerical calculations, we have considered parameters from single QD optical experiment with optical dipole moment $d_{a/b} = d_0 = 60D$ (Debye) [147]. In addition, we assume the pure dephasing rate $\gamma_i' = \gamma_{a/b}' = 1\ \mu eV$ (equal for all QDs) as demonstrated in the recent experiments for the decay of InAs QDs at room temperature [148, 119]. Note that even for a larger rate of $\gamma' = 1\ meV$, the numerical results are essentially identical since the plasmon coupling completely dominates the decay.

The quantum entanglement of a two-qubit system can be well quantified by the concurrence $\mathcal{C}(t)$, ranging from zero for separable states up to one for maximally entangled states, which is given by [149]

$$\mathcal{C}(\rho) = \max\{0, \lambda_1 - \lambda_2 - \lambda_3 - \lambda_4\}, \tag{4.13}$$

where λ_i $(i = 1, 2, 3, 4)$ are the eigenvalues, in descending order, of the Hermitian matrix $\Lambda = \sqrt{\sqrt{\rho_{ab}}\tilde{\rho}_{ab}\sqrt{\rho_{ab}}}$. The spin-flip density matrix is defined as $\tilde{\rho}_{ab} = (\sigma_y \otimes \sigma_y)\rho^*_{ab}(\sigma_y \otimes \sigma_y)$ where σ_y is a Pauli matrix.

In the $\{|11\rangle, |10\rangle, |01\rangle, |00\rangle\}$ basis, the reduced density matrix for the QDs is determined by tracing out the plasmons mode which can be calculated to be

$$\rho_{ab}(t) = \begin{pmatrix} 0 & 0 & 0 & 0 \\ 0 & |C_a(t)|^2 & C_a(t)C_b^*(t)e^{-i\Delta} & 0 \\ 0 & C_a^*(t)C_b(t)e^{i\Delta} & |C_b(t)|^2 & 0 \\ 0 & 0 & 0 & 1 - |C_a|^2 - |C_b|^2 \end{pmatrix}, \tag{4.14}$$

where $\Delta = \omega_a - \omega_b$ is the difference (mismatch) of the transition energies of individual QDs. Hence for the density matrix given by Eq. (4.15), the concurrence takes the form

$$\mathcal{C}(t) = 2\max\{0, |C_a(t)C_b^*(t)|\}. \tag{4.15}$$

To better discuss the dynamical evaluation of the entanglement, we consider the initial state $|\psi(t=0)\rangle = C_a(0)|U_a\rangle + C_b(0)|U_b\rangle$ with $C_a(0) = \sqrt{\frac{1-s}{2}}$ and $C_b(0) = \sqrt{\frac{1+s}{2}}e^{i\phi}$, where $-1 \leq s \leq 1$.

In Fig. (4.4), we show the dynamics of coupled QDs located symmetrically with respect to the Au_2S/Ag nanoshell (i.e., with $r_a = r_b$) as a function of normalized

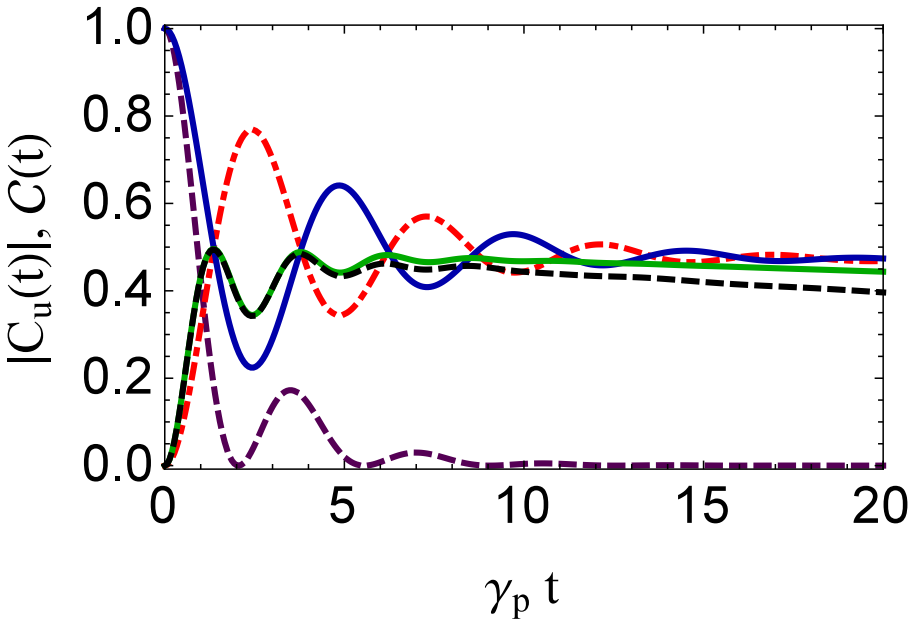

Figure 4.4: The coupling dynamics (exciton occupations and concurrence) between coupled QDs for the case of $s = -1$ as a function of normalized time; the upper decay of the QD a (solid blue curve), and b (dash-dotted red curve), and the concurrence (solid green curve). Here, $h_a = h_b = 3nm$. The dashed black curve shows the entanglement with 3.6 meV detuning between the QDs. The population dynamics of the QD a without QD b is shown in the dashed purple curve.

time . Here, we have assumed $\gamma_p = \Gamma_{bulk}$. We found that when both QDs being on resonance with the localized surface plasmon mode (i.e., $\omega_{n=1}$) and due to the enhancement of the local density of states ($F_z(\omega) \geq 10^4$), it leads to the dominating influence on the dynamic process of the QDs-nanoshell interactions. The existence of the Rabi oscillation in the decay profiles signifies the strong interaction between QDs in the proximity of surface plasmon nanoshell and, consequently, demonstrating that the decay dynamics contains the non-Markovian features. It is also demonstrated in Fig. (4.4) that the entangled state can be speeded up due to the Purcell effect as well as due to dealing with superradiant triplet state. The possibility of manipulating and speeding up the transition process might play a vital role in the future

development of quantum information processing. The exciton occupations is driven into a superposition state as shown in Fig. (4.4), which can be explained as follows. The oscillation of the initially excited QD creates plasmon excitation at the site of the metallic nanoshell. Subsequently, the strong medium-assisted photon exchange acting back on the QDs are $\pi/2$ phase shifted with respect to the field acting on the medium. This phase shift results in the redistribution of the energy of the initially excited QD, causing the system evolution towards the stable superposition state $(|1\rangle_a |0\rangle_b - |0\rangle_a |1\rangle_b)$. Consequently, the total field at the site of the nanoshell is quenched. The system sustains a stable superposition state until the retardation effects take place, which extract their energy in a non-radiative fashion. In this geometric arrangement, the entanglement oscillates ~ 0.5, which is the maximum amount possible (solid green curve). For comparison, we show the dynamics of QD a in the absence of QD b, which displays a smaller oscillation and a faster decay (dashed purple curve) compared to the presence of QD b. In addition, we also calculate the entanglement with realistic experimentally energy mismatch when the detuning $\Delta = \omega_a - \omega_b$ of the transition energies between the QDs is equal to 3.6 meV (dashed black curve). The resulting of concurrence is almost independent of Δ. This clearly indicates robustness of entanglement in our system.

The dipole asymmetry was also shown to offer a significant flexibility to derive quite different entanglement dynamics than the case of equal optical dipole moments by integrating planar-photonic-crystal (PPC) nanocavites with solid state [52]. However, the quality factor and the cavity mode volume in the latter system are always assumed to be very large, and subsequently reduces the quality factor in this system by one order of magnitude moving it in a weak coupling regime [52]. Such difficulties can be avoidable in our model, signifying the advantages of the nanoscale integration of metals and semiconductors.

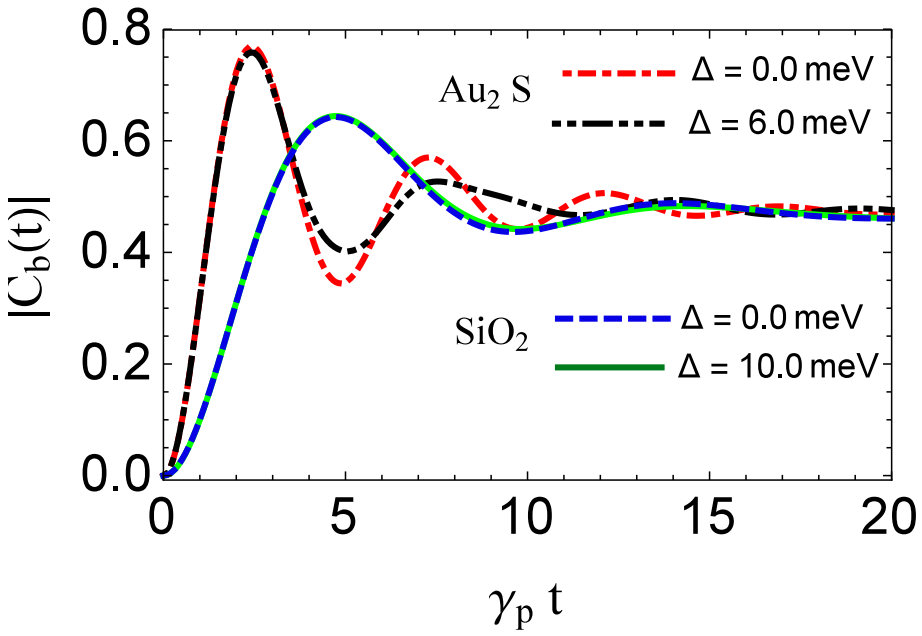

Figure 4.5: Evaluation of the non-Markovian decay dynamics of the QD b initially in the ground state as a function of normalized time with different core materials. Au_2S core: $\Delta = 0meV$ (dash-dotted red curve) and $\Delta = 6meV$ (dash-dotted-dotted black curve). SiO_2 core: $\Delta = 0meV$ (dashed blue curve) and $\Delta = 10meV$ (solid green curve). Here, $h_a = h_b = 3nm$.

In Fig. (4.5), we have investigated the non-Markovian decay dynamics of $|C_b(t)|$ for the QD b initially in its ground state with the presence of the nanoshell modelled with different core materials. The oscillations dynamics is observable even with the significant metal losses. The results in Fig. (4.5) demonstrate the effects of the detuning on the excitation of the QD b and subsequently the coupling of the system. Here, we have set $\omega_a = \omega_b = \omega_c + \Delta$, where ω_c is the SPR.

While for the Au_2S core the QD b excited at earlier times with pronounce oscillations, a small detuning about or may less than $6meV$ result in slowing down the dynamics of the system (dash-dotted-dotted black curve). In contrast, for SiO_2 core the oscillations with two cases (i.e., $\Delta = 0meV$ (dashed blue curve) and $\Delta = 10meV$ (solid green curve)) are identical though the detuning is increased up to $10meV$.

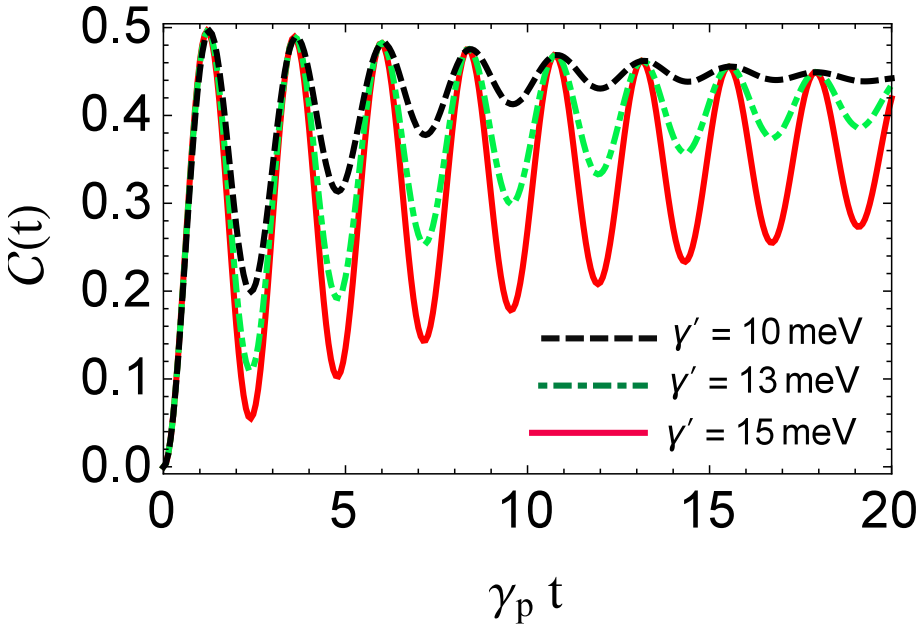

Figure 4.6: The concurrence as a function of normalized time for the case of $s = -1$ with varying the QDs pure dephasing: $\gamma' = 10meV$ (dashed black curve), $\gamma' = 13meV$ (dash-dotted green curve), and $\gamma' = 15meV$ (solid red curve). Here, $h_a = h_b = 3nm$ from the surface of the Au_2S/Ag.

Thus, the dynamics of the system are less dependence on the detuning if the losses are large and show strong sensitivity on the detuning if the losses at the minimum.

In Fig. (4.6), we have looked at the effect of coherent exchange interaction in the presence of QDs pure dephasing. The concurrence shows rich dynamics and the oscillations increased significantly with increasing γ' indicating that the two QDs are effectively coupled through the localized surface plasmon-induced photon exchange. The results in Fig. (4.6) clearly show the robustness of our protocol allow for an on-demand, fast, and almost perfect entanglement even at strong carrier-phonon interaction where other systems fail. In fact, the effectiveness of the presented schemes is shown to be better the stronger the carrier-phonon interaction is.

Shown in Fig. (4.7) is the concurrence dependence on the asymmetry in the QDs

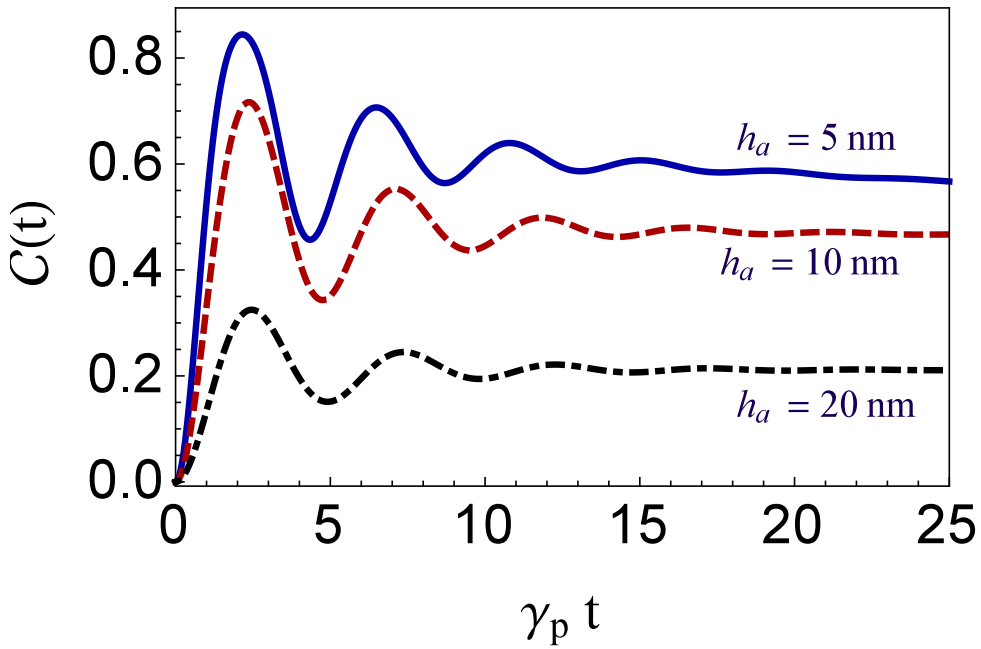

Figure 4.7: The concurrence as a function of normalized time with $s = -1$ for various locations of the QD a from the surface of Au_2S/Ag: $h_a = 5nm$ (solid blue curve), $10nm$ (dashed red curve), and $20nm$ (dash-dotted black curve). Here, $R_2/R_1 = 0.875$ and the QD b is located at $1nm$ from the surface of the nanoshell.

positions with respect to the nanoshell. Here, the QD b is initially in the ground state and situated very close from the surface of the nanoshell (i.e., $h_b = 1nm$) while the location of the initially excited QD a is varied.

While for the perfectly symmetric system shown in Fig. 4, the entanglement oscillates ~ 0.5, which is the maximum amount possible, the results do already considerably change for a slightly different QDs locations: not only does the oscillation amplitude persist, but the system is efficiently coupled, significantly higher entanglement are reached. For $h_b = 5nm$, which turn out to be the optimal choice for the location of QD a, an ideal and robust entanglement is realized with $\mathcal{C}$ taking values of roughly 0.87. It is also found that the asymmetry in the QDs positions with respect to the nanoshell leads to a steady state entanglement existing for a suffi-

ciently long time in contrast to the symmetric case. These features indicate that the QDs-nanoshell interaction enters the strong coupling regime, where the excitation energy is coherently transferred between the QDs and the nanoshell in the form of Rabi oscillation. Eventually, when the QD a is placed at large distances, the system enters a weak coupling regime and subsequently the concurrence attains 0.35 as an optimum value (dash-dotted black curve). This is an exciting and promising result, that can be implemented with today's technology. This may lead to the design of devices at the nanoscale that may be useful for quantum computing community.

The strong sensitivity of the entanglement on the shell thickness is shown in Fig. (4.8). The distances from QD a and QD b from the surface of the Au_2S/Ag nanoshell are $5nm$ and $1nm$, respectively. The transition frequencies of the QDs are set to be resonant with the localized sphere-like plasmon mode for different thicknesses of the shell. As the shell thickness increases, the plasmon resonance exhibits a large spectral shift to the higher frequencies (see the inset in Fig. (4.2a)). Additionally, the linewidths in the spectrum are enlarged significantly showing that the contributions of the interband absorption (the losses in the metal) are magnified. Shown in Fig. 8 the dramatic change in the evolution dynamics of the coupled QDs and subsequently the entanglement by varying the shell thickness although the outer radius is fixed at a certain value, namely $16nm$.

In addition, we have also considered the quantum entanglement in the limit of the refractive index of the Au_2S core n_c and the refractive index of the silver shell $n_m(\omega)$ being equal. This case represents a solid sphere with permittivity $\epsilon_m(\omega, R_1)$ embedded in a homogenous medium with dielectric constant ϵ_b. Here, we have calculated the concurrence for the solid sphere with two different sizes; $R = 16nm$ (dash-dotted-dotted dark green curve) and $R = 5nm$ (dashed pink curve). The results in Fig. (4.8) confirmed that it is unlikely to generate an efficient entanglement

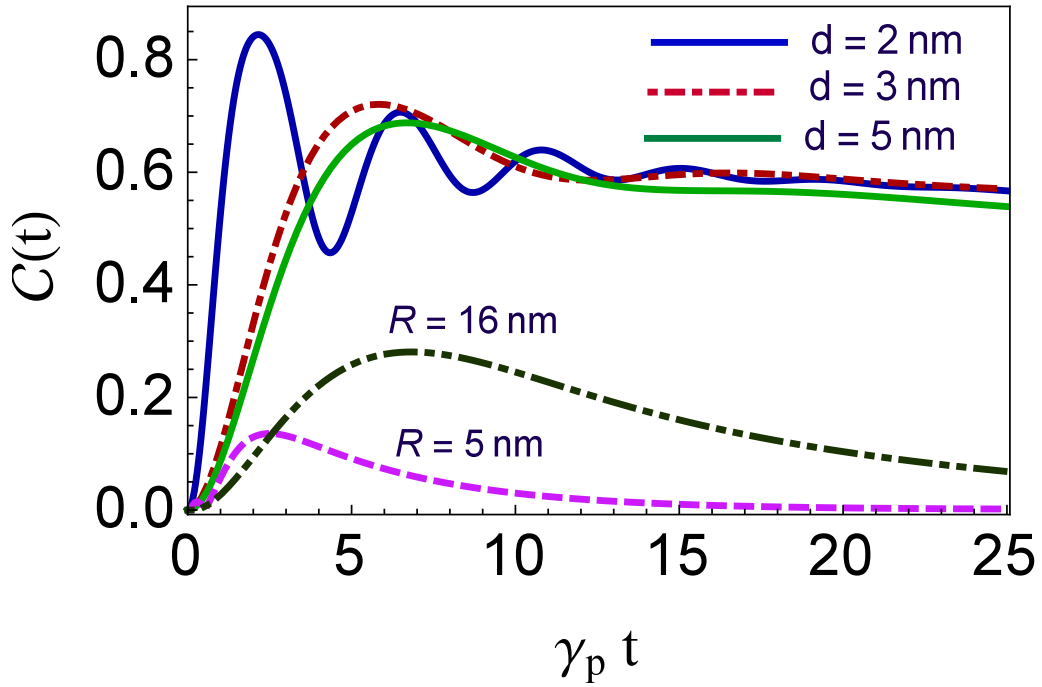

Figure 4.8: The concurrence as a function of normalized time with varying the thickness of the nanoshell: $d = 2nm$ (solid blue curve), $3nm$ (dash-dotted red curve), and $5nm$ (solid green curve). Here, $h_a = 5nm$ and $h_b = 1nm$ from the surface of Au_2S/Ag. For comparison, the concurrence in the limit of the refractive index of the Au_2S core n_c and the refractive index of the silver shell $n_m(\omega)$ being equal is shown with different sizes: $R = 16nm$ (dash-dotted-dotted dark green curve) and $R = 5nm$ (dashed pink curve).

in the vicinity of a solid sphere. Clearly, the realistic parameters that we used in the numerical calculations including the retardation effects and the inherent losses in the nanoparticle as elaborated in Fig. (4.2b) indicate that the application of the nanoshell with a controllable shell thickness as well as the core material is advantageous over a solid sphere for creating pronounce entangled pairs from a one QD excited initial condition.

4.4 Conclusions

We have presented an applicable scheme that allows us to investigate quantum correlations between two single QDs in the proximity of a metal nanoshell. We used a self-consistent photon Green's function technique to explore the quantum optical and entanglement dynamics between two QDs that cover all the coupling regimes. In the vicinity of the nanoshell, the local density of states enhanced immensely, leading to strong coupling regime. The degree of the entanglement characterized by the concurrence can be maximized by optimizing the shell thickness as well as the ratio of the distances between the QDs and the surface of the shell. The loss of the system is greatly reduced even when the QDs are ultra-close to the shell, which signifies slow decay rate of the coherence information and longtime entanglement preservation, which is highly desirable for quantum information science community. In addition, the populations dynamics with solid state QDs are found to have great flexibility in deriving substantial amount of qubit entanglement in many cases and subsequently offer several advantages over coupling identical atoms. Our protocol allow for an on-demand, fast, and almost perfect entanglement even at strong carrier- phonon interaction where other systems fail. We noticed that the realistic parameters that we used including the retardation effects and the inherent losses in the nanoparticle, it is unlikely to generate an efficient entanglement in the vicinity of a solid sphere. There is also the potential to see strong coupling, if one uses MNPs with nonspherical shapes, e.g., cigar shapes [39]. Rapid advances in nanofabrication techniques for plasmonic nanoparticles put such a system within experimental reach.

5. CONCLUSION

In this dissertation, we have reconnoitered several interesting phenomenon and remarkable potential applications of the quantum optical coherence to nano-optics at subwavelength scales in miscellaneous and interesting practical scenarios related to the applications of Casimir force and quantum plasmonics.

Nowadays, with the development of microelectromechanical and nanoelectromechanical systems and nanotechnology, a repulsive Casimir interaction would be advantageous to prevent stiction as well as for frictionless suspension and other applications. Activated by this urgent practical issue in nanoelectromechanical systems and today's micro-devices and the fast development of force detection techniques, experimental and theoretical investigations on these forces between neutral bodies have experienced an extraordinary revitalization in the past few years.

There have been predominantly several mechanisms as a criteria to realize a repulsive Casimir force: (i) two objects characterized by $\epsilon_1(i\xi)$ and $\epsilon_2(i\xi)$ embedded in a fluid satisfy $\epsilon_1(i\xi) < \epsilon_{\text{fluid}}(i\xi) < \epsilon_2(i\xi)$ over a sufficiently wide range of imaginary frequencies, (ii) asymmetric setup with $(\epsilon > \mu)$ and $(\epsilon < \mu)$, and (iii) two objects sandwiching a perfect lens.

In the first part of this work, we have investigated the possibility of realizing a repulsive interaction using optical active chiral metamaterials that respond differently for the left and right circular polarizations. We have proposed for the first time, to our knowledge, a practical scheme studying coherent control of the Casimir force at nanoscale with the possibility of switching between attractive and repulsive forces.

There are many open questions that needs to be addressed. For practical systems, the robustness and strength of chirality coefficients need to be testified within experi-

mental measurements. One future direction would be to perform a thorough detailed theoretical modeling to identify the most suitable and applicable atomic species and experimental system for observing repulsive Casimir force. If achieved, we expect that our technique may have potential applications in nanoelectromecanical (NEMS) devices.

The second part of this work is dedicated to the applications of quantum plasmonics. We have investigated the coherent control of the quantum optical properties of a quantum dot coupled to a metallic nanoparticle applying a photon Greens function method, which is based on the exact quantization of the electromagnetic fields in a dissipative medium. The properties of the spontaneous emission spectra of such a system are studied in detail with and without involving the coherent field. The Rabi splitting effect in the spectrum emitted by the quantum dot under particular conditions is predicted for different sizes of the metal nanoparticles. We show that the spontaneous emission spectra of the transition coupled to surface plasmons may be further modified by adjusting the external coherent control on the adjacent transitions. Furthermore, the pronounced oscillatory behavior for the quantum-dot dynamics is demonstrated with the presence of the metal nanoparticle by the non-Markovian treatment. Our results may have potential applications in plasmonic-based quantum manipulation.

In the third part, we proposed a scheme to create entanglement in a hybrid structure consisting of two quantum bits or quantum emitters in the proximity of multi-layered plasmonic nanostructures (nanoshells). Quantum entanglement and quantum superposition are extraordinary phenomena of quantum mechanics, which have remarkable potential applications in quantum metrology, quantum information and quantum computation [150]. Nanoshells can enhance the local density of states, leading to a strong-coupling regime where the excitation energy can coherently be

transferred between the quantum dots and the nanoshell in the form of Rabi oscillations. The long-lived entangled states can be created deterministically by optimizing the shell thickness as well as the ratio of the distances between the quantum dots and the surface of the shell. The loss of the system is greatly reduced even when the quantum dots are ultraclose to the shell, which signifies a slow decay rate of the coherence information and longtime entanglement preservation. Our protocol allows for an on-demand, fast, and almost perfect entanglement even at strong carrier-phonon interaction where other systems fail.

REFERENCES

[1] A. W. Rodriguez, F. Capasso, and S. G. Johnson, "The casimir effect in microstructured geometries," *Nature*, vol. 5, pp. 211–221, 2011.

[2] A. W. Rodriguez, A. P. McCauley, D. Woolf, F. Capasso, J. D. Joannopoulos, and S. G. Johnson, "Nontouching nanoparticle diclusters bound by repulsive and attractive casimir forces," *Phys. Rev. Lett.*, vol. 104, p. 160402, 2010.

[3] V. A. Parsegian, *Van der Waals Forces. A Handbook for Biologists, Chemists, Engineers, and Physicists.* Cambridge University Press, 2006.

[4] H. B. Chan, V. A. Aksyuk, R. N. Kleiman, D. J. Bishop, and F. Capasso, "Nonlinear micromechanical casimir oscillator," *Phys. Rev. Lett.*, vol. 87, p. 211801, 2001.

[5] A. W. Rodriguez, A. D. W., P. McCauley, F. Capasso, J. D. Joannopoulos, and S. G. Johnson, "Achieving a strongly temperature-dependent casimir effect," *Phys. Rev. Lett.*, vol. 105, p. 060401, 2010.

[6] H. B. G. Casimir, "On the attraction between two perfectly conducting plates," *Proc. K. Ned. Akad. Wet.*, vol. 51, pp. 793–795, 1948.

[7] P. W. Milonni, *The Quantum Vacuum: An Introduction to Quantum Electrodynamics.* Academic, San Diego, 1994.

[8] E. M. Lifshitz, "The theory of molecular attractive forces between solids," *Sov. Phys. JETP*, vol. 2, p. 73, 1956.

[9] S. K. Lamoreaux, "Demonstration of the casimir force in the 0.6 to 6m range," *Phys. Rev. Lett.*, vol. 78, p. 5, 1997.

[10] U. Mohideen and A. Roy, "Precision measurement of the casimir force from 0.1 to 0.9m," *Phys. Rev. Lett.*, vol. 81, p. 4549, 1998.

[11] S. K. Lamoreaux, "The casimir force: Background, experiments, and applications," *Rep. Prog. Phys.*, vol. 68, p. 201, 2005.

[12] M. Bordag, U. Mohideen, G. L. Klimchitskaya, and V. M. Mostepanenko, "New developments in the casimir effect," *Phys. Rep.*, vol. 353, p. 1, 2001.

[13] U. Leonhardt and T. G. Philbin, "Quantum levitation by left-handed metamaterials," *New J. Phys.*, vol. 9, p. 254, 2007.

[14] F. S. S. Rosa, D. A. R. Dalvit, and P. W. Milonni, "Casimir-lifshitz theory and metamaterials," *Phys. Rev. Lett.*, vol. 100, p. 183602, 2008.

[15] F. S. S. Rosa, D. A. R. Dalvit, and P. Milonni, "Casimir interactions for anisotropic magnetodielectric metamaterials," *Phys. Rev. A*, vol. 78, p. 032117, 2008.

[16] Y. Yang, R. Zeng, H. Chen, and M. S. Zubairy, "Controlling the casimir force via the electromagnetic properties of materials," *Phys. Rev. A*, vol. 81, p. 022114, 2010.

[17] T. H. Boyer, "Van der waals forces and zero-point energy for dielectric and permeable materials," *Phys. Rev. A*, vol. 9, p. 2078, 1974.

[18] R. Zhao, J. Zhou, T. Koschny, E. N. Economou, and C. M. Soukoulis, "Repulsive casimir force in chiral metamaterials," *Phys. Rev. Lett.*, vol. 103, p. 103602, 2009.

[19] R. Zhao, J. Zhou, T. Koschny, E. N. Economou, and C. Soukoulis, "Repulsive casimir forces with finite-thickness slabs," *Phys. Rev. B*, vol. 83, p. 075108, 2011.

[20] M. G. Silveirinha and S. I. Maslovski, "Comment on repulsive casimir force in chiral metamaterials," *Phys. Rev. Lett.*, vol. 105, p. 189301, 2010.

[21] R. J. Thompson, G. Rempe, and H. J. Kimble, "Observation of normal-mode splitting for an atom in an optical cavity," *Phys. Rev. Lett.*, vol. 68, p. 1132, 1992.

[22] M. Brune, F. Schmidt-Kaler, A. Maali, J. Dreyer, E. Hagley, J. M. Raimond, and S. Haroche, "Quantum rabi oscillation: A direct test of field quantization in a cavity," *Phys. Rev. Lett.*, vol. 76, p. 1800, 1996.

[23] D. E. Chang, A. S. Sorensen, P. R. Hemmer, and M. D. Lukin, "Quantum optics with surface plasmons," *Phys. Rev. Lett.*, vol. 97, p. 053002, 2006.

[24] D. E. Chang, A. S. Sorensen, E. A. Demler, and M. D. Lukin, "A single-photon transistor using nanoscale surface plasmons," *Nature*, vol. 3, p. 807, 2007.

[25] C. J. Powell and J. B. Swan, "Origin of the characteristic electron energy losses in aluminum," *Phys. Rev.*, vol. 115, p. 869, 1959.

[26] D. Bouchet, D. Cao, R. Carminati, Y. D. Wilde, and V. Krachmalnicoff, "Long-range plasmon-assisted energy transfer between fluorescent emitters," *Phys. Rev. Lett.*, vol. 116, p. 037401, 2016.

[27] V. N. Pustovit and T. V. Shahbazyan, "Cooperative emission of light by an ensemble of dipoles near a metal nanoparticle: The plasmonic dicke effect," *Phys. Rev. Lett.*, vol. 102, p. 077401, 2009.

[28] M. Russ and G. Burkard, "Long distance coupling of resonant exchange qubits," *Phys. Rev. B*, vol. 92, p. 205412, 2015.

[29] V. N. Pustovit and T. V. Shahbazyan, "Plasmon-mediated superradiance near metal nanostructures," *Phys. Rev. B*, vol. 82, p. 075429, 2010.

[30] D. J. Bergman and M. I. Stockman, "Surface plasmon amplification by stimulated emission of radiation: Quantum generation of coherent surface plasmons in nanosystems," *Phys. Rev. Lett.*, vol. 90, p. 027402, 2003.

[31] M. I. Stockman, "Spasers explained," *Nature*, vol. 2, pp. 327–329, 2008.

[32] R. Ruppin, "Decay of an excited molecule near a small metal sphere," *J. Chem. Phys.*, vol. 76, p. 1681, 1982.

[33] G. S. Agarwal and S. V. ONeil, "Effect of hydrodynamic dispersion of the metal on surface plasmons and surface-enhanced phenomena in spherical geometries," *Phys. Rev. B*, vol. 28, p. 487, 1983.

[34] G. W. Ford and W. H. Weber, "Electromagnetic interactions of molecules with metal surfaces," *Phys. Rep.*, vol. 113, p. 195, 1984.

[35] X. Y. Huang, K. T. Lee, and T. F. George, "Resonance fluorescence of a two-level atom near a rough metal surface," *J. Chem. Phys.*, vol. 85, p. 567, 1986.

[36] A. O. Govorov, G. W. Bryant, W. Zhang, T. Skeini, J. Lee, N. A. Kotov, J. M. Slocik, and P. R. Naik, "Exciton-plasmon interaction and hybrid excitons in semiconductor-metal nanoparticle assemblies," *Nano Lett.*, vol. 6, p. 984, 2006.

[37] G. C. des Francs, C. Girard, T. Laroche, G. Leveque, and O. J. F. Martin, "Theory of molecular excitation and relaxation near a plasmonic device," *J. Chem. Phys.*, vol. 127, p. 034701, 2007.

[38] G. Y. Chen, Y. N. Chen, D. S. Chuu, and T. Brandes, "Quantum-dot exciton dynamics with a surface plasmon: Band-edge quantum optics," *Phys. Rev. A*, vol. 79, p. 033815, 2009.

[39] A. Trügler and U. Hohenester, "Strong coupling between a metallic nanoparticle and a single molecule," *Phys. Rev. B*, vol. 77, p. 115403, 2008.

[40] Y. Gu, L. J. Wang, P. Ren, J. X. Zhang, T. C. Zhang, O. J. F. Martin, and Q. Gong, "Surface-plasmon-induced modification on the spontaneous emission spectrum via subwavelength-confined anisotropic purcell factor," *Nano Lett.*, vol. 12, p. 2488, 2012.

[41] R. Marty, A. Arbouet, V. Paillard, C. Girard, and G. C. des Francs, "Photon antibunching in the optical near field," *Phys. Rev. B*, vol. 82, p. 081403, 2010.

[42] A. Gonzalez-Tudela, F. J. Rodríguez, L. Quiroga, and C. Tejedor, "Dissipative dynamics of a solid-state qubit coupled to surface plasmons: From non-markov to markov regimes," *Phys. Rev. B*, vol. 82, p. 115334, 2010.

[43] D. Dzsotjan, A. S. Sorensen, and M. Fleischhauer, "Quantum emitters coupled to surface plasmons of a nanowire: A greens function approach," *Phys. Rev. B*, vol. 82, p. 075427, 2010.

[44] P. Anger, P. Bharadwaj, and L. Novotny, "Enhancement and quenching of single-molecule fluorescence," *Phys. Rev. Lett.*, vol. 96, p. 113002, 2006.

[45] S. Kuhn, U. Hakanson, L. Rogobete, and V. Sandoghdar, "Enhancement of single-molecule fluorescence using a gold nanoparticle as an optical nanoantenna," *Phys. Rev. Lett.*, vol. 97, p. 017402, 2006.

[46] S. Schietinger, M. Barth, T. Alchele, and O. Benson, "Plasmon-enhanced single photon emission from a nanoassembled metal-diamond hybrid structure at room temperature," *Nano Lett.*, vol. 9, p. 1694, 2009.

[47] K. T. Shimizu, W. K. Woo, B. R. Fisher, H. J. Eisler, and M. G. Bawendi, "Surface-enhanced emission from single semiconductor nanocrystals," *Phys. Rev. Lett.*, vol. 89, p. 117401, 2002.

[48] D. Ratchford, F. Shafiei, S. Kim, S. K. Gray, and X. Li, "Manipulating coupling between a single semiconductor quantum dot and single gold nanoparticle," *Nano Lett.*, vol. 11, p. 1049, 2011.

[49] A. Gonzalez-Tudela, D. Martin-Cano, E. Moreno, L. Martin-Moreno, C. Tejedor, and F. J. Garcia-Vidal1, "Entanglement of two qubits mediated by one-dimensional plasmonic waveguides," *Phys. Rev. Lett.*, vol. 106, p. 020501, 2011.

[50] D. Kim, S. G. Carter, A. Greilich, A. S. Bracker, and D. Gammon, "Ultrafast optical control of entanglement between two quantum-dot spins," *Nature*, vol. 7, p. 223, 2011.

[51] X. Li, Y. Wu, D. Steel, D. Gammon, T. H. Stievater, D. S. Katzer, D. Park, C. Piermarocchi, and L. J. Shamn, "An all-optical quantum gate in a semiconductor quantum dot," *Science*, vol. 301, p. 809, 2003.

[52] S. Hughes, "Modified spontaneous emission and qubit entanglement from dipole-coupled quantum dots in a photonic crystal nanocavity," *Phys. Rev. Lett.*, vol. 94, p. 227402, 2005.

[53] L. A. Webster, K. Truex, L.-M. Duan, D. G. Steel, A. S. Bracker, D. Gammon, and L. J. Sham, "Coherent control to prepare an inas quantum dot for spin-photon entanglement," *Phys. Rev. Lett.*, vol. 112, p. 126801, 2014.

[54] M. L. Andersen, S. Stobbe, A. S. Sørensen, and P. Lodahl, "Strongly modified plasmon-matter interaction with mesoscopic quantum emitters," *Nature*, vol. 7, p. 215, 2011.

[55] E. Prodan, C. Radloff, N. J. Halas, and P. Nordlander, "A hybridization model for the plasmon response of complex nanostructures," *Science*, vol. 302, p. 419, 2003.

[56] S. A. Maier, *Plasmonics: Fundamental and Applications.* Springer, New York, 2007.

[57] H. A. Atwate, "The promise of plasmonics," *Sci. Am.*, vol. 17, p. 56, 2007.

[58] I. E. Dzyaloshinskii, E. M. Lifshitz, and L. P. Pitaevskii, "The general theory of van der waals forces," *Adv. Phys.*, vol. 10, p. 165, 1961.

[59] F. Zhou and L. Spruch, "Van der waals and retardation (casimir) interactions of an electron or an atom with multilayered walls," *Phys. Rev. A*, vol. 52, p. 297, 1995.

[60] N. van Kampen, B. Nijboer, and K. Schram, "On the macroscopic theory of van der waals forces," *Phys. Lett.*, vol. 26A, p. 307, 1968.

[61] B. W. Ninham, V. A. Parsegian, and G. H. Weiss, "On the macroscopic theory of temperature-dependent van der waals forces," *J. Stat. Phys.*, vol. 2, p. 323, 1970.

[62] M. S. Tomaš, "Casimir force in absorbing multilayers," *Phys. Rev. A*, vol. 66, p. 052103, 2002.

[63] G. L. Klimchitskaya, U. Mohideen, and V. M. Mostepanenko, "Casimir and van der waals forces between two plates or a sphere lens above a plate made of real metals," *Phys. Rev. A*, vol. 61, p. 062107, 2000.

[64] A. Lambrecht, P. A. M. Neto, and S. Reynaud, "The casimir effect within scattering theory," *New J. Phys.*, vol. 8, p. 243, 2006.

[65] C. Raabe, L. Knöll, and D. G. Welsch, "Three-dimensional casimir force between absorbing multilayer dielectrics," *Phys. Rev. A*, vol. 68, p. 033810, 2003.

[66] J. Kästel, M. Fleischhauer, S. F. Yelin, and R. L. Walsworth, "Low-loss negative refraction by laser-induced magnetoelectric cross coupling," *Phys. Rev. A*, vol. 79, p. 063818, 2009.

[67] J. Kästel, M. Fleischhauer, S. F. Yelin, and R. Walsworth, "Tunable negative refraction without absorption via electromagnetically induced chirality," *Phys. Rev. Lett.*, vol. 99, p. 073602, 2007.

[68] H. Zhang, Y. Niu, H. Sun, J. Luo, and S. Gong, "Phase control of switching from positive to negative index material in a four-level atomic system," *J. Phys. B: At. Mol. Opt. Phys.*, vol. 41, p. 125503, 2008.

[69] J. B. Pendry, "A chiral route to negative refraction," *Science*, vol. 306, p. 1353, 2004.

[70] B. Wang, J. Zhou, T. Koschny, M. Kafesaki, and C. M. Soukoulis, "Chiral metamaterials: Simulations and experiments," *J. Opt. A: Pure Appl. Opt.*, vol. 11, p. 114003, 2009.

[71] C. Monzon and D. W. Forester, "Negative refraction and focusing of circularly polarized waves in optically active media," *Phys. Rev. Lett.*, vol. 95, p. 123904, 2005.

[72] C. F. Bohren, "Light scattering by an optically active sphere," *Chem. Phys. Lett.*, vol. 29, p. 458, 1974.

[73] A. Lakhtakia, V. V. Varadan, and V. K. Varadan, "What happens to plane waves at the planar interfaces of mirror-conjugated chiral media," *J. Opt. Soc. Am. A*, vol. 6, p. 23, 1989.

[74] A. Lakhtakia, *Time-Harmonic Electromagnetic Fields in Chiral Media*. Berlin: Springer, 1989.

[75] A. Lakhtakia, V. V. Varadan, and V. K. Varadan, "Reflection of plane waves at planar achiral-chiral interfaces: Independence of the reflected polarization state from the incident polarization state," *J. Opt. Soc. Am. A*, vol. 7, p. 1654, 1990.

[76] I. V. Lindell, A. H. Sihvola, S. A. Tretyakov, and A. J. Viitanen, *Electromagnetic Waves in Chiral and Bi-Isotropic Media*. Artech House, Boston, London, 1994.

[77] J. Hakami and M. S. Zubairy, "Coherent control of casimir force in a chiral medium," *J. Phys. B: At. Mol. Opt. Phys.*, vol. 45, p. 205502, 2012.

[78] M. O. Scully and M. S. Zubairy, *Quantum Optics*. Cambridge: Cambridge University Press, 1997.

[79] F. li Li, A. ping Fang, and M. Wang, "Electromagnetic chirality-induced negative refraction via atomic coherence," *J. Phys. B: At. Mol. Opt. Phys.*, vol. 42, p. 195505, 2009.

[80] J. Kästel and M. Fleischhauer, "Comment on electromagnetically induced left handedness in optically excited four-level atomic media," *Phys. Rev. Lett.*, vol. 98, p. 069301, 2007.

[81] D. E. Sikes and D. Yavuz, "Negative refraction with low absorption using raman transitions with magnetoelectric coupling," *Phys. Rev. A*, vol. 82, p. 011806(R), 2010.

[82] D. E. Sikes and D. D. Yavuz, "Negative refraction using raman transitions and chirality," *Phys. Rev. A*, vol. 84, p. 053836, 2011.

[83] C. E. Pryor and M. E. Flatté, "Landé g factors and orbital momentum quenching in semiconductor quantum dots," *Phys. Rev. Lett.*, vol. 96, p. 026804, 2006.

[84] V. A. Dzuba, V. V. Flambaum, and B. L. Lev, "Dynamic polarizabilities and magic wavelengths for dysprosium," *Phys. Rev. A*, vol. 83, p. 032502, 2011.

[85] M. Lu, S. Youn, and B. L. Lev, "Spectroscopy of a narrow-line laser-cooling transition in atomic dysprosium," *Phys. Rev. A*, vol. 83, p. 012510, 2011.

[86] M. Lu, S. H. Youn, and B. L. Lev, "Trapping ultracold dysprosium: A highly magnetic gas for dipolar physics," *Phys. Rev. Lett.*, vol. 104, p. 063001, 2010.

[87] C. I. Hancox, S. C. Doret, M. T. Hummon, L. Luo, and J. M. Doyle, "Magnetic trapping of rare-earth atoms at millikelvin temperatures," *Nature*, vol. 431, p. 281, 2004.

[88] V. Yannopapas, E. Paspalakis, and N. V. Vitanov, "Plasmon-induced enhancement of quantum interference near metallic nanostructures," *Phys. Rev. Lett.*, vol. 103, p. 063602, 2009.

[89] V. Yannopapas and N. V. Vitanov, "Spontaneous emission of a two-level atom placed within clusters of metallic nanoparticles," *J. Phys. Condens. Matter*, vol. 19, p. 096210, 2007.

[90] X. D. Zeng, J. P. Xu, and Y. P. Yang, "Spontaneous emission interference enhancement with a μ-negative metamaterial slab," *Phys. Rev. A*, vol. 84, p. 033834, 2011.

[91] J. R. Lakowicz, "Plasmonics in biology and plasmon-controlled fluorescence," *Plasmonics*, vol. 1, p. 5, 2006.

[92] A. Ridolfo, O. D. Stefano, N. Fina, R. Saija, and S. Savasta, "Quantum plasmonics with quantum dot-metal nanoparticle molecules: Influence of the fano effect on photon statistics," *Phys. Rev. Lett.*, vol. 105, p. 263601, 2010.

[93] Y. Gu, L. Huang, O. J. F. Martin, and Q. Gong, "Resonance fluorescence of single molecules assisted by a plasmonic structure," *Phys. Rev. B*, vol. 81, p. 193103, 2010.

[94] A. V. Akimov, A. Mukherjee, C. L. Yu, D. E. Chang, A. S. Zibrov, H. P. P. R. Hemmer, and M. D. Lukin, "Generation of single optical plasmons in metallic nanowires coupled to quantum dots," *Nature*, vol. 450, p. 402, 2007.

[95] C. Genet and T. W. Ebbesen, "Light in tiny holes," *Nature*, vol. 445, p. 39, 2007.

[96] H. Ditlbacher, A. Hohenau, D. Wagner, U. Kreibig, M. Rogers, F. Hofer, F. R. Aussenegg, and J. R. Krenna, "Silver nanowires as surface plasmon resonators," *Phys. Rev. Lett.*, vol. 95, p. 257403, 2005.

[97] S. Evangelo, V. Yannopapas, and E. Paspalakis, "Modifying free-space spontaneous emission near a plasmonic nanostructure," *Phys. Rev. A*, vol. 83, p. 023819, 2011.

[98] C. V. Vlack, P. T. Kristensen, and S. Hughes, "Spontaneous emission spectra and quantum light-matter interactions from a strongly coupled quantum dot metal-nanoparticle system," *Phys. Rev. B*, vol. 85, p. 075303, 2012.

[99] J. D. Cox, M. R. Singh, G. Gumbs, M. A. Anton, and F. Carreno, "Dipole-dipole interaction between a quantum dot and a graphene nanodisk," *Phys. Rev. B*, vol. 86, p. 125452, 2012.

[100] M. A. Antn, F. Carreo, S. Melle, O. G. Caldern, E. Cabrera-Granado, J. Cox, and M. R. Singh, "Plasmonic effects in excitonic population transfer in a driven semiconductormetal nanoparticle hybrid system," *Phys. Rev. B*, vol. 86, p. 155305, 2012.

[101] J. Hakami, L. Wang, and M. S. Zubairy, "Spectral properties of a strongly coupled quantum-dotmetal-nanoparticle system," *Phys. Rev. A*, vol. 89, p. 053835, 2014.

[102] M. V. G. Dutt, J. Cheng, B. Li, X. Xu, X. Li, P. R. Berman, D. G. Steel, A. S. Bracker, D. Gammon, S. E. Economou, R.-B. Liu, and L. J. Sham, "Stimulated and spontaneous optical generation of electron spin coherence in charged gaas quantum dots," *Phys. Rev. Lett.*, vol. 94, p. 227403, 2005.

[103] X. Xu, B. Sun, P. R. Berman, D. G. Steel, A. S. Bracker, D. Gammon, and L. J. Sham, "Coherent population trapping of an electron spin in a single negatively charged quantum dot," *Nature*, vol. 4, p. 692, 2008.

[104] J. M. Elzerman, K. M. Weiss, J. Miguel-Sanchez, and A. Imamoglu, "Optical amplification using raman transitions between spin-singlet and spin-triplet states of a pair of coupled in-gaas quantum dots," *Phys. Rev. Lett.*, vol. 107, p. 017401, 2011.

[105] M. Bamba and H. Ishihara, "Qed of excitons with nonlocal susceptibility in arbitrarily structured dielectrics," *Phys. Rev. B*, vol. 78, p. 085109, 2008.

[106] K. Cho, *Optical Response of Nanostructures.* Springer-Verlag, Berlin, 2003.

[107] T. Torimoto, H. Horibe, T. Kameyama, K. Okazaki, S. Ikeda, M. Matsumura, A. Ishikawa, and H. Ishihara, "Plasmon-enhanced photocatalytic activity of cadmium sulfide nanoparticle immobilized on silica-coated gold particles," *J. Phys. Chem. Lett.*, vol. 2, p. 2057, 2011.

[108] A. Ishikawa, K. Osono, A. Nobuhiro, Y. Mizumoto, T. Torimoto, and H. Ishihara, "Theory for self-consistent interplay between light and nanomaterials

strongly modified by metallic nanostructures," *Phys. Chem. Chem. Phys.*, vol. 15, p. 4214, 2013.

[109] H. T. Dung, S. Y. Buhmann, L. Knll, D.-G. Welsch, S. Scheel, and J. Kstel, "Electromagnetic-field quantization and spontaneous decay in left-handed media," *Phys. Rev. A*, vol. 68, p. 043816, 2003.

[110] X. Xu, B. Sun, P. R. Berman, D. G. Steel, A. S. Bracker, D. Gammon, and L. J. Sham, "Coherent optical spectroscopy of a strongly driven quantum dot," *Science*, vol. 317, p. 929, 2007.

[111] R. Carminati, J.-J. Greffet, C. Henkel, and J. M. Vigoureux, "Radiative and non-radiative decay of a single molecule close to a metallic nanoparticle," *Opt. Commun.*, vol. 261, p. 368, 2006.

[112] L. Novotny and B. Hecht, *Principles of Nano-optics*. Cambridge University Press, Cambridge, UK, 2012.

[113] J.-J. Greffet, M. Laroche, and F. Marquier, "Impedance of a nanoantenna and a single quantum emitter," *Phys. Rev. Lett.*, vol. 105, p. 117701, 2010.

[114] P. B. Johnson and R. W. Christy, "Optical constants of the noble metals," *Phys. Rev. B*, vol. 6, p. 4370, 1972.

[115] W. H. Press, S. A. Teukolsky, W. T. Vetterling, and B. P. Flanery, *Numerical Recipes in FORTRAN: The Art of Scientific Computing*. Cambridge University Press, Cambridge, 1992.

[116] H. T. Dung, L. Knll, and D.-G. Welsch, "Spontaneous decay in the presence of dispersing and absorbing bodies: General theory and application to a spherical cavity," *Phys. Rev. A*, vol. 62, p. 053804, 2000.

[117] F. Alpeggiani, S. D'Agostino, and L. C. Andreani, "Surface plasmons and strong light-matter coupling in metallic nanoshells," *Phys. Rev. B*, vol. 86, p. 035421, 2012.

[118] S. Savasta, R. Saija, A. Ridolfo, O. D. Stefano, P. Denti, and F. Borghese, "Nanopolaritons: Vacuum rabi splitting with a single quantum dot in the center of a dimer nanoantenna," *ACS Nano*, vol. 4, p. 6369, 2010.

[119] H. Qiao, K. A. Abel, F. C. J. M. van Veggel, and J. F. Young, "Exciton thermalization and state broadening contributions to the photoluminescence of colloidal pbse quantum dot films from 295 to 4.5 k," *Phys. Rev. B*, vol. 82, p. 165435, 2010.

[120] E. Dulkeith, A. C. Morteani, T. Niedereichholz, T. A. Klar, J. Feldmann, S. A. Levi, F. C. J. M. van Veggel, D. N. Reinhoudt, M. Mller, and D. I. Gittins, "Fluorescence quenching of dye molecules near gold nanoparticles: Radiative and nonradiative effects," *Phys. Rev. Lett.*, vol. 89, p. 203002, 2002.

[121] G. Baffou, C. Girard, E. Dujardin, G. C. des Francs, and O. J. F. Martin, "Molecular quenching and relaxation in a plasmonic tunable system," *Phys. Rev. B*, vol. 77, p. 121101(R), 2008.

[122] G. Sun, J. B. Khurgin, and R. A. Soref, "Practical enhancement of photoluminescence by metal nanoparticles," *Appl. Phys. Lett.*, vol. 94, p. 101103, 2009.

[123] K. E. Dorfman, P. K. Jha, D. V. Voronine, P. Genevet, F. Capasso, and M. O. Scully, "Quantum-coherence-enhanced surface plasmon amplification by stimulated emission of radiation," *Phys. Rev. Lett.*, vol. 111, p. 043601, 2013.

[124] M. J. Mendes, E. Hernández, E. López, P. García-Linares, I. Ramiro, I. Artacho, E. Antolín, I. Tobías, A. Martí, and A. Luque, "Self-organized colloidal quantum dots and metal nanoparticles for plasmon-enhanced intermediate-band solar cells," *Nanotechnology*, vol. 24, p. 345402, 2013.

[125] M. Gullans, T. G. Tiecke, D. E. Chang, J. Feist, J. D. Thompson, J. I. Cirac, P. Zoller, and M. D. Lukin, "Nanoplasmonic lattices for ultracold atoms," *Phys. Rev. Lett.*, vol. 109, p. 235309, 2012.

[126] D. E. Chang, J. D. Thompson, H. Park, V. Vuletić, A. S. Zibrov, P. Zoller, and M. D. Lukin, "Trapping and manipulation of isolated atoms using nanoscale plasmonic structures," *Phys. Rev. Lett.*, vol. 103, p. 123004, 2009.

[127] A. Delga, J. Feist, J. Bravo-Abad, and F. J. Garcia-Vidal, "Quantum emitters near a metal nanoparticle: Strong coupling and quenching," *Phys. Rev. Lett.*, vol. 112, p. 253601, 2014.

[128] Y. He and K.-D. Zhu, "Strong coupling among semiconductor quantum dots induced by a metal nanoparticle," *Nano. Res. Lett.*, vol. 7, p. 95, 2012.

[129] K. V. Nerkararyan and S. I. Bozhevolnyi, "Entanglement of two qubits mediated by a localized surface plasmon," *Phys. Rev. B*, vol. 92, p. 045410, 2015.

[130] J. Hakami and M. S. Zubair, "Nanoshell-mediated robust entanglement between coupled quantum dots," *Phys. Rev. A*, vol. 93, p. 022320, 2016.

[131] R. D. Averitt, D. Sarkar, and N. J. Halas, "Plasmon resonance shifts of au-coated au2s nanoshells: Insight into multicomponent nanoparticle growth," *Phys. Rev. Lett.*, vol. 78, p. 4217, 1997.

[132] A. Zrenner, E. Beham, S. Stufler, F. Findeis, M. Bichler, and G. Abstreiter, "Coherent properties of a two-level system based on a quantum-dot photodi-

ode," *Nature*, vol. 418, p. 612, 2002.

[133] E. B. Flagg, A. Muller, J. W. Robertson, S. Founta, D. G. Deppe, M. Xiao, W. Ma, G. J. Salamo, and C. K. Shih, "Resonantly driven coherent oscillations in a solid-state quantum emitter," *Nature*, vol. 5, p. 203, 2009.

[134] D. Gammon and D. G. Steel, "Optical studies of single quantum dots," *Phys. Today*, vol. 55(10), p. 36, 2002.

[135] T. Yoshie, A. Scherer, J. Hendrickson, G. Khitrova, H. M. Gibbs, G. Rupper, C. Ell, O. B. Shchekin, and D. G. Deppe, "Vacuum rabi splitting with a single quantum dot in a photonic crystal nanocavity," *Nature*, vol. 432, p. 200, 2004.

[136] J. M. Villas-Bôas, S. E. Ulloa, and A. O. Govorov, "Decoherence of rabi oscillations in a single quantum dot," *Phys. Rev. Lett.*, vol. 94, p. 057404, 2005.

[137] U. Kreibig and M. Vollmer, *Optical Properties of Metal Clusters*. Springer, Berlin, 1995.

[138] J. A. Scholl, S. Stobbe, A. L. Koh, and J. A. Dionne, "Quantum plasmon resonances of individual metallic nanoparticles," *Nature*, vol. 483, p. 421, 2012.

[139] K. J. Ahn and A. Knorr, "Radiative lifetime of quantum confined excitons near interfaces," *Phys. Rev. B*, vol. 68, p. 161307(R), 2003.

[140] S. Stobbe, P. T. Kristensen, J. E. Mortensen, J. M. Hvam, J. Mørk, and P. Lodahl, "Spontaneous emission from large quantum dots in nanostructures: Exciton-photon interaction beyond the dipole approximation," *Phys. Rev. B*, vol. 86, p. 085304, 2012.

[141] J. R. Zurita-Sánchez and L. Novotny, "Multipolar interband absorption in a semiconductor quantum dot. i. electric quadrupole enhancement," *J. Opt. Soc. Am. B*, vol. 19, p. 1355, 2002.

[142] P. T. Kristensen, J. E. Mortensen, P. Lodahl, and S. Stobbe, "Shell theorem for spontaneous emission," *Phys. Rev. B*, vol. 88, p. 205308, 2013.

[143] R. S. Savelev, A. P. Slobozhanyuk, A. E. Miroshnichenko, Y. S. Kivshar, and P. A. Belov, "Subwavelength waveguides composed of dielectric nanoparticles," *Phys. Rev. B*, vol. 89, p. 035435, 2014.

[144] M. A. Noginov, G. Zhu, A. M. Belgrave, R. Bakker, V. M. Shalaev, E. E. Narimanov, S. Stout, E. Herz, T. Suteewong, and U. Wiesner, "Demonstration of a spaser-based nanolaser," *Nature*, vol. 460, p. 1110, 2009.

[145] K. T. Butler, P. E. Vullum, A. M. Muggerud, E. Cabrera, and J. H. Harding, "Structural and electronic properties of silver/silicon interfaces and implications for solar cell performance," *Phys. Rev. B*, vol. 83, p. 235307, 2011.

[146] R. Bardhan, N. K. Grady, T. Ali, and N. J. Halas, "Metallic nanoshells with semiconductor cores: Optical characteristics modified by core medium properties," *ACS Nano*, vol. 4 (10), p. 6169, 2010.

[147] T. Unold, K. Mueller, C. Lienau, T. Elsaesser, and A. D. Wieck, "Optical control of excitons in a pair of quantum dots coupled by the dipole-dipole interaction," *Phys. Rev. Lett.*, vol. 94, p. 137404, 2005.

[148] S. Weiler, A. Ulhaq, S. M. Ulrich, D. Richter, M. Jetter, C. R. P. Michler, and S. Hughes, "Phonon-assisted incoherent excitation of a quantum dot and its emission properties," *Phys. Rev. B*, vol. 86, p. 241304(R), 2012.

[149] W. K. Wootters, "Entanglement of formation of an arbitrary state of two qubits," *Phys. Rev. Lett.*, vol. 80, p. 2245, 1998.

[150] M. A. Nielsen and I. L. Chuang, *Quantum Computation and Quantum Information*. Cambridge University Press, 2010.

[151] L. W. Li, P. S. Kooi, M. S. Leong, and T. S. Yeo, "Electromagnetic dyadic green's function in spherically multilayered media," *IEEE Trans. Microwave Theory Tech.*, vol. 42, p. 2302, 1994.

[152] C.-T. Tai, *Dyadic Green Functions in Electromagnetic Theory.* IEEE Press, New York, 1994.

[153] G. N. Watson, *A Treatise on the Theory of Bessel Functions.* Cambridge University Press, Cambridge, 1944.

[154] A. Sommerfeld, *Partial Differential Equations.* Academic Press, New York, 1949.

APPENDIX A

DERIVATION OF CASIMIR FORCE BETWEEN ABSORBING MULTILAYERS: THE STRESS TENSOR METHOD

The derivation of the Casimir force in absorbing multilayer dielectric plates at finite temperatures, which may be regarded as being a generalization of the Lifshitz formula, that gives the force acting on two semi-infinite absorbing dielectric walls, to multilayer systems [62, 65]. Consider a multilayered system described by the dielectric function $\epsilon(\boldsymbol{r},\omega) = \epsilon'(\boldsymbol{r},\omega) + i\epsilon''(\boldsymbol{r},\omega)$ defined in a stepwise fashion, the force on a stack of layers that separates a jth and an lth layer can be calculated from the stress tensor given by

$$\boldsymbol{T}(\boldsymbol{r},\boldsymbol{r}',t) = \boldsymbol{T}_1(\boldsymbol{r},\boldsymbol{r}',t) + \boldsymbol{T}_2(\boldsymbol{r},\boldsymbol{r}',t) - \frac{1}{2}\boldsymbol{I}\mathrm{Tr}\left[\boldsymbol{T}_1(\boldsymbol{r},\boldsymbol{r}',t) + \boldsymbol{T}_2(\boldsymbol{r},\boldsymbol{r}',t)\right], \tag{A.1}$$

where

$$\boldsymbol{T}_1(\boldsymbol{r},\boldsymbol{r}',t) = \left\langle \hat{\boldsymbol{D}}(\boldsymbol{r},t) \otimes \hat{\boldsymbol{E}}(\boldsymbol{r}',t) \right\rangle, \tag{A.2}$$

and

$$\boldsymbol{T}_2(\boldsymbol{r},\boldsymbol{r}',t) = \left\langle \hat{\boldsymbol{B}}(\boldsymbol{r},t) \otimes \hat{\boldsymbol{H}}(\boldsymbol{r}',t) \right\rangle. \tag{A.3}$$

Here, $\hat{\boldsymbol{E}}(\boldsymbol{r})$, $\hat{\boldsymbol{D}}(\boldsymbol{r})$, $\hat{\boldsymbol{B}}(\boldsymbol{r})$, and $\hat{\boldsymbol{H}}(\boldsymbol{r})$ are the medium-assisted (macroscopic) electromagnetic field operators, which decomposed into their annihilation and creation components according to

$$\hat{\boldsymbol{E}}(\boldsymbol{r},t) = \int_0^\infty d\omega \hat{\boldsymbol{E}}(\boldsymbol{r},\omega)e^{-i\omega t} + \mathrm{H.c.}, \tag{A.4}$$

and $\hat{\boldsymbol{D}}(\boldsymbol{r})$, $\hat{\boldsymbol{B}}(\boldsymbol{r})$, and $\hat{\boldsymbol{H}}(\boldsymbol{r})$ accordingly. The constitutive relations

$$\hat{\boldsymbol{D}}(\boldsymbol{r},\omega) = \epsilon_0\epsilon(\boldsymbol{r},\omega)\hat{\boldsymbol{E}}(\boldsymbol{r},\omega) + \hat{\boldsymbol{P}}_{\boldsymbol{N}}(\boldsymbol{r},\omega),$$

$$\hat{\boldsymbol{H}}(\boldsymbol{r},\omega) = \mu_0^{-1}\hat{\boldsymbol{B}}(\boldsymbol{r},\omega), \tag{A.5}$$

satisfy the Maxwell equations and the Kramers-Kronig relations. The noise polarization operator

$$\hat{\boldsymbol{P}}_{\boldsymbol{N}}(\boldsymbol{r},\omega) = i\sqrt{\hbar\epsilon_0\epsilon''(\boldsymbol{r},\omega)/\pi}\hat{\boldsymbol{f}}(\boldsymbol{r},\omega) \tag{A.6}$$

associated with the dissipation in the system is expressed in terms of bosonic fields $\hat{\boldsymbol{f}}(\boldsymbol{r},\omega)$ and $\hat{\boldsymbol{f}}^{\dagger}(\boldsymbol{r},\omega)$,

$$\left[\hat{\boldsymbol{f}}_i(\boldsymbol{r},\omega), \hat{\boldsymbol{f}}_j(\boldsymbol{r}',\omega')\right] = 0,$$

$$\left[\hat{\boldsymbol{f}}_i(\boldsymbol{r},\omega), \hat{\boldsymbol{f}}_j^{\dagger}(\boldsymbol{r}',\omega')\right] = \delta_{ij}\delta(\boldsymbol{r},\boldsymbol{r}')\delta(\omega,\omega'). \tag{A.7}$$

From Maxwell equations and equations (A.5) – (A.7) it then follows that

$$\hat{\boldsymbol{B}}(\boldsymbol{r},\omega) = (i\omega)^{-1}\boldsymbol{\nabla}\times\hat{\boldsymbol{E}}(\boldsymbol{r},\omega),$$

$$\hat{\boldsymbol{D}}(\boldsymbol{r},\omega) = (\mu_0\omega^2)^{-1}\nabla\times\nabla\times\hat{\boldsymbol{B}}(\boldsymbol{r},\omega), \tag{A.8}$$

where $\hat{\boldsymbol{E}}(\boldsymbol{r},\omega)$ is determined via the classical Green tensor satisfying

$$\left[\nabla\times\nabla\times -\epsilon''(\boldsymbol{r},\omega)\frac{\omega^2}{c^2}\mathbf{I}\right]\boldsymbol{G}(\boldsymbol{r},\boldsymbol{r}',\omega) = 4\pi\mathbf{I}\delta(\boldsymbol{r},\boldsymbol{r}') \tag{A.9}$$

according to

$$\hat{\boldsymbol{E}}(\boldsymbol{r},\omega) = \frac{\omega^2}{c^2}\int d^3\boldsymbol{r}'\boldsymbol{G}(\boldsymbol{r},\boldsymbol{r}',\omega)\cdot\hat{\boldsymbol{P}}_{\boldsymbol{N}}(\boldsymbol{r}',\omega)$$
$$= i\sqrt{\frac{\hbar}{\pi\epsilon_0}}\frac{\omega^2}{c^2}\int d^3\boldsymbol{r}'\sqrt{\epsilon''(\boldsymbol{r}',\omega)}\boldsymbol{G}(\boldsymbol{r},\boldsymbol{r}',\omega)\hat{\boldsymbol{f}}(\boldsymbol{r}',\omega). \tag{A.10}$$

To specify the quantum state, we assume that the reservoir variables are distributed in the uncorrelated thermal equilibrium mixture of states. For finite temperatures T, we may apply the canonical density operator

$$\hat{\rho} = \frac{\exp(-H/k_BT)}{\mathrm{Tr}[\exp(-H/k_BT)]}. \tag{A.11}$$

where k_B is the Boltzmann constant and H is the Hamiltonian of the system, $H = \Sigma_{\mu,\boldsymbol{R}}\hbar\omega_\mu\hat{\boldsymbol{f}}^\dagger_{\mu,\boldsymbol{R}}\hat{\boldsymbol{f}}_{\mu,\boldsymbol{R}}$ with $(\mu,\boldsymbol{R})$ being the grid points. A straightforward calculation shows that

$$\left\langle\hat{\boldsymbol{f}}^\dagger(\boldsymbol{r},\omega)\otimes\hat{\boldsymbol{f}}(\boldsymbol{r}',\omega')\right\rangle = \delta(\boldsymbol{r},\boldsymbol{r}')\delta(\omega-\omega')\frac{1}{2}\left[\coth\left(\frac{\hbar\omega}{2k_BT}\right)-1\right], \tag{A.12}$$

$$\left\langle\hat{\boldsymbol{f}}(\boldsymbol{r},\omega)\otimes\hat{\boldsymbol{f}}^\dagger(\boldsymbol{r}',\omega')\right\rangle = \delta(\boldsymbol{r},\boldsymbol{r}')\delta(\omega-\omega')\frac{1}{2}\left[\coth\left(\frac{\hbar\omega}{2k_BT}\right)+1\right], \tag{A.13}$$

$$\left\langle\hat{\boldsymbol{f}}(\boldsymbol{r},\omega)\otimes\hat{\boldsymbol{f}}(\boldsymbol{r}',\omega')\right\rangle = \left\langle\hat{\boldsymbol{f}}^\dagger(\boldsymbol{r},\omega)\otimes\hat{\boldsymbol{f}}^\dagger(\boldsymbol{r}',\omega')\right\rangle = 0. \tag{A.14}$$

Now, substituting equation (A.4) and the corresponding displacement field into equations (A.2) and (A.3), we may write, on recalling equations (A.12) − (A.14),

$$\boldsymbol{T}_1(\boldsymbol{r},\boldsymbol{r}',t) = \int_0^\infty d\omega\int_0^\infty d\omega'\left[e^{-i(\omega-\omega')t}\left\langle\hat{\boldsymbol{D}}(\boldsymbol{r},\omega)\otimes\hat{\boldsymbol{E}}^\dagger(\boldsymbol{r}',\omega')\right\rangle\right.$$
$$\left. + e^{i(\omega-\omega')t}\left\langle\hat{\boldsymbol{D}}^\dagger(\boldsymbol{r},\omega)\otimes\hat{\boldsymbol{E}}(\boldsymbol{r}',\omega')\right\rangle\right], \tag{A.15}$$

$$\boldsymbol{T}_2(\boldsymbol{r},\boldsymbol{r}',t) = \int_0^\infty d\omega \int_0^\infty d\omega' \left[e^{-i(\omega-\omega')t} \left\langle \hat{\boldsymbol{B}}(\boldsymbol{r},\omega) \otimes \hat{\boldsymbol{H}}^\dagger(\boldsymbol{r}',\omega') \right\rangle \right.$$
$$\left. + e^{i(\omega-\omega')t} \left\langle \hat{\boldsymbol{B}}^\dagger(\boldsymbol{r},\omega) \otimes \hat{\boldsymbol{H}}(\boldsymbol{r}',\omega') \right\rangle \right], \tag{A.16}$$

Using the explicit expressions of equations (A.8) and (A.10) and the reciprocity property $\boldsymbol{G}_{ij}(\boldsymbol{r},\boldsymbol{r}',\omega) = \boldsymbol{G}_{ji}(\boldsymbol{r}',\boldsymbol{r},\omega)$, we obtain

$$\boldsymbol{T}_1(\boldsymbol{r},\boldsymbol{r}',t) = \mu_0 \int_0^\infty d\omega \int_0^\infty d\omega' {\omega'}^2 \boldsymbol{\nabla} \times \boldsymbol{\nabla} \times \boldsymbol{K}(\boldsymbol{r},\boldsymbol{r}',\omega,\omega',t), \tag{A.17}$$

and

$$\boldsymbol{T}_2(\boldsymbol{r},\boldsymbol{r}',t) = -\mu_0 \int_0^\infty d\omega \int_0^\infty d\omega' \omega\omega' \boldsymbol{\nabla} \times \boldsymbol{K}(\boldsymbol{r},\boldsymbol{r}',\omega,\omega',t) \times \overleftarrow{\boldsymbol{\nabla}}', \tag{A.18}$$

where

$$\boldsymbol{K}(\boldsymbol{r},\boldsymbol{r}',\omega,\omega',t)$$
$$= \left[e^{-i(\omega-\omega')t} \left\langle \left(\int d^3\boldsymbol{r}' \boldsymbol{G}(\boldsymbol{r},\boldsymbol{r}',\omega) \sqrt{\frac{\hbar\epsilon_0}{\pi}\epsilon''(\boldsymbol{r}',\omega)}\hat{\boldsymbol{f}}(\boldsymbol{r}',\omega) \right) \right.\right.$$
$$\left. \otimes \left(\int d^3\boldsymbol{r}'' \sqrt{\frac{\hbar\epsilon_0}{\pi}\epsilon''(\boldsymbol{r}'',\omega')}\hat{\boldsymbol{f}}^\dagger(\boldsymbol{r}'',\omega') \boldsymbol{G}^*(\boldsymbol{r}',\boldsymbol{r}'',\omega') \right) \right\rangle$$
$$+ e^{i(\omega-\omega')t} \left\langle \left(\int d^3\boldsymbol{r}' \boldsymbol{G}^*(\boldsymbol{r},\boldsymbol{r}',\omega) \sqrt{\frac{\hbar\epsilon_0}{\pi}\epsilon''(\boldsymbol{r}',\omega)}\hat{\boldsymbol{f}}^\dagger(\boldsymbol{r}',\omega) \right) \right.$$
$$\left.\left. \otimes \left(\int d^3\boldsymbol{r}'' \sqrt{\frac{\hbar\epsilon_0}{\pi}\epsilon''(\boldsymbol{r}'',\omega')}\hat{\boldsymbol{f}}(\boldsymbol{r}'',\omega') \boldsymbol{G}(\boldsymbol{r}',\boldsymbol{r}'',\omega') \right) \right\rangle \right], \tag{A.19}$$

Using equations (A.12) − (A.14), from equations (A.17) and (A.19) we derive

$$\boldsymbol{T}_1(\boldsymbol{r},\boldsymbol{r}',t)=\frac{\hbar}{\pi}\int_0^\infty d\omega\coth\left(\frac{\hbar\omega}{2k_BT}\right)\boldsymbol{\nabla}\times\boldsymbol{\nabla}\times\mathrm{Im}[\boldsymbol{G}(\boldsymbol{r},\boldsymbol{r}',\omega)]. \tag{A.20}$$

Recalling equation (A.9), we see that equation (A.20) leads to

$$\boldsymbol{T}_1(\boldsymbol{r},\boldsymbol{r}',t)=\frac{\hbar}{\pi}\int_0^\infty d\omega\coth\left(\frac{\hbar\omega}{2k_BT}\right)\frac{\omega^2}{c^2}\mathrm{Im}[\epsilon(\boldsymbol{r},\omega)\boldsymbol{G}(\boldsymbol{r},\boldsymbol{r}',\omega)]. \tag{A.21}$$

Similarly, we obtain

$$\boldsymbol{T}_2(\boldsymbol{r},\boldsymbol{r}',t)=\frac{\hbar}{\pi}\int_0^\infty d\omega\coth\left(\frac{\hbar\omega}{2k_BT}\right)\boldsymbol{\nabla}\times\mathrm{Im}[\boldsymbol{G}(\boldsymbol{r},\boldsymbol{r}',\omega)]\times\overleftarrow{\boldsymbol{\nabla}}'. \tag{A.22}$$

Here,

$$\left[\boldsymbol{G}(\boldsymbol{r},\boldsymbol{s},\omega)\times\overleftarrow{\boldsymbol{\nabla}}_{\boldsymbol{s}}\right]_{ij}=\epsilon_{jkl}\partial_k^s G_{il}(\boldsymbol{r},\boldsymbol{s},\omega). \tag{A.23}$$

The explicit form of the multilayer Green tensor used in calculating the stress tensors of equations (A.21) and (A.22) and consequently equation (A.1) is constructed in terms of generalized Fresnel coefficients as given in Ref. [62]. Writing the wave vector of an rightward (leftward) propagation waves in a j th layer as $\mathbf{K}_j^{\pm}=\mathbf{k}_\parallel\pm\beta_j\hat{\mathbf{z}}$ with $\mathbf{k}_\parallel=(k_x,k_y)$ is the wave vector parallel to the system surfaces. Here, $\beta_j=\sqrt{k_j^2-k_\parallel}$ and $k_j(\omega)=\sqrt{\epsilon_j(\omega)}\omega/c$. Therefore, the scattering field in the j th layer reads [62]

$$\begin{aligned}\boldsymbol{G}_j^{\mathrm{sca}}(\boldsymbol{r},\boldsymbol{r}',\omega)=&\frac{i}{8\pi^2}\int\frac{d^2\mathbf{k}_\parallel}{\beta_j}e^{i\mathbf{k}_\parallel\cdot(\boldsymbol{r}_\parallel-\boldsymbol{r}'_\parallel)}\sum_{q=p,s}\frac{e^{i\beta_jd_j}}{D_{qj}}\xi_q\\&\times\Big\{r_{j-}^q e^{i\beta_jz_-}\hat{\boldsymbol{e}}_{qj}^+(\mathbf{k}_\parallel)\left[\hat{\boldsymbol{e}}_{qj}^+(-\mathbf{k}_\parallel)e^{-i\beta_jz'_+}+r_{j+}^q\hat{\boldsymbol{e}}_{qj}^-(-\mathbf{k}_\parallel)e^{i\beta_jz'_+}\right]\\&+r_{j+}^q e^{i\beta_jz_+}\hat{\boldsymbol{e}}_{qj}^-(\mathbf{k}_\parallel)\left[\hat{\boldsymbol{e}}_{qj}^-(-\mathbf{k}_\parallel)e^{-i\beta_jz'_-}+r_{j-}^q\hat{\boldsymbol{e}}_{qj}^+(-\mathbf{k}_\parallel)e^{i\beta_jz'_-}\right]\Big\},\end{aligned} \tag{A.24}$$

where $D_{qj} = 1 - r^q_{j+} r^q_{j-} e^{2i\beta_j d_j}$, $\xi_p = 1$, $\xi_s = -1$, $z_- \equiv z$, and $z_+ \equiv d_j - z$,

$$\hat{\boldsymbol{e}}^{\mp}_{pj}(\mathbf{k}_\parallel) = \frac{1}{k_j}(\pm\beta_j \hat{\mathbf{k}}_\parallel + k_\parallel \hat{\boldsymbol{z}}), \qquad \hat{\boldsymbol{e}}^{\mp}_{sj}(\mathbf{k}_\parallel) = \hat{\mathbf{k}}_\parallel \times \hat{\boldsymbol{z}}. \tag{A.25}$$

The Fresnel coefficients satisfy

$$r^q_{i/j/k} = r^q_{i/j} + \frac{t^q_{i/j} t^q_{j/i} r^q_{j/k} e^{2i\beta_j d_j}}{1 - r^q_{j/i} r^q_{j/k} e^{2i\beta_j d_j}},$$

$$t^q_{i/j/k} = \frac{t^q_{i/j} t^q_{j/k} e^{i\beta_j d_j}}{1 - r^q_{j/i} r^q_{j/k} e^{2i\beta_j d_j}}, \tag{A.26}$$

where, for a single i/j interface, reduce to

$$r^p_{i/j} = \frac{\epsilon_j \beta_i - \epsilon_i \beta_j}{\epsilon_j \beta_i + \epsilon_i \beta_j}, \qquad t^p_{i/j} = \sqrt{\frac{\epsilon_i}{\epsilon_j}}(1 + r^p_{i/j}). \tag{A.27}$$

$$r^s_{i/j} = \frac{\beta_i - \beta_j}{\beta_i + \beta_j}, \qquad t^s_{i/j} = (1 + r^s_{i/j}). \tag{A.28}$$

The corresponding dyadic Green tensor for the magnetic field in the layer j

$$\begin{aligned}
\boldsymbol{G}^{\mathrm{B}}_j &\equiv \boldsymbol{\nabla} \times \boldsymbol{G}(\boldsymbol{r}, \boldsymbol{r}', \omega) \times \overleftarrow{\boldsymbol{\nabla}}' \\
&= -\frac{i}{8\pi^2} \int \frac{d^2\mathbf{k}_\parallel}{\beta_j} e^{i\mathbf{k}_\parallel \cdot (\boldsymbol{r}_\parallel - \boldsymbol{r}'_\parallel)} \sum_{q=p,s} \frac{e^{i\beta_j d_j}}{D_{qj}} \xi_q \\
&\times \Bigg\{ r^q_{j-} e^{i\beta_j z_-} \left(\mathbf{K}^+_j \times \hat{\boldsymbol{e}}^+_{qj}(\mathbf{k}_\parallel)\right) \left[\left(\mathbf{K}^-_j \times \hat{\boldsymbol{e}}^+_{qj}(-\mathbf{k}_\parallel)\right) e^{-i\beta_j z'_+} + r^q_{j+} \left(\mathbf{K}^+_j \times \hat{\boldsymbol{e}}^-_{qj}(-\mathbf{k}_\parallel)\right) e^{i\beta_j z'_+} \right] \\
&+ r^q_{j+} e^{i\beta_j z_+} \left(\mathbf{K}^-_j \times \hat{\boldsymbol{e}}^-_{qj}(\mathbf{k}_\parallel)\right) \left[\left(\mathbf{K}^+_j \times \hat{\boldsymbol{e}}^-_{qj}(-\mathbf{k}_\parallel)\right) e^{-i\beta_j z'_-} + r^q_{j-} \left(\mathbf{K}^-_j \times \hat{\boldsymbol{e}}^+_{qj}(-\mathbf{k}_\parallel)\right) e^{i\beta_j z'_-} \right] \Bigg\},
\end{aligned} \tag{A.29}$$

Using

$$\mathbf{K}_j^{\pm} \times \hat{\boldsymbol{e}}_{qj}^{\pm}(\mathbf{k}_{\parallel}) = k_j \xi_q \hat{\boldsymbol{e}}_{q'j}^{-}(\mathbf{k}_{\parallel}), \qquad p' = s, \qquad s' = p, \tag{A.30}$$

into equation (A.12), we easily find the equal-point dyadics Green function

$$\begin{aligned}\boldsymbol{G}_j^{\mathrm{sca}}(\boldsymbol{r},\boldsymbol{r},\omega) =& \frac{i}{8\pi^2 k_j^2} \int \frac{d^2\mathbf{k}_{\parallel}}{\beta_j} \Bigg\{ \hat{\mathbf{k}}\hat{\mathbf{k}} \frac{\beta_j^2}{D_{pj}} \left[2 r_{j-}^p r_{j+}^p e^{2i\beta_j d_j} - r_{j-}^p e^{2i\beta_j z_-} - r_{j+}^p e^{2i\beta_j z_+} \right] \\ & \hat{\mathbf{n}}\hat{\mathbf{n}} \frac{k_j^2}{D_{sj}} \left[2 r_{j-}^s r_{j+}^s e^{2i\beta_j d_j} + r_{j-}^s e^{2i\beta_j z_-} + r_{j+}^s e^{2i\beta_j z_+} \right] \\ & + \hat{\mathbf{z}}\hat{\mathbf{z}} \frac{k_{\parallel}^2}{D_{pj}} \left[2 r_{j-}^p r_{j+}^p e^{2i\beta_j d_j} + r_{j-}^p e^{2i\beta_j z_-} + r_{j+}^p e^{2i\beta_j z_+} \right] \Bigg\}, \end{aligned} \tag{A.31}$$

$$\begin{aligned}\boldsymbol{G}_j^{\mathrm{B}}(\boldsymbol{r},\boldsymbol{r},\omega) =& \frac{i}{8\pi^2} \int \frac{d^2\mathbf{k}_{\parallel}}{\beta_j} \Bigg\{ \hat{\mathbf{k}}\hat{\mathbf{k}} \frac{\beta_j^2}{D_{sj}} \left[2 r_{j-}^s r_{j+}^s e^{2i\beta_j d_j} - r_{j-}^s e^{2i\beta_j z_-} - r_{j+}^s e^{2i\beta_j z_+} \right] \\ & \hat{\mathbf{n}}\hat{\mathbf{n}} \frac{k_j^2}{D_{pj}} \left[2 r_{j-}^p r_{j+}^p e^{2i\beta_j d_j} + r_{j-}^p e^{2i\beta_j z_-} + r_{j+}^p e^{2i\beta_j z_+} \right] \\ & + \hat{\mathbf{z}}\hat{\mathbf{z}} \frac{k_{\parallel}^2}{D_{sj}} \left[2 r_{j-}^s r_{j+}^s e^{2i\beta_j d_j} + r_{j-}^s e^{2i\beta_j z_-} + r_{j+}^s e^{2i\beta_j z_+} \right] \Bigg\}, \end{aligned} \tag{A.32}$$

Substituting equations (A.31) and (A.32) into equations (A.21) and (A.22), the traces $\boldsymbol{G}_j^{\mathrm{sca}}(\boldsymbol{r},\boldsymbol{r},\omega)$ and $\boldsymbol{G}_j^{\mathrm{B}}(\boldsymbol{r},\boldsymbol{r},\omega)$ can be readily recognized and one has,

$$\begin{aligned}\mathrm{Tr}[\boldsymbol{T}_1(\boldsymbol{r},\boldsymbol{r}) + \boldsymbol{T}_2(\boldsymbol{r},\boldsymbol{r})] =& \frac{1}{D_{pj}} \left\{ 4 r_{j-}^p r_{j+}^p e^{2i\beta_j d_j} \beta_j^2 + 2k_{\parallel}^2 \left(2 r_{j-}^p r_{j+}^p e^{2i\beta_j d_j} + r_{j-}^p e^{2i\beta_j z_-} + r_{j+}^p e^{2i\beta_j z_+} \right) \right\} \\ & \frac{1}{D_{sj}} \left\{ 4 r_{j-}^s r_{j+}^s e^{2i\beta_j d_j} \beta_j^2 + 2k_{\parallel}^2 \left(2 r_{j-}^s r_{j+}^s e^{2i\beta_j d_j} + r_{j-}^s e^{2i\beta_j z_-} + r_{j+}^s e^{2i\beta_j z_+} \right) \right\}, \end{aligned} \tag{A.33}$$

The Casimir force (per unit area) between the two stacks separated by the j th layer is then determined by the z components of the stress tensor giving in equation (A.1)

with

$$\bar{\mathbf{I}} = \sum_{q=p,s} \hat{\boldsymbol{e}}^{\pm}_{qj}(\mathbf{k}_{\parallel})\hat{\boldsymbol{e}}^{\pm}_{qj}(\mathbf{k}_{\parallel}) + \left(\hat{\boldsymbol{e}}^{\pm}_{pj} \times \hat{\boldsymbol{e}}^{\pm}_{sj}(\mathbf{k}_{\parallel})\right)\left(\hat{\boldsymbol{e}}^{\pm}_{pj} \times \hat{\boldsymbol{e}}^{\pm}_{sj}(\mathbf{k}_{\parallel})\right). \tag{A.34}$$

Then

$$T_{j,zz} = -\frac{\hbar}{\pi}\mathrm{Re}\int_0^{\infty} d\omega \coth\left(\frac{\hbar\omega}{2k_BT}\right)\int \frac{d^2\mathbf{k}_{\parallel}}{(2\pi)^2}\beta_j \sum_{q=p,s} \frac{1 - D_{qj}(\omega, k_{\parallel})}{D_{qj}(\omega, k_{\parallel})}, \tag{A.35}$$

where $\beta_j(\omega, k_{\parallel}) = \sqrt{k_j^2(\omega) - k_{\parallel}^2}$,

$$D_{qj}(\omega, k_{\parallel})1 - r^q_{j-}(\omega, k_{\parallel})r^q_{j+}(\omega, k_{\parallel})e^{2i\beta_j d_j}. \tag{A.36}$$

APPENDIX B

GREEN'S FUNCTION IN A SPHERICALLY MULTILAYERED MEDIUM

B.1 Electromagnetic dyadic Green's function

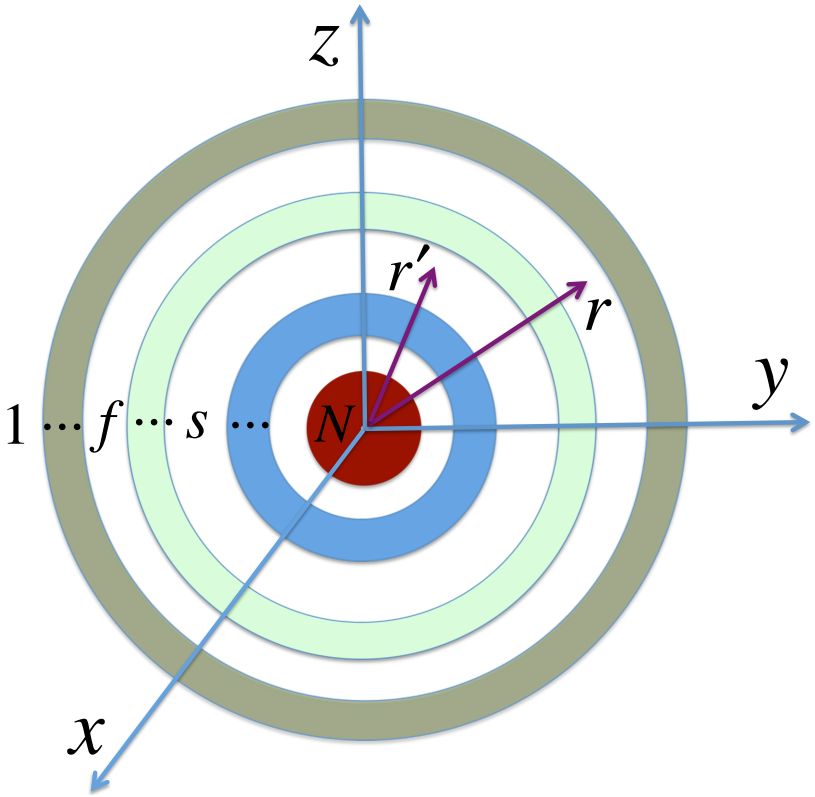

Figure B.1: Structure of a spherically N-layered medium. The layers containing the field $\boldsymbol{r}$ in the fth layer and the source $\boldsymbol{r'}$ in the sth layer.

Starting with the Maxwell's equations, the electromagnetic fields $\boldsymbol{E}_f$ and $\boldsymbol{H}_f$ in the fth layer ($f = 1, 2, ..., N$), contributed by the electric and magnetic current sources $\boldsymbol{J}_s$ and $\boldsymbol{M}_s$ located in the sth layer ($s = 1, 2, ..., N$), of a spherically N-

layered medium can be expressed as [151, 152]

$$\nabla \times \nabla \times \boldsymbol{E}_f - k_f^2 \boldsymbol{E}_f = i\omega\mu_f \boldsymbol{J}_f \delta_f^s - (\nabla \times \boldsymbol{M})_f \delta_f^s, \tag{B.1}$$

$$\nabla \times \nabla \times \boldsymbol{H}_f - k_f^2 \boldsymbol{H}_f = i\omega\epsilon_f \boldsymbol{M}_f \delta_f^s + (\nabla \times \boldsymbol{J})_f \delta_f^s, \tag{B.2}$$

where k_f in the fth layer of the multilayered medium is derived as $k_f = \frac{\omega}{c}\sqrt{\mu_f \epsilon_f (1 + \frac{i\sigma_f}{\omega\epsilon_f})}$ with σ_f is the conductivity of the medium.

Solving equations (B.1) and (B.2) yield, respectively

$$\nabla \times \nabla \times \overline{\boldsymbol{G}}_e^{(fs)}(\boldsymbol{r}, \boldsymbol{r'}) - k_f^2 \overline{\boldsymbol{G}}_e^{(fs)}(\boldsymbol{r}, \boldsymbol{r'}) = \bar{\boldsymbol{I}} \delta(\boldsymbol{r} - \boldsymbol{r'}) \delta_f^s, \tag{B.3}$$

$$\nabla \times \nabla \times \overline{\boldsymbol{G}}_{m2}^{(fs)}(\boldsymbol{r}, \boldsymbol{r'}) - k_f^2 \overline{\boldsymbol{G}}_{m2}^{(fs)}(\boldsymbol{r}, \boldsymbol{r'}) = \nabla \times \left[\bar{\boldsymbol{I}} \delta(\boldsymbol{r} - \boldsymbol{r'})\right] \delta_f^s, \tag{B.4}$$

where $\overline{\boldsymbol{G}}_{m2}(\boldsymbol{r}, \boldsymbol{r'})$ is the magnetic dyadic Green's function of the second kind satisfying the equation

$$\nabla \times \overline{\boldsymbol{G}}_{m2}(\boldsymbol{r}, \boldsymbol{r'}) = \bar{\boldsymbol{I}} \delta(\boldsymbol{r} - \boldsymbol{r'}) + k_f^2 \overline{\boldsymbol{G}}_e^{(fs)}(\boldsymbol{r}, \boldsymbol{r'}), \tag{B.5}$$

where $\bar{\boldsymbol{I}}$ is the unit dyadic and $\delta(\boldsymbol{r} - \boldsymbol{r'})$ is the Dirac delta function.

B.2 Vector eigenfunction expansion method

The expression for various $\overline{\boldsymbol{G}}$ can be obtained by the conventional method explained in the theory of differential equations. Following [153], we apply the method of Ohm-Rayleigh, an approach introduced by Sommerfeld [154], or the method of vector eigenfunction expansion. The key step of this method is to expand $\delta(\boldsymbol{r} - \boldsymbol{r'})$ in terms of the eigenfunction of a homogenous vector wave equation of the same type.

$$\nabla \times \nabla \times \overline{\boldsymbol{F}} - \kappa^2 \overline{\boldsymbol{F}} = 0, \tag{B.6}$$

where κ is so far arbitrary. The spherical vector eigenfunctions which are solutions

of the vector equation (B.6) can be constructed as follows:

$$\boldsymbol{M}_{\substack{e\\o}mn}(\boldsymbol{r},\kappa) = \nabla \times \left[\psi_{\substack{e\\o}mn}(\boldsymbol{r},\kappa)\boldsymbol{r}\right] \tag{B.7}$$

$$\boldsymbol{N}_{\substack{e\\o}mn}(\boldsymbol{r},\kappa) = \frac{1}{\kappa}\nabla \times \nabla \times \left[\psi_{\substack{e\\o}mn}(\boldsymbol{r},\kappa)\boldsymbol{r}\right] \tag{B.8}$$

$$\boldsymbol{L}_{\substack{e\\o}mn}(\boldsymbol{r},\kappa) = \nabla\psi_{\substack{e\\o}mn}(\boldsymbol{r},\kappa). \tag{B.9}$$

Substituting Eqs. (B.7)-(B.9) into Eq. (B.6), it can be seen that $\boldsymbol{M}_{\substack{e\\o}mn}(\boldsymbol{r},\kappa)$, $\boldsymbol{N}_{\substack{e\\o}mn}(\boldsymbol{r},\kappa)$, and $\boldsymbol{L}_{\substack{e\\o}mn}(\boldsymbol{r},\kappa)$ are the solutions for Eq. (B.6) if the scalar wave equation, ψ, is a solution of $\nabla^2\psi(\boldsymbol{r},\kappa) + \kappa^2\psi(\boldsymbol{r},\kappa) = 0$ in spherical coordinate systems which can be written in the form

$$\psi_{\substack{e\\o}mn}(\boldsymbol{r},\kappa) = j_n(\kappa r)P_n^m(\cos\theta)\begin{matrix}\cos\\ \sin\end{matrix} m\phi, \tag{B.10}$$

where e and o stand for even and odd solutions in ϕ and $j_n(x)$ is the spherical Bessel function of order n which satisfies the differential equation

$$\frac{d^2}{dx^2}\left[xj_n(x)\right] + \left[1 - \frac{n(n+1)}{x^2}\right]xj_n(x) = 0. \tag{B.11}$$

It is related to the half-order cylindrical Bessel function by

$$j_n(x) = \left(\frac{\pi}{2x}\right)^{\frac{1}{2}} J_{n+1/2}(x). \tag{B.12}$$

The function $P_n^m(\cos\theta)$ is the associated Legendre polynomials of order (n,m) which satisfies the differential equation

$$\frac{1}{\sin\theta}\frac{d}{d\theta}\left[\sin\theta\frac{dP_n^m(\cos\theta)}{d\theta}\right] + \left[n(n+1) - \frac{m^2}{\sin^2\theta}\right]P_n^m(\cos\theta) = 0. \tag{B.13}$$

Rewriting Eqs. (B.7)-(B.9) with Eq. (B.10) in the form of functional expansion leading to the expressions

$$\begin{aligned}\boldsymbol{M}_{\substack{e\\o}mn}(\boldsymbol{r},\kappa) = &\mp \frac{m}{\sin\theta} j_n(\kappa r) P_n^m(\cos\theta) \begin{matrix}\sin\\ \cos\end{matrix} m\phi \hat{\boldsymbol{\theta}} \\ &- j_n(\kappa r) \frac{\partial P_n^m(\cos\theta)}{\partial\theta} \begin{matrix}\cos\\ \sin\end{matrix} m\phi \hat{\boldsymbol{\phi}}, \end{aligned} \tag{B.14}$$

$$\begin{aligned}\boldsymbol{N}_{\substack{e\\o}mn}(\boldsymbol{r},\kappa) = &\frac{n(n+1)}{\kappa r} j_n(\kappa r) P_n^m(\cos\theta) \begin{matrix}\cos\\ \sin\end{matrix} m\phi \hat{\boldsymbol{r}} \\ &+ \frac{1}{\kappa r} \frac{\partial\left[r j_n(\kappa r)\right]}{\partial r} \frac{\partial P_n^m(\cos\theta)}{\partial\theta} \begin{matrix}\cos\\ \sin\end{matrix} m\phi \hat{\boldsymbol{\theta}} \\ &\mp \frac{1}{\kappa r} \frac{\partial\left[r j_n(\kappa r)\right]}{\partial r} \frac{m}{\sin\theta} P_n^m(\cos\theta) \begin{matrix}\sin\\ \cos\end{matrix} m\phi \hat{\boldsymbol{\phi}}, \end{aligned} \tag{B.15}$$

$$\begin{aligned}\boldsymbol{L}_{\substack{e\\o}mn}(\boldsymbol{r},\kappa) = &\frac{\partial j_n(\kappa r)}{\partial r} P_n^m(\cos\theta) \begin{matrix}\cos\\ \sin\end{matrix} m\phi \hat{\boldsymbol{r}} \\ &+ \frac{j_n(\kappa r)}{r} \frac{\partial P_n^m(\cos\theta)}{\partial\theta} \begin{matrix}\cos\\ \sin\end{matrix} m\phi \hat{\boldsymbol{\theta}} \\ &\mp \frac{j_n(\kappa r)}{r} \frac{m}{\sin\theta} P_n^m(\cos\theta) \begin{matrix}\sin\\ \cos\end{matrix} m\phi \hat{\boldsymbol{\phi}}. \end{aligned} \tag{B.16}$$

According to the Ohm-Rayleigh methodology, we first seek an eigenfunction expansion for the source function on the right-hand side of Eq. (B.4), $\nabla \times \left[\bar{\boldsymbol{I}}\delta(\boldsymbol{r}-\boldsymbol{r'})\right]$, using the solenoidal vector wave functions introduced in the previous equations. Thus we let

$$\nabla \times \left[\bar{\boldsymbol{I}}\delta(\boldsymbol{r}-\boldsymbol{r'})\right]$$
$$= \int_0^\infty d\kappa \sum_{m,n} \left[\boldsymbol{N}_{\substack{e\\o}mn}(\boldsymbol{r},\kappa)\mathcal{A}_{\substack{e\\o}mn}(\boldsymbol{r},\kappa) + \boldsymbol{M}_{\substack{e\\o}mn}(\boldsymbol{r},\kappa)\mathcal{B}_{\substack{e\\o}mn}(\boldsymbol{r},\kappa)\right], \tag{B.17}$$

where $\mathcal{A}_{\substack{e\\o}mn}(\boldsymbol{r},\kappa)$ and $\mathcal{B}_{\substack{e\\o}mn}(\boldsymbol{r},\kappa)$ are two unknown vector coefficients to be determined. By taking the anterior scalar product of Eq. (B.17) with $\boldsymbol{M}_{\substack{e\\o}m'n'}(\kappa')$ and $\boldsymbol{N}_{\substack{e\\o}m'n'}(\kappa')$ and integrating the resultant equations through the entire space, we obtain

$$\iiint_V \boldsymbol{N}_{\substack{e\\o}m'n'}(\kappa') \cdot \nabla \times \left[\bar{\boldsymbol{I}}\delta(\boldsymbol{r}-\boldsymbol{r'})\right] \mathrm{d}V = \iiint_V \mathrm{d}V \int_0^\infty d\kappa \sum_{m,n} \boldsymbol{N}_{\substack{e\\o}m'n'}(\kappa')$$
$$\cdot \left[\boldsymbol{N}_{\substack{e\\o}mn}(\boldsymbol{r},\kappa)\mathcal{A}_{\substack{e\\o}mn}(\boldsymbol{r},\kappa) + \boldsymbol{M}_{\substack{e\\o}mn}(\boldsymbol{r},\kappa)\mathcal{B}_{\substack{e\\o}mn}(\boldsymbol{r},\kappa)\right]. \tag{B.18}$$

$$\iiint_V \boldsymbol{M}_{\substack{e\\o}m'n'}(\kappa') \cdot \nabla \times \left[\bar{\boldsymbol{I}}\delta(\boldsymbol{r}-\boldsymbol{r'})\right] \mathrm{d}V = \iiint_V \mathrm{d}V \int_0^\infty d\kappa \sum_{m,n} \boldsymbol{M}_{\substack{e\\o}m'n'}(\kappa')$$
$$\cdot \left[\boldsymbol{N}_{\substack{e\\o}mn}(\boldsymbol{r},\kappa)\mathcal{A}_{\substack{e\\o}mn}(\boldsymbol{r},\kappa) + \boldsymbol{M}_{\substack{e\\o}mn}(\boldsymbol{r},\kappa)\mathcal{B}_{\substack{e\\o}mn}(\boldsymbol{r},\kappa)\right]. \tag{B.19}$$

First, using the vector identities $\nabla \times (\nabla \times \boldsymbol{A}) = \nabla(\nabla \cdot \boldsymbol{A}) - \nabla^2 \boldsymbol{A}$ and $\nabla \cdot (\boldsymbol{A} \times \boldsymbol{B}) = (\nabla \times \boldsymbol{A}) \cdot \boldsymbol{B} - \boldsymbol{A} \cdot (\nabla \times \boldsymbol{B})$, the integral at the left-hand side of Eq. (B.18) can be split into two terms

$$\iiint_V \boldsymbol{N}_{\substack{e\\o}m'n'}(\kappa') \cdot \nabla \times \left[\bar{\boldsymbol{I}}\delta(\boldsymbol{r}-\boldsymbol{r'})\right] \mathrm{d}V$$
$$= \iiint_V \left\{ \nabla \times \boldsymbol{N}_{\substack{e\\o}m'n'}(\kappa') \cdot \bar{\boldsymbol{I}}\delta(\boldsymbol{r}-\boldsymbol{r'}) - \nabla . \left[\boldsymbol{N}_{\substack{e\\o}m'n'}(\kappa') \times \bar{\boldsymbol{I}}\delta(\boldsymbol{r}-\boldsymbol{r'})\right] \right\} \mathrm{d}V$$
$$= \nabla' \times \boldsymbol{N}'_{\substack{e\\o}m'n'}(\kappa') - \oiint_S \hat{n} \cdot \left[\boldsymbol{N}_{\substack{e\\o}m'n'}(\kappa') \times \bar{\boldsymbol{I}}\delta(\boldsymbol{r}-\boldsymbol{r'})\right] \mathrm{d}S, \tag{B.20}$$

In deriving Eq. (B.20) we have used the dyadic Gauss theorem to convert one volume integral into a surface integral. This integral vanishes because $\boldsymbol{r'}$ is located inside V. The functions $\nabla' \times \boldsymbol{N}'_{\substack{e\\o}m'n'}(\kappa')$ are defined with respect to (r', θ', ϕ') of the current source $\boldsymbol{J}_f$. Second, the integrals on the right-hand side of Eq. (B.18) can be calculated as a result of the orthogonal properties of the spherical vector wave functions. Based on the complete expressions of these functions as given in Eqs. (B.14) and (B.15), we obtain the following orthogonal relations:

$$\iiint_V \boldsymbol{M}_{\substack{e\\o}mn}(\boldsymbol{r}, \kappa) \cdot \boldsymbol{N}_{\substack{e\\o}m'n'}(\kappa') \, \mathrm{d}V = 0. \tag{B.21}$$

$$\begin{aligned}
&\iiint_V \boldsymbol{N}_{\substack{e\\o}mn}(\boldsymbol{r}, \kappa) \cdot \boldsymbol{N}_{\substack{e\\o}m'n'}(\kappa') \, \mathrm{d}V \\
&= \int_0^{\infty} \int_0^{\pi} \int_0^{2\pi} \boldsymbol{N}_{\substack{e\\o}mn}(\boldsymbol{r}, \kappa) \cdot \boldsymbol{N}_{\substack{e\\o}m'n'}(\kappa') r^2 \sin\theta \, \mathrm{d}r \, \mathrm{d}\theta \, \mathrm{d}\phi \\
&= \begin{cases} 0, & m \neq m', n \neq n' \\ \frac{(1+\delta_{0m})\pi^2}{\kappa^2} \frac{n(n+1)}{(2n+1)} \frac{(n+m)!}{(n-m)!} \delta(\kappa - \kappa'), & m = m', n = n'. \end{cases}
\end{aligned} \tag{B.22}$$

In deriving Eq. (B.21) we have used the following useful formulas found in [152]:

$$\int_0^{\pi} [P_n^m(\cos\theta)]^2 \sin\theta \, \mathrm{d}\theta = \frac{2}{2n+1} \frac{(n+m)!}{(n-m)!},$$

$$\begin{aligned}
&\int_0^{\pi} \left[\left(\frac{\partial P_n^m(\cos\theta)}{\partial \theta} \right)^2 + \left(\frac{m P_n^m(\cos\theta)}{\sin\theta} \right)^2 \right] \sin\theta \, \mathrm{d}\theta \\
&= \frac{2n(n+1)}{2n+1} \frac{(n+m)!}{(n-m)!},
\end{aligned} \tag{B.23a}$$

$$\frac{\mathrm{d}}{\mathrm{d}x} \left[x j_n(x) \right] = \frac{x}{2n+1} \left[(n+1) j_{n-1}(x) - n j_{n+1}(x) \right], \tag{B.23b}$$

$$j_n(x) = \frac{x}{2n+1} \left[j_{n-1}(x) + j_{n+1}(x) \right]. \tag{B.23c}$$

Substituting Eqs. (B.20-B.22) into Eq. (B.18) we obtain

$$\mathcal{A}_{\substack{e\\o}mn}(\boldsymbol{r},\kappa) = \frac{C_{mn}}{2\pi^2}\kappa^2\nabla'\times\boldsymbol{N}'_{\substack{e\\o}mn}(\kappa) \equiv \frac{C_{mn}}{2\pi^2}\kappa^3\boldsymbol{M}'_{\substack{e\\o}mn}(\kappa), \tag{B.24}$$

$$\mathcal{B}_{\substack{e\\o}mn}(\boldsymbol{r},\kappa) = \frac{C_{mn}}{2\pi^2}\kappa^2\nabla'\times\boldsymbol{M}'_{\substack{e\\o}mn}(\kappa) \equiv \frac{C_{mn}}{2\pi^2}\kappa^3\boldsymbol{N}'_{\substack{e\\o}mn}(\kappa), \tag{B.25}$$

where

$$C_{mn} = (2-\delta_{0m})\frac{(2n+1)}{n(n+1)}\frac{(n-m)!}{(n+m)!}. \tag{B.26}$$

Substituting Eqs. (B.24) and (B.25) into Eq. (B.17) we obtain

$$\begin{aligned}&\nabla\times\left[\bar{\boldsymbol{I}}\delta(\boldsymbol{r}-\boldsymbol{r'})\right]\\ &= \frac{1}{2\pi^2}\int_0^\infty d\kappa\sum_{m,n}C_{mn}\kappa^3\left[\boldsymbol{N}_{\substack{e\\o}mn}(\boldsymbol{r},\kappa)\boldsymbol{M}'_{\substack{e\\o}mn}(\boldsymbol{r},\kappa)+\boldsymbol{M}_{\substack{e\\o}mn}(\boldsymbol{r},\kappa)\boldsymbol{N}'_{\substack{e\\o}mn}(\boldsymbol{r},\kappa)\right],\end{aligned} \tag{B.27}$$

Now $\overline{\boldsymbol{G}}_{m0}(\boldsymbol{r},\boldsymbol{r'})$ in Eq. (B.4) can be represented by a similar integral in terms of the spherical vector eigenfunctionsin

$$\begin{aligned}\overline{\boldsymbol{G}}_{m0}(\boldsymbol{r},\boldsymbol{r'}) =&\frac{1}{2\pi^2}\int_0^\infty d\kappa\sum_{m,n}C_{mn}\kappa^3\\ &\cdot\left[\mathcal{C}_{\substack{e\\o}mn}(\boldsymbol{r},\kappa)\boldsymbol{N}_{\substack{e\\o}mn}(\boldsymbol{r},\kappa)\boldsymbol{M}'_{\substack{e\\o}mn}(\boldsymbol{r},\kappa)+\mathcal{D}_{\substack{e\\o}mn}(\boldsymbol{r},\kappa)\boldsymbol{M}_{\substack{e\\o}mn}(\boldsymbol{r},\kappa)\boldsymbol{N}'_{\substack{e\\o}mn}(\boldsymbol{r},\kappa)\right],\end{aligned} \tag{B.28}$$

where the coefficients $\mathcal{C}_{\substack{e\\o}mn}(\boldsymbol{r},\kappa)$ and $\mathcal{D}_{\substack{e\\o}mn}(\boldsymbol{r},\kappa)$ can be determined by substituting Eqs. (B.27) and (B.28) into Eq. (B.4) that leads, upon using the identities

$$\nabla\times\nabla\times\boldsymbol{N}_{\substack{e\\o}mn}(\boldsymbol{r},\kappa) = \kappa^2\boldsymbol{N}_{\substack{e\\o}mn}(\boldsymbol{r},\kappa) \tag{B.29}$$

$$\nabla\times\nabla\times\boldsymbol{M}_{\substack{e\\o}mn}(\boldsymbol{r},\kappa) = \kappa^2\boldsymbol{M}_{\substack{e\\o}mn}(\boldsymbol{r},\kappa). \tag{B.30}$$

$$\mathcal{C}_{\substack{e\\o}mn}(\boldsymbol{r},\kappa)=\mathcal{D}_{\substack{e\\o}mn}(\boldsymbol{r},\kappa)=\frac{1}{\kappa^2-k_s^2}. \tag{B.31}$$

$$\begin{aligned}\overline{\boldsymbol{G}}_{m0}(\boldsymbol{r},\boldsymbol{r'}) =&\frac{1}{2\pi^2}\int_0^\infty d\kappa\sum_{m,n}\frac{C_{mn}\kappa^3}{\kappa^2-k_s^2}\\ &\cdot\left[\boldsymbol{N}_{\substack{e\\o}mn}(\boldsymbol{r},\kappa)\boldsymbol{M}'_{\substack{e\\o}mn}(\boldsymbol{r},\kappa)+\boldsymbol{M}_{\substack{e\\o}mn}(\boldsymbol{r},\kappa)\boldsymbol{N}'_{\substack{e\\o}mn}(\boldsymbol{r},\kappa)\right],\end{aligned} \tag{B.32}$$

Inspection of Eqs. (B14) and (B.15), reveals that $j_n(\boldsymbol{r},\kappa)$ is a function of κ. By writing the integrand in Eq. (B.32) in an operational form $\boldsymbol{N}_{\substack{e\\o}mn}(\boldsymbol{r},\kappa)\boldsymbol{M}'_{\substack{e\\o}mn}(\boldsymbol{r},\kappa)=\overline{\overline{\boldsymbol{T}}}_\kappa\left[j_n(\kappa r)j_n(\kappa r')\right]$, we will encounter integrals of the type

$$F(r,r')=\int_0^\infty d\kappa\frac{\kappa^3}{\kappa^2-k_s^2}j_n(\kappa r)j_n(\kappa r'). \tag{B.33}$$

Using the relation between a Bessel function and the two Hankel functions, we can write $J_\nu(\kappa r')=H_\nu^{(1)}(\kappa r')+H_\nu^{(2)}(\kappa r')$. Also, by changing the variable of integration from κ to $\kappa e^{-i\pi}$ and using the relations of the Bessel functions [152], we have $J_\nu(\kappa re^{-i\pi})=e^{-i\nu\pi}J_\nu(\kappa r)$ and $H_\nu^{(2)}(\kappa re^{-i\pi})=-e^{i\nu\pi}H_\nu^{(1)}(\kappa r)$ which is related to the spherical Bessel function by the relation $j_\nu(x)=\left(\frac{\pi}{2x}\right)^{\frac{1}{2}}J_{\nu+\frac{1}{2}}(x)$ and the spherical Hankel function of the first kind by the relation $h_\nu^{(1)}(x)=\left(\frac{\pi}{2x}\right)^{\frac{1}{2}}H^{(1)}_{\nu+\frac{1}{2}}(x)$. Applying the method of contour integration along a semi-infinite circular path in the upper complex $\kappa-$plane, we obtain

$$F(r,r')=\frac{i\pi k_s^2}{2}\begin{cases}h_n^{(1)}(k_sr)j_n(k_sr'), & r>r'\\ j_n(k_sr)h_n^{(1)}(k_sr'), & r<r'\end{cases} \tag{B.34}$$

and similarly for $\boldsymbol{M}_{\substack{e\\o}mn}(\boldsymbol{r},\kappa)\boldsymbol{N}'_{\substack{e\\o}mn}(\boldsymbol{r},\kappa)$. Using the resultant, we obtain the eigenfunction expansion for $\overline{\boldsymbol{G}}_{m0}$, namely,

$$
\begin{aligned}
&\overline{\boldsymbol{G}}^{\pm}_{m0}(\boldsymbol{r},\boldsymbol{r}') \\
=&\frac{ik_s^2}{4\pi}\sum_{m,n} C_{mn}
\begin{cases}
\boldsymbol{N}^{(1)}_{\substack{e\\o}mn}(\boldsymbol{r},k_s)\boldsymbol{M}_{\substack{e\\o}mn}(\boldsymbol{r}',k_s)+\boldsymbol{M}^{(1)}_{\substack{e\\o}mn}(\boldsymbol{r},k_s)\boldsymbol{N}_{\substack{e\\o}mn}(\boldsymbol{r}',k_s), & r>r' \\
\boldsymbol{N}_{\substack{e\\o}mn}(\boldsymbol{r},k_s)\boldsymbol{M}^{(1)}_{\substack{e\\o}mn}(\boldsymbol{r}',k_s)+\boldsymbol{M}_{\substack{e\\o}mn}(\boldsymbol{r},k_s)\boldsymbol{N}^{(1)}_{\substack{e\\o}mn}(\boldsymbol{r}',k_s), & r<r',
\end{cases}
\end{aligned}
\tag{B.35}
$$

where the prime denotes the coordinates with respect to (r',θ',ϕ') of the current source $\boldsymbol{J}_f$. The superscript (1) in Eq. (B.35) indicates that, in this equation, the spherical Bessel function $j_n(x)$ in Eqs. (B.14) and (B.15) has to be replaced with the spherical Hankel function of the first kind $h_n^{(1)}$. Using the discontinuity satisfies the boundary conditions $\hat{\boldsymbol{n}}\times(\overline{\boldsymbol{G}}^{+}_{m0}-\overline{\boldsymbol{G}}^{-}_{m0})=\bar{\boldsymbol{I}}_s\delta(\boldsymbol{r}-\boldsymbol{r}')$, we have

$$
\hat{\boldsymbol{r}}\times(\overline{\boldsymbol{G}}^{+}_{m0}-\overline{\boldsymbol{G}}^{-}_{m0})=(\bar{\boldsymbol{I}}-\hat{\boldsymbol{r}}\hat{\boldsymbol{r}})\frac{\delta(\theta-\theta')\delta(\phi-\phi')}{r'^2\sin\theta'}. \tag{B.36}
$$

From the discontinuity of the magnetic dyadic Green function, we can write

$$
\overline{\boldsymbol{G}}_{m0}(\boldsymbol{r},\boldsymbol{r}')=\overline{\boldsymbol{G}}^{+}_{m0}(\boldsymbol{r},\boldsymbol{r}')U(r-r')+\overline{\boldsymbol{G}}^{-}_{m0}(\boldsymbol{r},\boldsymbol{r}')U(r'-r), \tag{B.37}
$$

where U is the unit step function. Here,

$$
\begin{aligned}
\nabla\times\overline{\boldsymbol{G}}_{m0}(\boldsymbol{r},\boldsymbol{r}')=&\left[\nabla\times\overline{\boldsymbol{G}}^{+}_{m0}(\boldsymbol{r},\boldsymbol{r}')\right]U(r-r')+\nabla U(r-r')\times\overline{\boldsymbol{G}}^{+}_{m0}(\boldsymbol{r},\boldsymbol{r}') \\
&+\left[\nabla\times\overline{\boldsymbol{G}}^{-}_{m0}(\boldsymbol{r},\boldsymbol{r}')\right]U(r'-r)+\nabla U(r'-r)\times\overline{\boldsymbol{G}}^{-}_{m0}(\boldsymbol{r},\boldsymbol{r}'),
\end{aligned}
\tag{B.38}
$$

where we have used the identity $\nabla\times(a\bar{\boldsymbol{b}})=a(\nabla\times\bar{\boldsymbol{b}})+(\nabla a)\times\bar{\boldsymbol{b}}$. From the theory of generalized functions,

$$
\nabla U(r-r')=\hat{\boldsymbol{r}}\delta(r-r'), \tag{B.39}
$$

we obtain

$$\nabla \times \overline{\boldsymbol{G}}_{m0}(\boldsymbol{r},\boldsymbol{r}') =(\bar{\boldsymbol{I}} - \hat{\boldsymbol{r}}\hat{\boldsymbol{r}})\delta(\boldsymbol{r}-\boldsymbol{r}') + \left[\nabla \times \overline{\boldsymbol{G}}^{+}_{m0}(\boldsymbol{r},\boldsymbol{r}')\right] U(r-r') + \left[\nabla \times \overline{\boldsymbol{G}}^{-}_{m0}(\boldsymbol{r},\boldsymbol{r}')\right] U(r'-r). \tag{B.40}$$

Substituting Eq. (B.40) into Eq. (B.3) we obtain

$$\overline{\boldsymbol{G}}_{e0}(\boldsymbol{r},\boldsymbol{r}') =\frac{1}{k_s^2}\Bigg\{ - \hat{\boldsymbol{r}}\hat{\boldsymbol{r}}\delta(\boldsymbol{r}-\boldsymbol{r}') + \left[\nabla \times \overline{\boldsymbol{G}}^{+}_{m0}(\boldsymbol{r},\boldsymbol{r}')\right] U(r-r') + \left[\nabla \times \overline{\boldsymbol{G}}^{-}_{m0}(\boldsymbol{r},\boldsymbol{r}')\right] U(r'-r)\Bigg\}. \tag{B.41}$$

Substituting Eq. (B.35) into Eq. (B.41) leads to, upon using the identities $\nabla \times \boldsymbol{N}_{\substack{e\\o}mn}(\boldsymbol{r},k_s) = k_s \boldsymbol{M}_{\substack{e\\o}mn}(\boldsymbol{r},k_s)$ and $\nabla \times \boldsymbol{M}_{\substack{e\\o}mn}(\boldsymbol{r},k_s) = k_s \boldsymbol{N}_{\substack{e\\o}mn}(\boldsymbol{r},k_s)$

$$\begin{aligned}\overline{\boldsymbol{G}}_{e0}(\boldsymbol{r},\boldsymbol{r}') =& -\frac{1}{k_s^2}\hat{\boldsymbol{r}}\hat{\boldsymbol{r}}\delta(\boldsymbol{r}-\boldsymbol{r}') \\ &+ \frac{ik_s}{4\pi}\sum_{e,o}\sum_{n=1}^{\infty}\sum_{m=0}^{n}(2-\delta_{0m})\frac{2n+1}{n(n+1)}\frac{(n-m)!}{(n+m)!} \\ &\times \begin{cases} \boldsymbol{M}^{(1)}_{\substack{e\\o}mn}(\boldsymbol{r},k_s)\boldsymbol{M}_{\substack{e\\o}mn}(\boldsymbol{r}',k_s) + \boldsymbol{N}^{(1)}_{\substack{e\\o}mn}(\boldsymbol{r},k_s)\boldsymbol{N}_{\substack{e\\o}mn}(\boldsymbol{r}',k_s), & r > r', \\ \boldsymbol{M}_{\substack{e\\o}mn}(\boldsymbol{r},k_s)\boldsymbol{M}^{(1)}_{\substack{e\\o}mn}(\boldsymbol{r}',k_s) + \boldsymbol{N}_{\substack{e\\o}mn}(\boldsymbol{r},k_s)\boldsymbol{N}^{(1)}_{\substack{e\\o}mn}(\boldsymbol{r}',k_s), & r < r', \end{cases}\end{aligned} \tag{B.42}$$

B.3 A spherically multilayered medium

The dyadic Green's function can be constructed for a spherically N-layered medium where the field $\boldsymbol{r}$ is located in the fth layer and the source $\boldsymbol{r}'$ in the sth layer by means of method of scattering superposition

$$\overline{\boldsymbol{G}}_e^{(fs)}(\boldsymbol{r},\boldsymbol{r}') = \overline{\boldsymbol{G}}_{e0}(\boldsymbol{r},\boldsymbol{r}')\delta_f^s + \overline{\boldsymbol{G}}_{es}^{(fs)}(\boldsymbol{r},\boldsymbol{r}'). \tag{B.43}$$

Assuming that the current source is located in the layer s, the scattering dyadic Green's function for the layer $f(=1,2,....N)$ can be represented by

$$\begin{aligned}
\overline{\boldsymbol{G}}_{es}^{(fs)}(\boldsymbol{r},\boldsymbol{r}') =& \frac{ik_s}{4\pi}\sum_{e,o}\sum_{n=1}^{\infty}\sum_{m=0}^{n}(2-\delta_{0m})\frac{2n+1}{n(n+1)}\frac{(n-m)!}{(n+m)!} \\
&\times\Bigg\{(1-\delta_f^N)\boldsymbol{M}_{\substack{e\\o}mn}^{(1)}(\boldsymbol{r},k_f)\Big[(1-\delta_s^1)\mathcal{A}_M^{fs}\boldsymbol{M}_{\substack{e\\o}mn}(\boldsymbol{r}',k_s) \\
&+(1-\delta_s^N)\mathcal{B}_M^{fs}\boldsymbol{M}_{\substack{e\\o}mn}^{(1)}(\boldsymbol{r}',k_s)\Big] \\
&+(1-\delta_f^N)\boldsymbol{N}_{\substack{e\\o}mn}^{(1)}(\boldsymbol{r},k_f)\Big[(1-\delta_s^1)\mathcal{A}_N^{fs}\boldsymbol{N}_{\substack{e\\o}mn}(\boldsymbol{r}',k_s) \\
&+(1-\delta_s^N)\mathcal{B}_N^{fs}\boldsymbol{N}_{\substack{e\\o}mn}^{(1)}(\boldsymbol{r}',k_s)\Big] \\
&+(1-\delta_f^1)\boldsymbol{M}_{\substack{e\\o}mn}(\boldsymbol{r},k_f)\Big[(1-\delta_s^1)\mathcal{C}_M^{fs}\boldsymbol{M}_{\substack{e\\o}mn}(\boldsymbol{r}',k_s) \\
&+(1-\delta_s^N)\mathcal{D}_M^{fs}\boldsymbol{M}_{\substack{e\\o}mn}^{(1)}(\boldsymbol{r}',k_s)\Big] \\
&+(1-\delta_f^1)\boldsymbol{N}_{\substack{e\\o}mn}(\boldsymbol{r},k_f)\Big[(1-\delta_s^1)\mathcal{C}_N^{fs}\boldsymbol{N}_{\substack{e\\o}mn}(\boldsymbol{r}',k_s) \\
&+(1-\delta_s^N)\mathcal{D}_N^{fs}\boldsymbol{N}_{\substack{e\\o}mn}^{(1)}(\boldsymbol{r}',k_s)\Big]\Bigg\},
\end{aligned} \tag{B.44}$$

where $\mathcal{A}_{M,N}^{fs}$, $\mathcal{B}_{M,N}^{fs}$, $\mathcal{C}_{M,N}^{fs}$, and $\mathcal{D}_{M,N}^{fs}$ $(s=1,2,....N)$ are the coefficients of scattered dyadic Green's function to be solved by imposing the boundary conditions at the spherical interfaces $r=a_i(i=1,2,.....N-1)$:

$$\hat{\boldsymbol{r}}\times\overline{\boldsymbol{G}}_e^{(fs)}(\boldsymbol{r},\boldsymbol{r}') = \hat{\boldsymbol{r}}\times\overline{\boldsymbol{G}}_e^{[(f+1)s]}(\boldsymbol{r},\boldsymbol{r}'), \tag{B.45}$$

$$\frac{1}{\mu_f}\hat{\boldsymbol{r}}\times\nabla\times\overline{\boldsymbol{G}}_e^{(fs)}(\boldsymbol{r},\boldsymbol{r}') = \frac{1}{\mu_{f+1}}\hat{\boldsymbol{r}}\times\nabla\times\overline{\boldsymbol{G}}_e^{[(f+1)s]}(\boldsymbol{r},\boldsymbol{r}'). \tag{B.46}$$

The boundary conditions leads to the following coefficients matrix equations:

$$\begin{bmatrix} \mathcal{A}_M^{(f+1)s} + \delta_{f+1}^s \\ \mathcal{B}_M^{(f+1)s} \end{bmatrix} = \frac{1}{T_{Ff}^H} \begin{bmatrix} \mathcal{A}_M^{fs} \\ \mathcal{B}_M^{fs} \end{bmatrix} + \frac{\mathcal{R}_{Ff}^H}{T_{Ff}^H} \begin{bmatrix} \mathcal{C}_M^{fs} \\ \mathcal{D}_M^{fs} + \delta_f^s \end{bmatrix}, \tag{B.47a}$$

$$\begin{bmatrix} \mathcal{A}_N^{(f+1)s} + \delta_{f+1}^s \\ \mathcal{B}_N^{(f+1)s} \end{bmatrix} = \frac{1}{T_{Ff}^V} \begin{bmatrix} \mathcal{A}_N^{fs} \\ \mathcal{B}_N^{fs} \end{bmatrix} + \frac{\mathcal{R}_{Ff}^V}{T_{Ff}^V} \begin{bmatrix} \mathcal{C}_N^{fs} \\ \mathcal{D}_N^{fs} + \delta_f^s \end{bmatrix}, \tag{B.47b}$$

and

$$\begin{bmatrix} \mathcal{C}_M^{(f+1)s} \\ \mathcal{D}_M^{(f+1)s} \end{bmatrix} = \frac{\mathcal{R}_{Pf}^H}{T_{Pf}^H} \begin{bmatrix} \mathcal{A}_M^{fs} \\ \mathcal{B}_M^{fs} \end{bmatrix} + \frac{1}{T_{Pf}^H} \begin{bmatrix} \mathcal{C}_M^{fs} \\ \mathcal{D}_M^{fs} + \delta_f^s \end{bmatrix}, \tag{B.48a}$$

$$\begin{bmatrix} \mathcal{C}_N^{(f+1)s} \\ \mathcal{D}_N^{(f+1)s} \end{bmatrix} = \frac{\mathcal{R}_{Pf}^V}{T_{Pf}^V} \begin{bmatrix} \mathcal{A}_N^{fs} \\ \mathcal{B}_N^{fs} \end{bmatrix} + \frac{1}{T_{Pf}^V} \begin{bmatrix} \mathcal{C}_N^{fs} \\ \mathcal{D}_N^{fs} + \delta_f^s \end{bmatrix}, \tag{B.48b}$$

The matrix equations (B.47) and (B.48) can be rewritten in a form of recurrence equation:

$$\begin{bmatrix} \mathcal{A}_{M,N}^{(f+1)s} + \delta_{f+1}^s & \mathcal{B}_{M,N}^{(f+1)s} \\ \mathcal{C}_{M,N}^{(f+1)s} & \mathcal{D}_{M,N}^{(f+1)s} \end{bmatrix} = \begin{bmatrix} \frac{1}{T_{Ff}^{H,V}} & \frac{\mathcal{R}_{Ff}^{H,V}}{T_{Ff}^{H,V}} \\ \frac{\mathcal{R}_{Pf}^{H,V}}{T_{Pf}^{H,V}} & \frac{1}{T_{Pf}^{H,V}} \end{bmatrix} + \begin{bmatrix} \mathcal{A}_{M,N}^{fs} & \mathcal{B}_{M,N}^{fs} \\ \mathcal{C}_{M,N}^{fs} & \mathcal{D}_{M,N}^{fs} + \delta_f^s \end{bmatrix}, \tag{B.49}$$

where

$$\mathcal{R}_{Ff}^H = \frac{\mu_f k_{f+1} \psi_n'(k_{f+1} a_f) \psi_n(k_f a_f) - \mu_{f+1} k_f \psi_n'(k_f a_f) \psi_n(k_{f+1} a_f)}{\mu_f k_{f+1} \psi_n'(k_{f+1} a_f) \xi_n(k_f a_f) - \mu_{f+1} k_f \psi_n(k_{f+1} a_f) \xi_n'(k_f a_f)}, \tag{B.50a}$$

$$\mathcal{R}^V_{Ff} = \frac{\mu_f k_{f+1}\psi_n(k_{f+1}a_f)\psi_n'(k_f a_f) - \mu_{f+1}k_f\psi_n(k_f a_f)\psi_n'(k_{f+1}a_f)}{\mu_f k_{f+1}\psi_n(k_{f+1}a_f)\xi_n'(k_f a_f) - \mu_{f+1}k_f\psi_n'(k_{f+1}a_f)\xi_n(k_f a_f)}, \tag{B.50b}$$

$$T^H_{Ff} = \frac{\mu_f k_f\left[\psi_n'(k_{f+1}a_f)\xi_n(k_{f+1}a_f) - \psi_n(k_{f+1}a_f)\xi_n'(k_{f+1}a_f)\right]}{\mu_f k_{f+1}\psi_n'(k_{f+1}a_f)\xi_n(k_f a_f) - \mu_{f+1}k_f\psi_n(k_{f+1}a_f)\xi_n'(k_f a_f)}, \tag{B.50c}$$

$$T^V_{Ff} = \frac{\mu_f k_f\left[\psi_n(k_{f+1}a_f)\xi_n'(k_{f+1}a_f) - \psi_n'(k_{f+1}a_f)\xi_n(k_{f+1}a_f)\right]}{\mu_f k_{f+1}\psi_n(k_{f+1}a_f)\xi_n'(k_f a_f) - \mu_{f+1}k_f\psi_n'(k_{f+1}a_f)\xi_n(k_f a_f)}, \tag{B.50d}$$

$$\mathcal{R}^H_{Pf} = \frac{\mu_f k_{f+1}\xi_n'(k_{f+1}a_f)\xi_n(k_f a_f) - \mu_{f+1}k_f\xi_n'(k_f a_f)\xi_n(k_{f+1}a_f)}{\mu_f k_{f+1}\psi_n(k_f a_f)\xi_n'(k_{f+1}a_f) - \mu_{f+1}k_f\psi_n'(k_f a_f)\xi_n(k_{f+1}a_f)}, \tag{B.50e}$$

$$\mathcal{R}^V_{Pf} = \frac{\mu_f k_{f+1}\xi_n(k_{f+1}a_f)\xi_n'(k_f a_f) - \mu_{f+1}k_f\xi_n(k_f a_f)\xi_n'(k_{f+1}a_f)}{\mu_f k_{f+1}\psi_n'(k_f a_f)\xi_n(k_{f+1}a_f) - \mu_{f+1}k_f\psi_n(k_f a_f)\xi_n'(k_{f+1}a_f)}, \tag{B.50f}$$

$$T^H_{Pf} = \frac{\mu_f k_f\left[\psi_n(k_{f+1}a_f)\xi_n'(k_{f+1}a_f) - \psi_n'(k_{f+1}a_f)\xi_n(k_{f+1}a_f)\right]}{\mu_f k_{f+1}\psi_n(k_f a_f)\xi_n'(k_{f+1}a_f) - \mu_{f+1}k_f\psi_n'(k_f a_f)\xi_n(k_{f+1}a_f)}, \tag{B.50g}$$

$$T^V_{Pf} = \frac{\mu_f k_f\left[\psi_n'(k_{f+1}a_f)\xi_n(k_{f+1}a_f) - \psi_n(k_{f+1}a_f)\xi_n'(k_{f+1}a_f)\right]}{\mu_f k_{f+1}\psi_n'(k_f a_f)\xi_n(k_{f+1}a_f) - \mu_{f+1}k_f\psi_n(k_f a_f)\xi_n'(k_{f+1}a_f)}, \tag{B.50h}$$

with $\psi_n(\rho) = \rho j_n(\rho)$ and $\xi_n(\rho) = \rho h_n^{(1)}(\rho)$. The prime denotes differentiation with respect to the argument and the subscripts F and P indicate the centrifugal and centripetal modes, respectively. Here, $T^H_{(P,F)f}$ and $\mathcal{R}^H_{(P,F)f}$ represent the centripetal and centrifugal transmission and reflection contributed from TE modes while $T^V_{(P,F)f}$ and $\mathcal{R}^V_{(P,F)f}$ represent the centripetal and centrifugal transmission and reflection contributed from TM modes.

APPENDIX C

LOCAL DENSITY OF STATES: DERIVATION OF THE FREE-SPACE GREEN FUNCTION

The Green function in the case of the emitting dipole located outside sphere of spherically two-layered media along the z axis, at $z = r'$ can be written as

$$\begin{aligned}\boldsymbol{G}^R(\boldsymbol{r},\boldsymbol{r},\omega) =& \frac{ik_1}{4\pi}\sum_{n=1}^{\infty}(2n+1)\left[\frac{1}{2}\left(R^H\left[h_n^{(1)}(k_1r)\right]^2\right.\right.\\ &+R^V\frac{1}{(k_1r)^2}\left\{[k_1rh_n^{(1)}(k_1r)]'\right\}^2\left.\right)(\hat{\boldsymbol{x}}\hat{\boldsymbol{x}}+\hat{\boldsymbol{y}}\hat{\boldsymbol{y}})\\ &\left.+n(n+1)R^V\left(\frac{h_n^{(1)}(k_1r)}{k_1r}\right)^2\hat{\boldsymbol{z}}\hat{\boldsymbol{z}}\right]. \end{aligned} \tag{C.1}$$

Therefore, the imaginary part of the Green function along the z axis is

$$\begin{aligned}\mathrm{Im}[\boldsymbol{G}_{zz}(\boldsymbol{r},\boldsymbol{r},\omega)] =& \frac{k_1}{4\pi}\mathrm{Re}\sum_{n=1}^{\infty}(2n+1)n(n+1)\\ &\times R^V\left(\frac{h_n^{(1)}(k_1r)}{k_1r}\right)^2. \end{aligned} \tag{C.2}$$

The coefficients R^H and R^V are depend on the properties of the metal nanoparticle. Here, the reflections or scattering coefficients is given explicitly in Appendix B as.

$$R^V = \frac{k_1^2 j_n(k_1R)[k_2Rj_n(k_2R)]' - k_2^2 j_n(k_2R)[k_1Rj_n(k_1R)]'}{k_2^2 j_n(k_2R)[k_1Rh_n^{(1)}(k_1R)]' - k_1^2 h_n^{(1)}(k_1R)[k_2Rj_n(k_2R)]'}, \tag{C.3}$$

Now we apply the formula $(C2)$ to derive the imaginary part of the free-space

Green function. From Eq. (B.41), for $r > r'$, we have

$$\begin{aligned}\mathrm{Im}\boldsymbol{G}^0 =&\frac{k_1}{4\pi}\sum_{e,o}\sum_{n=1}^{\infty}\sum_{m=0}^{n}(2-\delta_{0m})\frac{2n+1}{n(n+1)}\frac{(n-m)!}{(n+m)!}\\ &\times \mathrm{Re}\left[\boldsymbol{N}^{(1)}_{mn^e_o}(\boldsymbol{r},k_1)\boldsymbol{N}_{mn^e_o}(\boldsymbol{r}',k_1)\right].\end{aligned} \tag{C.4}$$

Using Eq. (B.15) into Eq. (C.4), we get

$$\begin{aligned}\mathrm{Im}\boldsymbol{G}^0 =&\frac{k_1}{4\pi}\sum_{n=1}^{\infty}\sum_{m=0}^{n}(2-\delta_{0m})(2n+1)n(n+1)\frac{(n-m)!}{(n+m)!}\\ &\times \mathrm{Re}\left[\frac{j_n(k_1r')h_n^{(1)}(k_1r')}{(k_1r')^2}(P_n^m(1))^2\right]\\ =&\frac{k_1}{4\pi}\sum_{n=1}^{\infty}(2n+1)n(n+1)\mathrm{Re}\left[\frac{j_n(k_1r')h_n^{(1)}(k_1r')}{(k_1r')^2}\right]\\ =&\frac{k_1}{4\pi}\sum_{n=1}^{\infty}(2n+1)n(n+1)\left(\frac{j_n(k_1r')}{k_1r'}\right)^2.\end{aligned} \tag{C.5}$$

Denoting $z = k_1r'$,

$$\mathrm{Im}\boldsymbol{G}^0 = \frac{k_1}{4\pi}\sum_{n=1}^{\infty}(2n+1)n(n+1)\left(\frac{j_n(z)}{z}\right)^2. \tag{C.6}$$

We use the following formula [153]

$$\begin{aligned}\left(\frac{z}{2}\right)^{\mu+\nu} =&\frac{\Gamma(\mu+1)\Gamma(\nu+1)}{\Gamma(\mu+\nu+1)}\\ &\times\sum_{n=0}^{\infty}\frac{(\mu+\nu+2n)\Gamma(\mu+\nu+n)}{n!}J_{\mu+n}(z)J_{\nu+n}(z).\end{aligned} \tag{C.7}$$

For $\mu = \nu = 3/2$ and using the relation $J_{n+\frac{1}{2}}(z) = \sqrt{2z/\pi}j_n(z)$, we obtain

$$\left(\frac{z}{2}\right)^3 = \frac{\Gamma(5/2)\Gamma(5/2)}{\Gamma(4)} \sum_{n=0}^{\infty} \frac{(3+2n)\Gamma(3+n)}{n!} \left(J_{\frac{3}{2}+n}(z)\right)^2$$
$$= \frac{3\pi}{32} \sum_{n=1}^{\infty} \frac{(2n+1)\Gamma(n+2)}{(n-1)!} \left(J_{\frac{1}{2}+n}(z)\right)^2. \tag{C.8}$$

From Eq. (C.8) we have

$$\frac{2}{3} = \sum_{n=1}^{\infty} (2n+1)n(n+1) \left(\frac{j_n(z)}{z}\right)^2. \tag{C.9}$$

Substituting Eq. (C.9) into Eq. (C.5), we have

$$\mathrm{Im}\boldsymbol{G}^0 = \frac{k_1}{6\pi}. \tag{C.10}$$

APPENDIX D

EIGENFREQUENCY RELATION IN SPHERICALLY THREE-LAYERED MEDIA

The plasmon resonance can be obtained including retardation effect from the explicit form of the reflection coefficients derived in Appendix B by noticing that these coefficients contain poles at the points where the denominator vanishes. These poles give the eigenfrequency relation of the the electric modes supported by the metallic shell schematically presented in Fig. (4.1):

$$h_n^{(1)}(\rho_1)\alpha_n = [\rho_1 h_n^{(1)}(\rho_1]'\beta_n, \tag{D.1}$$

where

$$\alpha_n = k_2^2[\rho_2 j_n(\rho_2)]'A_n - k_3^2 j_n(\rho_2)B_n, \tag{D.2}$$

$$\beta_n = \frac{k_2^2}{k_1^2}\left\{k_2^2[\rho_2 j_n(\rho_2)]'C_n - k_3^2 j_n(\rho_2)D_n\right\}, \tag{D.3}$$

with

$$A_n = j_n(\eta_2)[\eta_1 h_n^{(1)}(\eta_1)]' - h_n^{(1)}(\eta_2)[\eta_1 j_n(\eta_1)]', \tag{D.4}$$

$$B_n = [\eta_1 h_n^{(1)}(\eta_1)]'[\eta_2 j_n(\eta_2)]' - [\eta_2 h_n^{(1)}(\eta_2)]'[\eta_1 j_n(\eta_1)]', \tag{D.5}$$

$$C_n = j_n(\eta_2)h_n^{(1)}(\eta_1) - j_n(\eta_1)h_n^{(1)}(\eta_2), \tag{D.6}$$

$$D_n = h_n^{(1)}(\eta_1)[\eta_2 j_n(\eta_2)]' - j_n(\eta_1)[\eta_2 h_n^{(1)}(\eta_2)]', \tag{D.7}$$

where $\rho_1 = k_1 R_1$, $\rho_2 = k_3 R_2$, $\eta_1 = k_2 R_1$, $\eta_2 = k_2 R_2$, and the prime denotes differentiation with respect to the argument. Here, $k_1 = \frac{\omega}{c}\sqrt{\epsilon_b}$, $k_2 = \frac{\omega}{c}\sqrt{\epsilon_m(\omega)}$, and $k_3 = \frac{\omega}{c}\sqrt{\epsilon_c}$.